Stony Brook University

Joint Application of Concentration and Isotope Ratios to Investigate the Global Atmospheric Carbon Monoxide Budget: An Inverse Modeling Approach

A Dissertation Presented

by

Key Hong Park

to

The Graduate School

in Partial Fulfillment of the

Requirements

for the Degree of

Doctor of Philosophy

in

Marine and Atmospheric Science

Stony Brook University

December 2010

Stony Brook University

The Graduate School

Key Hong Park

We, the dissertation committee for the above candidate for the
Doctor of Philosophy degree, hereby recommend
acceptance of the dissertation.

Dr. John E. Mak – Dissertation Advisor
Associate Professor, School of Marine and Atmospheric Sciences

Dr. Minghua Zhang – Chairperson of Defense
Professor, School of Marine and Atmospheric Sciences

Dr. Daniel Knopf
Assistant Professor, School of Marine and Atmospheric Sciences

Dr. Carl Brenninkmeijer
Adjunct Professor, SoMAS / Max Plank Institute for Chemistry, Mainz, Germany

Dr. Louisa K. Emmons
Atmospheric Chemistry Division, National Center for Atmospheric Research

Dr. Emmanuel Cosme
Associate Professor, Laboratory of Geophysical and Industrial Flows, University of Grenoble

This dissertation is accepted by the Graduate School

Lawrence Martin

Dean of the Graduate School

Abstract of the Dissertation

Joint Application of Concentration and Isotope Ratios to Investigate the Global Atmospheric Carbon Monoxide Budget: An Inverse Modeling Approach

by

Key Hong Park

Doctor of Philosophy

in

Marine and Atmospheric Science

Stony Brook University

2010

Since carbon monoxide is one of the major sinks of hydroxyl radicals, it has been used as a proxy of hydroxyl radicals, which largely control the oxidizing capacity of the atmosphere. Thus, CO-related chemistry directly or indirectly affects the abundance of other atmospheric trace gases including methane, halocarbons and tropospheric ozone. Carbon monoxide has also been shown its usefulness as a tracer of transport of pollution and fire emissions and as an additional constraint for CO_2 fluxes. Variations in the global CO cycle are closely related to the change of total source strengths. Previously, to estimate the global

CO budget, most inverse modeling techniques have been applied to concentration of CO only and showed large discrepancies in each source estimate. Since CO from certain sources may have a specific isotopic signature, the different isotopic species of CO provides additional information to constrain the sources. Thus, coupling the concentration and isotope fraction information can provide a better constraint on CO source strengths and lead to a more realistic global CO budget estimation.

In this thesis, MOZART-4, a 3-D global chemical transport model, was used to simulate the global CO concentration and its oxygen minor isotopologue, $C^{18}O$. Also, a tracer version (a tagged CO version) of MOZART-4 was developed to analyze contributions of each CO source, emission region and isotopologue efficiently. To validate model performance, CO concentrations and isotopic signatures measured from the Max Plank Institute for Chemistry, National Institute of Water and Atmospheric Research and Stony Brook University were compared to the modeled results over a nine year period. The model reproduced the observations fairly well and the averaged model-observation difference was 10.5ppbv for concentration and 3‰ for $\delta^{18}O$. Also, $\delta^{18}O$ of biomass burning source was estimated through the Keeling plot method and sensitivity test of $\delta^{18}O$ of biomass burning. Both methods suggest the $\delta^{18}O$ signature from biomass burning is higher than 20‰ which is significantly enriched compared to previous estimates.

Bayesian inversion techniques are used to calculate the most probable global CO budget based on observations and source strength. In the inversion analysis, oxygen isotope information is jointly applied with concentration information. The joint inversion results provide not only more accurate and precise inversion results in comparison with [CO]-only inversion. Also, various methods combining the concentration and isotopic ratios were tested to maximize the benefit of including isotope information. The joint inversion of [CO] and $\delta^{18}O$ estimated total global CO production at 2951Tg CO/yr, 3084Tg CO/yr and 2583Tg CO/yr in 1997, 1998 and 2004 respectively. The updated CO budget improved modeled concentration and oxygen isotope ratio and since the improvement was more clearly shown in oxygen isotope ratio, this implied that more accurate *a posteriori* sources are estimated.

Inversion analysis was performed with multi-year NOAA GMD [CO] to examine the interannual change of non-methane hydrocarbons oxidation source of CO which is directly affected by climate variation, such as El Niño/Southern Oscillation (ENSO) events. A close correlation between the NMHC oxidation source and ENSO events and the Earth surface temperature change was found. The interannual variation of NMHC oxidation source was ±52% from the mean and during a strong ENSO event in 1997 and 1998, global NMHC-derived CO increased by 74±13%.

Dedication

I dedicate this dissertation to my family. Particularly to my dear wife, Min Ju Kim, who has continuously encouraged and supported me during my pursuit of a doctoral degree, and to our precious daughter, Amy Seyeon Park, who is the joy of our lives. I must also thank my loving parents and terrific in-laws who have given me their fullest support.

Table of Contents

List of Figures

List of Tables

Acknowledgements

I would like to sincerely thank my advisor Prof. John Mak. He provided me the opportunity to explore atmospheric chemistry modeling and stable isotope geochemistry. Also, his guidance, support, understanding, and patience were essential to the completion of this dissertation.

I would also like to thank Dr. Louisa Emmons. This work would have been next to impossible without her invaluable guidance and help on MOZART model and inversion analysis.

I am also grateful to my committee members Prof. Minghua Zhang, Prof. Carl Brenninkmeijer, Prof. Daniel Knopf, and Prof. Emmanuel Cosme for their very helpful insights, comments and suggestions.

Finally, I would like to thank all of the members of the Mak's group especially Dr. Zhihui Wang and Tracey Evans for assisting and encouraging me in various ways during my course of studies.

1. Introduction

Since carbon monoxide (CO) is one of the major sinks of hydroxyl radicals (OH) [Brenninkmeijer et al., 1999; Houghton et al., 2001; Lewis et al., 2005], it has been used as a proxy of hydroxyl radicals, which largely control the oxidizing capacity of the atmosphere [Khalil and Rasmussen, 1994]. Therefore, CO and OH related chemistry directly and indirectly affects the abundance of other atmospheric gases including methane and halocarbons [Prather et al., 2001; Crutzen and Zimmermann, 1991] as well as, in conjunction with NOx, plays a central role in determining the abundance of tropospheric ozone, which is a green house gas and atmospheric oxidant [Thompson, 1992; Forster et al., 2007]. Carbon monoxide has also been shown its usefulness as a tracer of transport of pollution [Li et al., 2002; Shim et al., 2008] and fire emissions [Chen et al., 2009] and as an additional constraint for CO_2 fluxes [Palmer et al., 2006].

The variations of CO mixing ratio are closely linked with not only its sinks but also its sources. It is known that methane oxidation, fossil and biofuel combustion, nonmethane hydrocarbon (NMHC) oxidation, and biomass burning are the major sources of CO (Table 1.1). Its global averaged lifetime is relatively short (2~3 months) [Weinstock, 1969; [Pfister et al., 2004; Yurganov et al., 2005; Pfister et al., 2008a; Ho et al., 2009]. The complex distribution of the various

major sources obstruct estimating a reliable global CO budget [Brenninkmeijer and Rockmann, 1997; Brenninkmeinjer 1999]. Reaction with OH is the primary sink that removes approximately 90% of CO from the atmosphere [Hauglustaine et al., 1998; Logan et al., 1981; Weinstock and Niki, 1972, IPCC 2001, Bergamaschi 2000a] and about one tenth of this is removed through surface deposition [Rockmann et al., 1998; Sanhueza et al., 1998; Bergamaschi et al., 2000a].

Source strengths of atmospheric trace gases are commonly assessed by two different methods: top-down estimation and bottom-up estimation. The bottom-up technique estimates the source strengths based on socioeconomic, energy, land use and environmental data. However, sources assessed by this method have disagreed with atmospheric measurements by factors of two or more (SF_6 [Levin et al., 2010], HFCs [Stohl et al., 2010], PFCs [Mühle et al., 2010] and NF_3 [Weiss et al., 2008]) because this method combines the factors having different properties such as numbers of cows and fuel consumption and frequently the reported statistical data which itself has a large uncertainty as well [Tanimoto et al., 2008; Pfister et al., 2006]. The top-down method has been used to overcome the drawbacks of bottom-up estimates by constraining the source inventories using observational data of chemical species and atmospheric chemical transport model [Pfister et al., 2006].

Table 1.1 Estimates of the global tropospheric CO budget (TgCO/year)

	Duncan et al., 2007	***IPCC 2001***
Sources		
Oxidation of CH_4	778 - 861	800
Oxidation of Isoprene	170 - 184	270
Oxidation of Terpene	68 - 71	~ 0
Oxidation of industrial NMHC	102 -106	110
Oxidation of biomass NMHC	45 - 57	30
Oxidation of Methanol	95 - 103	-
Oxidation of Acetone	21	20
Vegetation	-	150
Oceans	-	50
Biomass burning	406 – 516	700
Fossil and domestic fuel	550 - 570	650
Total sources	2236 - 2489	2780
Sinks		
OH reaction	1500 – 2700	
Surface deposition	250 - 640	

Previously, most top-down estimates of CO source strengths [Bergamaschi et al., 2000b; Kasibhatla et al., 2002; Pétron et al., 2002; Arellano et al., 2004; Pétron et al., 2004; Müller and Stavrakou, 2005; Arellano et al., 2006] have used only concentration observations. They used inversion analysis techniques to estimate CO source strengths based on most probable source strength distributions

that minimize the model-observation difference. Whether past inversion analyses used satellite measurement or direct measurements (surface or aircraft) for constraining CO sources, there were discrepancies of up to 30% in total estimates of the CO inventory (Figure 1.1). However, the amount of each individual source can have larger variations in its estimates: 15% for methane oxidation, which is the best constrained source of CO; 20% for anthropogenic sources (fossil + biofuel), the next best constrained CO source; 50% for biomass burning and 100% for biogenic hydrocarbon oxidation. Even when considering the typical uncertainty of the aggregate major CO source strength estimates (< 15%) of the previous studies, the discrepancies among each source estimate are still significant. Despite large discrepancies of each source estimate, each past study showed improved modeled concentrations when they applied their updated source inventory. However, this does not confirm that their *a posteriori* source estimates are correct since there are many emission scenarios that lead to an accurate simulated *a posteriori* CO. An accurate estimate of individual CO sources is required to understand the current atmospheric chemistry environment and to predict future changes of CO.

Since isotopes of CO from different sources may have different isotope ratio, in optimization of CO source strengths, isotope measurements provide essential information for finding more realistic estimates. In carbon monoxide, both carbon and oxygen have stable isotopes. In most of Earth's environment, the

stable isotopic composition of carbon is 98.89% ^{12}C and 1.11% ^{13}C and that of oxygen is 99.76% ^{16}O, 0.04% ^{17}O and 0.2% ^{18}O.

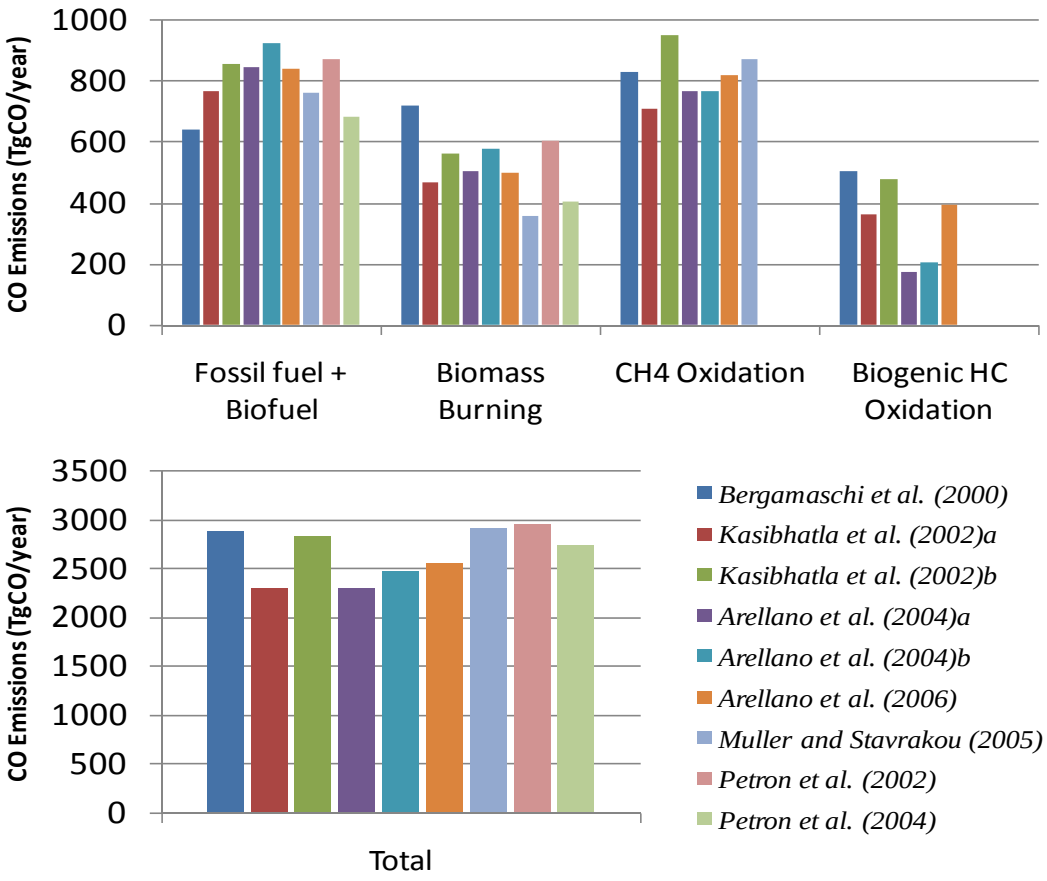

Figure 5.1 CO sources and total amount of CO emissions derived from inversion analyses

The fractionation of isotopes occurs in most biological, physical and chemical processes of the atmosphere and the Earth's surface. Thus the abundance of the minor stable isotopes is a reflection of the specific mechanisms leading to

its production. For instance, during a combustion process such as biomass burning, more $C^{18}O$ is produced from the higher burning temperature and $\delta^{18}O$ is close to 23.5 ‰ which is $\delta^{18}O$ of atmospheric O_2. Combined with concentration data, the stable isotope data should provide more constraints on the relative strengths of CO [Beregamaschi et al., 2000b; Tans, 1997; Brown, 1995; Rayner et al., 2008].

Table 1.2. Isotope Composition of CO sources

Sources	**$\delta^{18}O$, ‰**	**$\delta^{13}C$, ‰**
Fossil fuel combustion	+23.5[a,b], +24[e], +22[g]	-27.5[a]
	+25.3[i] (gasoline)	
	+15.1[i] (diesel)	
Biomass Burning	+16.3[b], +18±1[e]	-21.3[c], -24.5[d]
	+3~+18.4[j] (smoldering)	
	+16.2 ~ +26.0[j] (flaming)	
Methane oxidation	0[b,g], +15[e]	-52.6[f]
NMHC oxidation	0[b,g], +14.9[e]	-32.2[e]
Biogenic	?[h]	?[h]
Oceans	+15[h]	-40[h]

[a] *Stevens et al.* [1972];[b] *Brenninkmeijer* [1993];[c] *Conny et al.* [1997];[d] *Conny* [1999];[e] *Stevens and Wagner* [1989]; [f] Values based on the $\delta^{13}C_{CH4}$ (-47.2 ‰ [*Quay et al.*, 1991], and the fractionation in CH_4 + OH (5.4 ‰);[g] *Brenninkmeijer and Röckmann* [1997];[h] *Nakagawa et al.* [2004];[i] *Tsunogai et al.* [2003];[j] *Kato et al.* [1999];[h] *no data has been reported*

The isotope ratio is compared to the ratio in a standard material and

expressed as:

$$\delta = (\frac{R_{sample}}{R_{standard}} - 1) \times 1000 \quad (per\ mil, ‰) \qquad \text{(Eqn. 1.1)}$$

where R is the ratio of the minor isotope to the major isotope (eg. $^{18}O/^{16}O$ or $^{13}C/^{12}C$) and VSMOW(Vienna Standard Mean Ocean Water) [Coplen, 1994; Gonfiantini, 1978] and VPDB(Vienna Pee Dee Belemnite) [Craig, 1957; Gonfiantini, 1978] is used for the standard isotope ratio of $\delta^{18}O$ and $\delta^{13}C$ in CO, respectively.

There have been several $\delta^{18}O$ and $\delta^{13}C$ values reported for the main sources of carbon monoxide (Table 1.2). Since $\delta^{13}C$ and $\delta^{18}O$ signatures of each CO source are uncorrelated (Figure 1.2), each carbon and oxygen isotope contains its own isotopic source signature and can be independently applied in the budget optimization [Bergamaschi et al., 2000b; Rockmann et al., 2002]. Sometimes, the C or O isotope composition of a certain source is clearly different from the other sources. In that case, the isotope composition is very useful to separate that source from the others. For instance, the carbon isotope ratio ($\delta^{13}C$) of carbon monoxide derived from methane oxidation is obviously depleted (-52.6‰) compared to the other source signatures (Figure 1.2). Likewise, the oxygen isotopic signature clearly separates combustion source such as fossil fuel combustion, biofuel use and biomass burning from the other non-combustion sources.

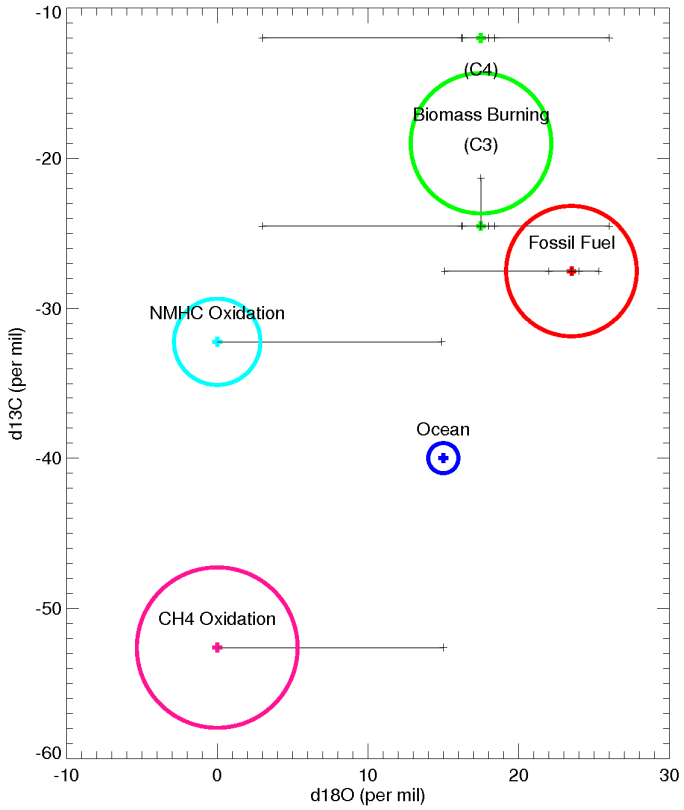

Figure 1.2 Isotopic source signatures of CO based on data in Table 1.2. The size of each circle represents the relative source strengths estimated in IPCC 2001.

Despite the potential advantages of including isotope data to the CO budget estimation, because of the lack of observations, their inclusion has been limited [Bergamaschi et al., 2000b]. Also, for some CO sources, there exist large uncertainties in isotopic source signature [Stevens, 1989; Kato et al., 1999; Brenninkmeijer, 1993; Brenninkmeijer and Rockmann, 1997], and for some other sources such as direct biogenic CO emission source there is no direct information for the isotopic source signature. In addition to this, each source of atmospheric

CO itself has a wide range of $\delta^{18}O$ values in its subcategories. For instance, $\delta^{18}O$ of CO from biomass burning is a function of burning temperature (smoldering phase and flaming phase), by $\delta^{18}O$ of precipitation, i.e. latitude and by the isotopic composition of each vegetation species [Kato et al., 1999; Richter et al., 2008]. In the case of CH_4 and NMHC oxidation, not only is there no direct measurement of oxygen isotope ratios but also the mechanisms of oxygen addition and fractionation in their oxidation chains are poorly known. Hence while more accurate results are expected with detailed assignment of oxygen isotope source signatures by vegetation distribution, burning type and isotope ratios of the precipitation, this cannot be included in the model without further detailed studies of isotopic source signatures of each source. However, since source strengths are estimated on the global or hemispheric scale, one can apply globally averaged isotope source signatures and this may reduce the influence of uncertainties of isotope source signatures in the isotope model simulation. More details about incorporation of isotopes in the model are discussed in chapter 3.

In this study, MOZART-4 (Model for OZone And Related chemical Tracers) [Emmons et al., 2010] which is one of the most accurate 3-D global chemical transport model (GCTM) [Shindell et al., 2006] for carbon monoxide simulation and included the latest observational concentration and isotope data was used. A successful model performance is important for CO isotope analysis helping to interpret the measurements since its observational data sets are very

limited in both sampling locations and periods for its measuring difficulty. Simulation results of CO mixing ratios and isotopic signatures agree fairly well with observations. A detailed discussion about the modeled concentration and isotope ratio is presented in chapter 5.

Including isotope information in an inversion study presumably leads to more accurate and precise source strength estimates [Enting, 2002], since isotope measurements not only provide information of the sources but also double the observational data sets, i.e. to [$C^{16}O$] and [$C^{18}O$] and [^{12}CO] and [^{13}CO]. Also, optimized isotope ratios which are updated modeled isotope ratios derived from improved inventories (*a posteriori* source strengths) can be used to confirm the inversion results and this adds more reliability to the inverse modeling results. There have been several concentration-isotopic ratio inversion schemes that applied to find the best source strength estimates of atmospheric trace gases [Bergamaschi et al., 2000b; Rayner et al., 2008; Tans et al., 1993; Ciais et al., 1995; Houweling et al., 2008; Brown, 1995; Mikaloff-Fletcher et al., 2004]. However, previous inverse modeling analyses did not fully use the benefit of applying isotope information in source optimization of atmospheric trace gases. For instance, in Mikaloff-Fletcher et al., 2004, carbon isotopes in CH_4 were not independently used to constrain the source of methane since they merged both concentration and isotope information in their inversion method. For carbon monoxide, [Bergamaschi et al., 2000b] pioneered and extensively investigated on

the atmospheric CO mixing ratio and isotopic signatures ($\delta^{13}C$ and $\delta^{18}O$) with both direct measurements and chemical transport model results to estimate the global CO budget. Although that study contained some shortcomings which will be discussed later in this chapter, it showed that isotope information can constrain the CO sources more effectively and adds more reliability to the inversion results.

[Bergamaschi et al., 2000b], adopted the inversion technique described in [Hein et al., 1997 GBC] which optimized the sources of methane based on [CH_4] and its C-isotope information. While CH_4 isotope inversion method can analogously be used to invert CO source strengths, seasonal variations of CO isotope signatures are much bigger than that for methane isotopes. Thus, the scheme should have been modified for more sophisticated source estimation because the linearity approximation for the methane isotopes is no longer valid for carbon monoxide isotopes [Hein et al., 1997 GBC]. Plus, the study did not include concentration data in the analyses from the five stations out of 31 stations having isotope ratio data. Thus, concentration dominantly constrained the sources and the benefits of isotope measurements were diminished. The benefit of including the isotope information could be maximized if there were an appropriate weighting between the concentration and isotope data sets and the effect of each data set is well-balanced. The reproducibility of measurements by the GCTM is essential to the accurate source estimation since, even though uncertainties of the model are incorporated in the inversion analyses, the *a posteriori* source strengths are

derived from the simulated Jacobian matrix containing the relation between the sources and concentration and/or isotope ratios. In Bergamaschi et al., 2000b, the forward model run results in a large difference from the measured concentration and isotope ratios. This implies a more reliable inversion result can be derived if the mechanisms of the model, including the chemistries and transports, are improved. The goal of the work presented here is to improve and develop a new joint inversion method of [CO] and its isotopes for accurate CO budget estimation. In this study, CO source optimization methods which maximize the benefit of including isotope information are vigorously and widely investigated. The availability of a more realistic and enhanced 3-D global chemical transport model and updated isotopic ratio measurements enables a more robust CO inversion analysis.

While both carbon and oxygen isotope measurements are available, only the oxygen isotopologues $C^{16}O$ and $C^{18}O$ are studied in this thesis. Since the minor isotope ratio to the major isotope ratio of carbon ($^{13}C/^{12}C$) is greater than that of oxygen ($^{18}O/^{16}O$), uncertainties in the carbon isotope measurement are relatively smaller than that in oxygen isotope. Thus, previous CO isotope studies have been more weighted on carbon-related isotopologues of CO [Manning et al., 1997; Bergamaschi et al., 2000b, Kato et al., 1999, Nakagawa et al., 2004]. However, for constraining the sources of CO, the isotope ratios of carbon are very similar in some of the main CO sources such as fossil fuel combustion, NMHC

oxidation and biomass burning, while the isotope ratios of oxygen are distinctively different in those CO sources, suggesting a greater potential to separate those sources [Manning et al., 1997; Brenninkmeijer et al., 1999; Mak et al., 2003]. Despite the clear separation of methane derived CO from other sources based on carbon isotope ratio, the methane source is already well constrained, in comparison with the other sources of CO, because of methane's long lifetime and known atmospheric concentration. This study focuses on the oxygen isotopes of CO because oxygen isotope information is unique for understanding the global CO budget.

The outline of the thesis is as follows. Carbon monoxide concentration and its oxygen isotope ratio measurements used in this study are described in chapter 2. In chapter 3, detailed descriptions about the forward model simulation including *a priori* source inventory and incorporation of $C^{18}O$ are presented. Next, the development of various joint inversion schemes combining concentration and isotope ratio information are presented and discussed. The sensitivity of inversion results to uncertainties in the observations and *a priori* source strengths are also discussed (chapter 4). Results of forward modeled concentration and isotope ratios are presented and evaluated by comparing with observations. After discussing the effects of each source of CO to the isotope ratio at each station and other factors affecting $\delta^{18}O$ and concentration of atmospheric CO, possible ideas to decrease uncertainties of $\delta^{18}O$ of CO sources and CO source

strengths are suggested (chapter 5). In chapter 6, the results of inverse modeling analysis including the optimized source strengths are presented and discussed. In addition, a detailed analysis of the interannual variability of CO sources deduced from the multi-year inversion of NOAA GMD [CO] measurements [Novelli et al., 1998a; Novelli et al., 2003a] is given.

2. Observation of Atmospheric Carbon Monoxide and Its Isotopes

2.1 Observational data

Atmospheric carbon monoxide mixing ratios and isotope ratios have been measured from eight stations: Alert, Canada; Spitsbergen, Norway and Sweden; Izaña, Spain; Baring Head, New Zealand; Scott Base, Antarctica; Mauna Loa, United States; Ragged Point, Barbados; and Westmann Island, Iceland. Station locations are shown in Figure 2.1. Investigators from the Max Plank Institute for chemistry (MPI), Germany measured [CO], $\delta^{13}C$ and $\delta^{18}O$ at Alert, Spitsbergen and Izaña [Braunlich et al., 1998; Rockmann et al., 1999]. Investigators from the National Institute of Water & Atmospheric Research (NIWA), New Zealand measured these species at the two Southern Hemispheric stations: Baring Head and Scott Base [Brennikmeijer, 1993; Moss et al., 1998]. Observations from Mauna Loa, Barbados and Iceland stations were made by Professor Mak's group at Stony Brook University [Mak et al., 2003]. Most air samples were collected weekly or biweekly.

Table 2.1 shows the periods of [CO], $\delta^{13}C$ and $\delta^{18}O$ observations at each sampling location. Also shown is the period of model simulation. Southern Hemisphere stations (Scott Base and Baring Head) have both concentration and

isotope ratio measurements covering most of the simulation time period: mid-1996 to 2004. Excluding January through June 2000 at Scott Base, each sampling location in the Southern Hemisphere has two periods which missed two consecutive months' observations: 9 ~ 10/1997 and 10 ~ 11/2004 for Scott Base and 10 ~ 11/1997 and 1 ~ 2/2002 for Baring head. For the Northern Hemisphere measurements, 1997 and 1998 observations from the Spitzbergen, Izaña and Barbados stations were used and 1997 observations from Alert were used. Observations from Iceland and Mauna Loa made during 2004 were also used. Monthly averaged concentration and isotope ratios were used in the inversion analyses and if data was missing, the record was interpolated.

Table 2.1 Data availability during the model simulation period (April 1996 ~ December 2004)

Year	96	…	96	…	97	97	97	97	97	98	…	98	…	99	99	99	…	99	…	00	00	00	…	01	…	01	02	02	02	…	03	…	04	…	04	04	04	04
Month	4	…	10	…	8	9	10	11	12	1	…	10	…	4	5	6	…	12	…	5	6	7	…	3	…	12	1	2	3	…	8	…	1	…	9	10	11	12
MODEL	Spin-up																																					
SCO																																						
BHD																																						
ICE																																						
ZEP																																						
ALT																																						
MLO																																						
IZO																																						
RPB																																						

The methodology of the sampling technique and measurement are nicely described in [Brenninkmeijer, 1993; Mak and Brenninkmeijer, 1994]; Mak and Kra, 1999]. Also, a subset of the NOAA GMD network CO mixing ratios [Novelli

et al., 1998b; Novelli et al., 2003b] were used in some inversion analyses. Each concentration and isotope ratio data set was inverted individually or together to update CO source strengths.

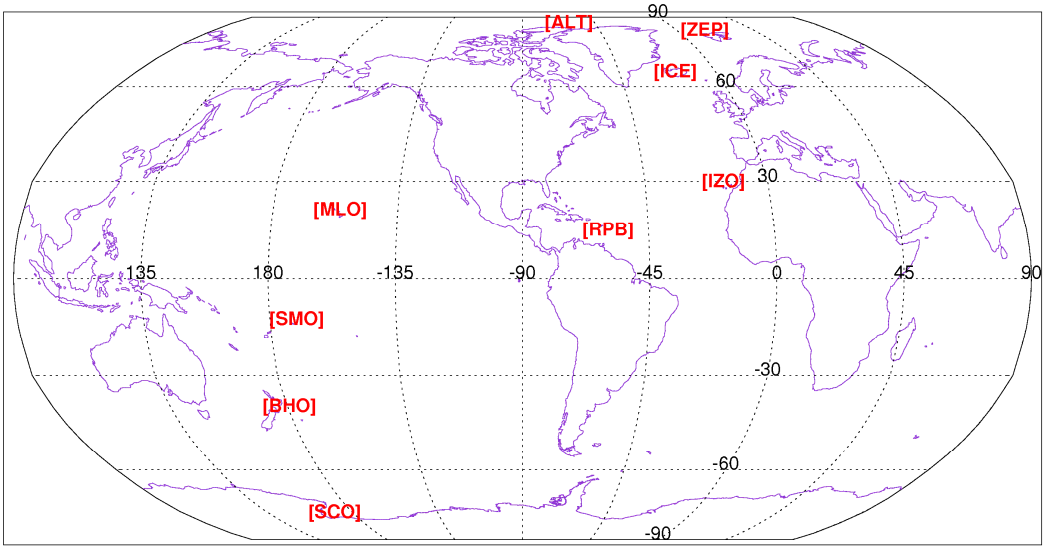

RPB Ragged Point, Barbados 13 10'N 59 26'W 13.17, 300.57 -59.43 lon
ICE Heimaey, Iceland 63 15'N 20 09'W 63.25, 339.85 -20.15 lon
MLO Mauna Loa, Hawaii 19 32'N 155 35'W 19.53, 204.42 -155.58 lon
SMO Tutuila, American Samoa 14 15'S 170 34'W -14.25, 189.43 -170.57 lon
IZO Tenerife, Canary Islands 28 18'N 16 29'W 28.30, 343.52 -16.48 lon
ZEP Spitsbergen, Norway/Sweden 78 54'N 11 53'E 78.90, 11.88 11.88 lon
ALT Alert, N.W.T., Canada 82 27'N 62 31'W 82.45, 297.48 -62.52 lon
BHO Baring Head, New Zealand 41 18'S 179 54'E -41.30 179.90 179.90 lon
SCO Scott Base, New Zealand 77 51'S 166 46'E -77.85 166.77 166.77 lon

Figure 6.1 Measurement stations for [CO] and isotope ratios

Since measuring isotopic ratios in CO is more difficult than measuring CO concentration, there is much less CO isotope data. However, because the average lifetime of tropospheric CO is approximately 2-3 months (60N-90N:8-9 months, 30N-60N: 3 months, tropics: 2 months, 30S-60S: 4-5 months, 60S-90S: 1year) [Pfister et al., 2008a], the gas is zonally well mixed in the atmosphere and its inter-hemispheric mixing is very limited [Petron et al 2002, Williams et al 2002,

also discussed in chapter 5]. Thus, since sampling locations were carefully selected to represent the background state of the atmosphere at specific latitude zones, the current number of sampling stations is sufficient to constrain the annual CO sources emissions on the hemispheric scale. This is demonstrated in Figure 2.2, showing little difference between the CO measurements used here when compared to the multi-year average of the NOAA GMD CO measurements from all background stations.

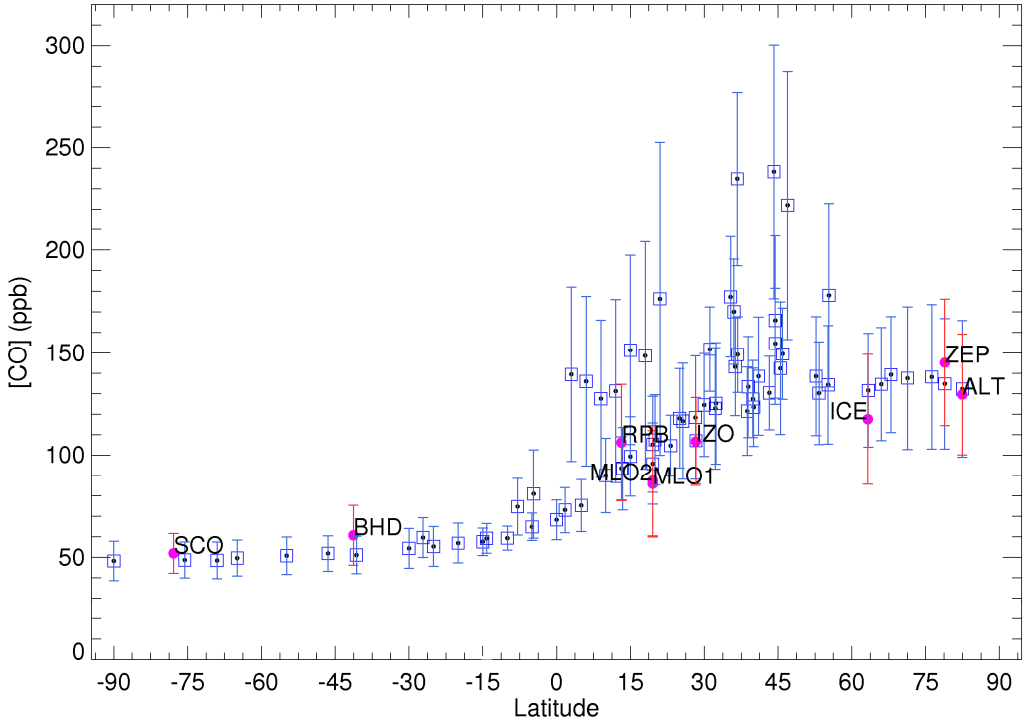

Figure 2.2 Global zonal distribution of CO concentration. The blue squares are NOAA GMD [CO] and the red dots are [CO] used in this study. The error bar is the range of mean seasonal variation of the multi-year CO observations

2.2 Measurement of concentration and isotope ratios of CO

Isotope ratios and concentration of atmospheric CO are determined based on the methods described in Brenninkmeijer, 1993 and Mak and Brenninkmeijer, 1994. A brief description of the isotope analyzing method is as follows. Air samples are collected in high pressure aluminum cylinders using a custom built clean air Rix piston compressor. Samples are transported to the laboratory and the collected air samples are processed through a cryogenic vacuum extraction line. Water vapor and most trace gases are trapped in the first two cryogenic traps and CO is oxidized to CO_2 by Schütze reagent [Smiley, 1949]. The converted CO_2 is collected in the last cryogenic trap. Concentrations are determined by measuring the total pressure of the oxidized CO in a calibrated volume, and its isotopes are measured in an isotope ratio mass spectrometer. The manometrically measured CO mixing ratios are pretty consistent with the NOAA GMD CO measurements (Figure 2.2) which were made by gas chromatography/HgO reduction gas detector [Novelli et al., 1992, 1998a]. Also, informal intercomparisons have been done between Mak and Brenninkmeijer and Novelli and Brenninkmeijer [Brenninkemijer, personal communication]. The oxygen isotope ratio of CO_2 is directly converted to $\delta^{18}O$ of CO using this equation:

$$\delta^{18}O_{CO} = 2\,\delta^{18}O_{CO2} - (2\,\delta^{18}O_{cal,\,CO2} - 2\,\delta^{18}O_{cal,\,CO}) \qquad \text{(Eqn. 2.1)}$$

where, $\delta^{18}O_{CO2}$ and $\delta^{18}O_{cal,\,CO2}$ are the measured signature of the CO-derived CO_2 from the air sample and calibration gas respectively, $\delta^{18}O_{cal,\,CO}$ is $\delta^{18}O$ of CO in

calibration gas and $\delta^{18}O_{CO}$ is the isotope signature of CO in the sample [Mak et al., 1999]. The precision of measurement is ±2 ppbv for concentration, ±0.2 per mil for $\delta^{13}C$ and ±0.8 per mil for $\delta^{18}O$ [Mak and Brenninkmeijer, 1994; Mak et al., 2003].

3. Forward Model Description

3.1 Model for OZone And Related chemical Tracers 4 (MOZART-4)

In order to get the global distribution of carbon monoxide and its isotopic signatures, MOZART-4 [Emmons et al., 2010] was used. MOZART-4 is a 3-dimensional global chemical transport model developed by investigators of the National Center for Atmospheric Research, the Max-Planck-Institute for Meteorology, and NOAA/GFDL. MOZART-4 is an updated version of MOZART-2 [Horowitz et al., 2003]. MOZART-4 includes more than 97 chemical and aerosol species with more than 196 chemical reactions and dry depositions. MOZART-4 does not require a specific meteorological field data. Thus, it can be driven by either modeled meteorology or assimilated meteorological observations such as National Center for Environmental Prediction (NCEP) or European Centre for Medium Range Weather Forecasts (ECMWF) reanalyzed wind fields [Emmons et al., 2006]. In past studies, MOZART-4 reproduced certain observations fairly well for carbon monoxide [Pfister et al., 2005], ozone [Pfister et al., 2006], isoprene nitrates [Horowitz et al., 2007], aerosol optical depth [Pfister et al., 2008b], and isoprene [Pfister et al., 2008a]. MOZART-4 also has shown good agreement with other model simulations; carbon monoxide [Shindell et al., 2006] and ozone [Stevenson et al., 2006]. A more detailed description of

MOZART-4 and a general evaluation of model performance is given in [Emmons et al., 2010].

3.2 Tracer version of MOZART-4

In this study, the tracer version of MOZART-4 [Petron et al., 2004] [Pfister et al., 2008a; Emmons et al., 2010] is developed and used. In this study, only chemical reactions and species directly related to carbon monoxide are included in the model. It has simple chemical reactions and uses prescribed mixing ratios and other parameters including OH concentration and chemical production rates. This information is pre-calculated and saved from the simulation of a full-chemistry version of MOZART-4. Therefore, the code of the tracer version is more flexible and requires less effort for building or implementing new chemistries. Also, simulation time is saved due to its simplified chemistry. Thus, the tracer version is much faster than the regular version of MOZART-4 without losing the advantages of MOZART-4 and the results can be more efficiently analyzed.

To understand the global distribution of CO more clearly, CO is tagged by each source, isotopologue, and geographic regions of origin which enables tracking the CO and its isotopes easily; $C^{16}O$ and $C^{18}O$ from each source and each geographic region were treated as independent tracers with the same chemical and

physical characteristics such as reaction rates and deposition velocities. Methane oxidation, NMHC oxidation, biomass burning, fossil fuel use, biofuel use, direct biogenic emission and oceanic sources comprised the sources of CO in the model. Fossil fuel use, biofuel use and biomass burning sources were divided into 9 emission regions: North America, Central America, South America, North Asia, South Asia, Australia, Europe, North Africa and South Africa. Hence, 62 tagged tracers are included in the model.

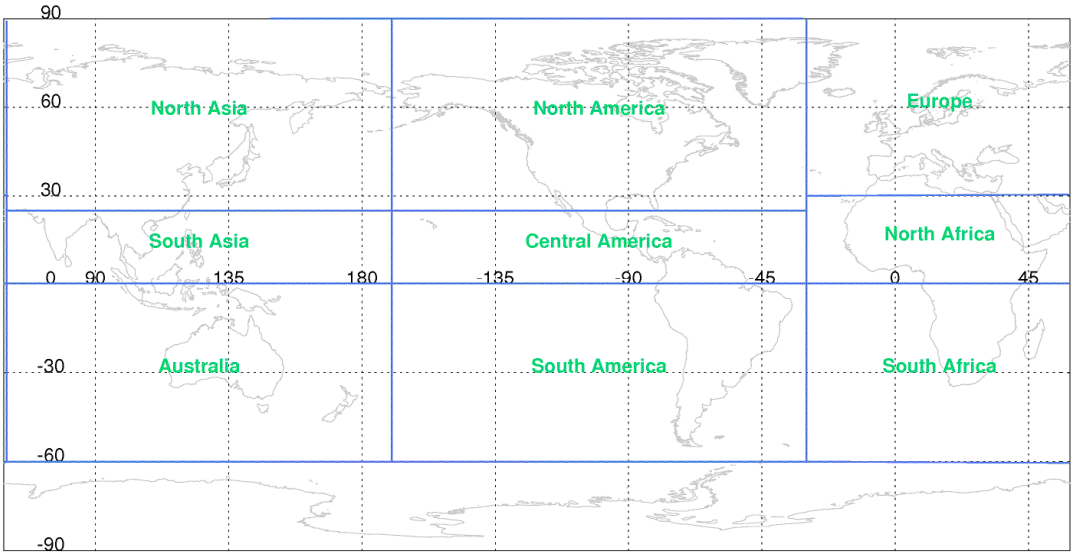

Figure 7.1 Partition of 9 regions for fossil fuel, biofuel and biomass burning emission

3.3 Sources and sinks of atmospheric CO

In this study, *a priori* CO source strengths are taken from various previous studies and/or atmospheric gas inventory data sets such as POET (Precursors of

Ozone and their Effects in the Troposphere) [Olivier et al., 2003], GEIA (Global Emission Inventory Activity; available at http://www. http://geiacenter.org) [Lawrence et al., 1999] and EDGAR (Emission Database for Global Atmospheric Research) [Olivier et al., 1996]. The global budget of CO sources used in this study is shown in Table 3.1 and 3.2.

Carbon monoxide emissions from fossil fuel and biofuel use are taken from [Pétron et al., 2004] which constrained the sources with the most recent CO observations among the CO inversion analyses and updated the inventory monthly for 15 regions. They derived CO source strengths from April 2000 to March 2001 using MOPITT (Measurement Of the Pollution In The Troposphere) satellite measurement data. Fossil fuel and biofuel emissions are updated monthly from the EDGAR-3 [Olivier and Berdowski, 2001] inventory. The inversion result indicated that fossil fuel and biofuel CO emissions in winter months are 30% and 100% higher than in summer months. Also, they found that East Asia is the strongest anthropogenic (fossil + biofuel) CO emitter which accounts for 20% of global anthropogenic CO. In Figure 1.1, previous anthropogenic CO inventories are shown and *a priori* anthropogenic used in this study (679 TgCO/year) is little lower than the average (799 TgCO/year). The monthly source estimates of biofuel and fossil fuels sources are repeatedly used for multi-year forward simulations.

Table 3.1 *a priori* source strengths used in this study (TgCO/year)

Sources	Northern Hemisphere	Southern Hemisphere
Fossil fuel	340	25
Methane oxidation	497	379
NMHC oxidation	310	232
Biofuel	276	38
Biogenic	104	57
Ocean	8	12

The Global Fire Emissions Database (GFED) version 2 [van der Werf et al., 2006] inventory is used for the biomass burning source of carbon monoxide. The inventory data set was compiled using satellite data and the Carnegie-Ames-Stanford-Approach (CASA) biogeochemical model [van der Werf et al., 2003; Potter et al., 1993; Field et al., 1995; Randerson et al., 1996]. This data set consists of 1˚ x 1˚ gridded monthly burned area, fuel loads, combustion completeness, and fire emissions of carbon (C), carbon dioxide (CO_2), carbon monoxide (CO), methane (CH_4), non-methane hydrocarbons (NMHC), molecular hydrogen (H_2), nitrogen oxides (NO_x), nitrous oxide (N_2O), particulate matter ($PM_{2.5}$), total particulate matter (TPM), total carbon (TC), organic carbon (OC), and black carbon (BC) for the time period January 1997 - December 2004. Annual CO emissions estimated by the GFED-v2 are shown in Table 3.2.

Carbon monoxide is also directly emitted from other natural sources: plants and the ocean. Carbon monoxide emissions from live or dead plant matter

are from the photodegradation or photooxidation of cellular material [Tarr et al., 1995] and oceanic CO is mainly produced by the photochemical oxidation of dissolved organic matter (DOM) [Wilson et al., 1970; Bauer et al., 1980; Conrad and Seiler, 1980; Conrad et al., 1982]. The inventories of these natural sources are taken from the POET atmospheric gas inventory [Olivier et al., 2003]. The inventory provides a CO source estimates based on net primary productivity, temperature and vegetations type [Erickson, 1989; Müller and Brasseur, 1995]. The CO emissions from the sources are shown in Table 3.1 and their monthly inventory estimates were used for each modeling year.

Table 3.2 GFED-v2 inventory of Biomass burning CO (TgCO/year)

Year	Northern Hemisphere	Southern Hemisphere
1997	192	364
1998	397	193
1999	221	171
2000	199	137
2001	193	171
2002	222	196
2003	235	161
2004	192	212

Methane-derived CO is the most accurately constrained CO source [Mak et al., 2003] because of its long lifetime (~10 years) [Emmons et al 2010; Horowitz et al., 2003; Lawrence et al 2001], known atmospheric concentration,

and well-known oxidation rate. Carbon monoxide from methane oxidation is calculated on-line. In MOZART-4, CH_4 concentration at the surface is set to the zonal average of the monthly mean NOAA GMD surface measurements.

In the full-chemistry version of MOZART-4, photochemical reactions of hydrocarbons also produce CO in the model. Hydrocarbon concentrations are calculated on-line, using emissions of NMHCs and chemical mechanisms of NMHC oxidation as described in [Emmons et al., 2010]. Vegetation emission of isoprene and monoterpenes are calculated using MEGAN (Model of Emissions of Gases and Aerosols from Nature) [Guenther et al., 1995; Guenther et al., 2006]. In the tracer version of MOZART, NMHC-derived CO is calculated by subtracting on-line calculated CO from CH_4 oxidation from the total chemical production (hydrocarbon oxidation) of CO from the full chemistry MOZART runs.

Reaction with hydroxyl radical is the dominant sink of tropospheric CO, responsible for around 90% of its removal and the rest of CO is removed by surface deposition [IPCC, 2001; Sanhueza et al., 1998; Bergamaschi et al., 2000b].

In the tracer version of MOZART, the distribution of hydroxyl radical (OH) concentration is read from a file produced from the full chemistry version of MOZART-4. Hydroxyl radical fields are pre-calculated from the MOZART-4 full chemistry run. Although the lifetime of methane is not linear to [OH], compared with 9.4 years [Horowitz et al., 2003] and 7.8-10.3 years [Lawrence et al., 2001], the calculated lifetime of methane from MOZART-4 run is 10.5 years [Emmons et

al., 2010], indicating the model may slightly underestimate globally averaged OH.

Surface deposition of CO is controlled by the activity of microorganisms in the soil. The soil uptake velocity is a function of soil moisture content of different ecosystems and is implemented in the standard version of MOZART-4 [Sanderson et al., 2003; Emmons et al., 2010]. The CO tracer version of MOZART-4 used the same surface deposition velocities.

3.4 Model setup

The MOZART-4 versions used in this study have a horizontal resolution of 2.8˚ × 2.8˚: 128 longitude points and 64 latitude points. There are 28 vertical levels from the surface to the top of the stratosphere (2hPa). Approximately 6 levels are included in the boundary layer and around 18 levels are in the troposphere. In this study, the model was driven by the NCAR reanalysis of the National Centers for Environmental Prediction forecasts (NCEP/NCAR reanalysis) [Kalnay et al., 1996; Kistler et al., 2001]. The chemical species are reacted and transported in the model every 20 minutes. Since the time step of the meteorological field is 6 hours, thus was interpolated to every 20 minutes. The modeled results are averaged and saved every 24 hours. The time period of model simulation was from April 1996 through December 2004, and the first six months' simulations were discarded since those months were considered as spin-up

months.

3.5 Incorporation of oxygen isotopes

To analyze the oxygen isotopes of CO in the model, each source of carbon monoxide was determined for $C^{16}O$ and $C^{18}O$ (Eqn. 3.1) and specific chemical reaction rates and deposition velocities assigned to each isotopologue.

First, to create CO isotope inventories, total CO inventory is divided based on $\delta^{18}O$ source signatures. For the direct emission sources such as biomass burning and fossil fuel use, the following equations derived from the definition of "delta (δ)" notation is used to divide each source inventory into $C^{16}O$ and $C^{18}O$ inventories (Eqn. 3.1).

$$\delta^{18}O_j = \left(\frac{\frac{^{18}O_j}{^{16}O_j}}{\frac{^{18}O_{standard}}{^{16}O_{standard}}} - 1 \right) \times 1000 \quad (per\ mil)$$

$$\Leftrightarrow \quad \frac{^{18}O_j}{^{16}O_j} = R_{standard} \times \left(1 + \frac{\delta^{18}O_j}{1000} \right), \quad R_{standard} = \frac{^{18}O}{^{16}O} \ (VSMOW)$$

Emission inventory (M) of a source j is $M_{CO_j} = M_{C^{16}O_j} + M_{C^{18}O_j}$ (Eqn 3.1)

then

$$M_{C^{16}O_j} = M_{CO_j} \times \frac{1}{1+Q}, \quad Q \equiv \frac{M_{C^{18}O_j}}{M_{C^{16}O_j}} = \frac{[C^{18}O]_j}{[C^{16}O]_j} \quad at\ a\ source\ point$$

$$M_{C^{18}O_j} = M_{CO_j} \times \frac{Q}{1+Q}$$

Carbon monoxide produced from the CH_4 + OH reaction in the model is separated by the online calculation since it is chemically produced and not emitted from the surface. Methane-derived $C^{16}O$ and $C^{18}O$ is calculated from:

$$CH_4 + OH \rightarrow 0.99799882 \times CO_{methane} + 0.00200118 \times C^{18}O_{methane} \quad \text{(Eqn. 3.2)}.$$

where the multipliers are the relative abundance of $C^{16}O$ and $C^{18}O$ for $\delta^{18}O$ = 0‰.

Oxidation reactions of each isotopologue are individually treated in the model since isotopic fractionation occurs during the CO + OH reaction (kinetic isotope effect: KIE). The KIE is defined as the ratio of reaction rate constants of each isotope: $KIE(\delta^{18}O) = k(C^{16}O)/k(C^{18}O)$ where $k(C^{16}O)$ and $k(C^{18}O)$ represent reaction constant of $C^{16}O$ + OH and $C^{18}O$ + OH respectively. When CO is

oxidized by hydroxyl radical, the behavior of oxygen isotopes show an inverse mass dependence (inverse KIE). In normal cases, the light isotopes preferentially react (mass dependent KIE). Thus, carbon monoxide with the heavier oxygen isotope (^{18}O) is preferentially removed from the atmosphere (KIE = 0.990). This KIE is weakly dependent on pressure. The rate constant for CO + OH itself is strongly dependent on pressure [Stevens and Wagner, 1989; Röckmann et al., 1998]. The reaction rate of the CO + OH reaction and the reaction rate ratio between $C^{16}O$ and $C^{18}O$ are known as follow:

$$\begin{aligned} k_{CO+OH} &= 1.5\times10^{-13}\times(1+0.6\times p[\text{atm}]) \\ \eta(\delta^{18}O)_{CO+OH} &= (KIE-1)\times1000 \\ &= -11.6+0.0042\,p-1.9\times10^{-6}\,p^2 \end{aligned} \qquad \text{(Eqn. 3.3)}$$

Carbon monoxide removal from soil uptake follows the normal KIE (KIE>1) and it is measured as $\eta(\delta^{18}O)_{soil\ sink}$ = 12‰ [Tsunogai et al., 2002].

The modeled $C^{16}O$ and $C^{18}O$ from different regions and sources are converted to total CO mixing ratios and $\delta^{18}O$ for the analyses using the following equations:

$$[CO]_{total} = \sum_{i,j}\left([C^{16}O]_{i,j} + [C^{18}O]_{i,j}\right)$$

$$\delta^{18}O = \left(\frac{\sum_{i,j}[C^{18}O]_{i,j} \Big/ \sum_{i,j}[C^{16}O]_{i,j}}{R_{standard}} - 1 \right) \times 1000 \qquad \text{(Eqn. 3.4)}$$

$$i = emission\ region,\ j = source$$

The isotopic source signature from fossil fuel combustion applied in this study is 23.5‰ [Stevens et al., 1972; Brenninkmeijer, 1993]. Based on [Brenninkmeijer, 1993] and [Brenninkmeijer and Röckmann, 1997], 0‰ is used for $\delta^{18}O$ signature from methane and NMHC oxidation source. Since there are two globally averaged estimation of $\delta^{18}O$ signature from biomass burning was reported (16.3‰: Brenninkmeijer, 1993 and 18±1‰: Stevensens and Wagner, 1989), a rough average of the estimates (17.5‰) is applied in the forward model. For the ocean source of CO, 15‰ is used in the model [Nakagawa et al., 2004].

Since there is no previous study on the oxygen isotopic source signature of directly emitted biogenic CO (CO_{bg}) and biofuel CO (CO_{bf}) (Table 1.2), $\delta^{18}O$ values from those sources are estimated in this study. $\delta^{18}O$ of CO from the direct biogenic emission was estimated at 0‰ which is same as that from hydrocarbon oxidation sources because, while the factors controlling this source are not well known [Guenther et al., 2000], this is also produced from the photochemical reactions [Tarr et al., 1995]. The biogenic source of CO is minor source of CO

(60~160 TgCO/year) [Brenninkmeijer et al., 1999] thus uncertainties originated from this assumption should not affect largely to the modeled results. The isotopic source signature from biofuel use is assumed to be the same as $\delta^{18}O$ of CO from biomass burning, since CO from the two sources originates from the same process: ‘burning wood or plants’.

4. Methodology for Inverse Modeling Analysis

4.1 Bayesian synthesis inversion

In this study, the Bayesian inversion method was used to find the best estimates of source strengths of atmospheric carbon monoxide. Since the Bayesian approach allows for the incorporation of prior information about the unknown parameters to the inversion procedure, it is a very useful method to solve the inverse problem, especially if one wants to update parameters having some prior understanding or experience. Since Bayes' theorem originates from probability theory, both the formulation of this technique and its solution is provided as a probability density function. Even if observations contain some errors or prior knowledge is imperfect the Bayesian approach can provide a solution with those uncertainties quantified as probability distributions [Heimann and Kaminski, 1999; Rodgers, 2000; Aster et al., 2005].

Assuming a Gaussian distribution for all probability distributions and a linear relationship between sources and concentrations [Bergamaschi et al., 2000a; Bergamaschi et al., 2000b; Pétron et al., 2002; Arellano et al., 2004; Müller and Stavrakou, 2005; Arellano et al., 2006], the measured concentration of CO can be expressed as:

$$\mathbf{y} = \mathbf{K}\mathbf{x} + \mathbf{e} \qquad \text{(Eqn. 4.1)}$$

where **y** is the observed concentrations of CO, **x** is the vector of each carbon monoxide source strength, **K** is the Jacobian matrix that links concentration and source strength calculated from the forward chemical transport model and **e** is the total error of measurement and model. Since **K** describes the sensitivity of CO concentration to the source change, **Kx** represents a modeled concentration of CO that expressed as sum of the concentration of each source category.

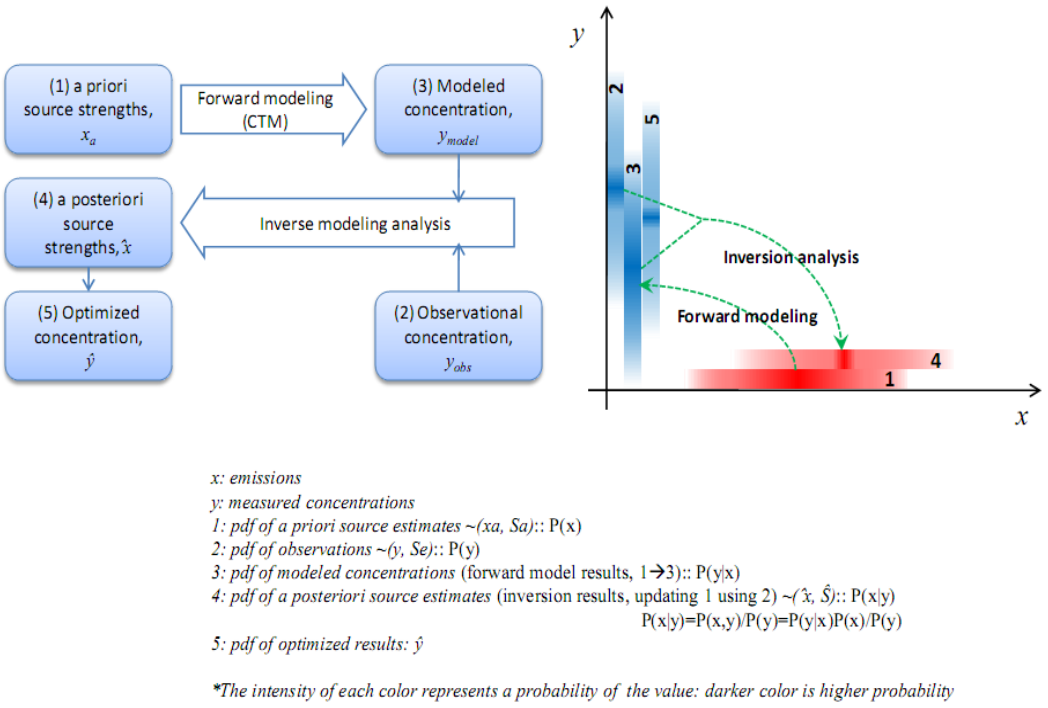

Figure 8.1 Illustrating the relationship between the prior source estimates, the measurements, and the posterior source estimate. The brightness of the color represents the probability distribution of each variable.

The maximum *a posteriori* (MAP) probability solution of the inverse

problem is finding an $\hat{x}$ ($\hat{x} = \int xP(x \mid y)dx$) where the posteriori probability distribution $P(x \mid y)$ (the conditional pdf of x given y) is a maximum, i.e.,

$$\hat{\mathbf{x}} = \mathbf{x_a} + (\mathbf{K^T S_e^{-1} K} + \mathbf{S_a^{-1}})^{-1} \mathbf{K^T S_e^{-1}} (\mathbf{y} - \mathbf{K x_a}) \ . \qquad \text{(Eqn. 4.2)}$$

$\mathbf{x_a}$ denotes a matrix of a priori source strength estimates, $\mathbf{S_e}$ is the error covariance matrix of the model, $\mathbf{S_a}$ is the error covariance matrix of prior information and $\hat{\mathbf{x}}$ is a matrix of optimized source strengths. The covariance matrix of $\hat{\mathbf{x}}$ is expressed as:

$$\hat{\mathbf{S}} = (\mathbf{K^T S_e^{-1} K} + \mathbf{S_a^{-1}})^{-1}. \qquad \text{(Eqn. 4.3)}$$

This technique is also frequently called a Bayesian 'synthesis' inversion. During the inversion analysis procedure, a pre-specified source pattern ($\mathbf{x_a}$) is linearly combined in the calculations and contributes to synthesis of the optimized source strengths ($\hat{\mathbf{x}}$).

4.2 Assigning uncertainties in the analyses

Two error covariance matrices are involved in the inversion calculation using the Bayesian method. Properly specifying and assigning those uncertainty terms is a particularly important part of the analysis since both inversion results and the *a posteriori* error covariance matrix($\hat{\mathbf{s}}$) can be sensitive to the error covariance matrices [Enting, 2002; Palmer et al., 2003].

4.2.1 Uncertainties in measurements: Se

The total observations error (**Se)** is a diagonal covariance matrix comprised of the following uncertainties: measurement error, representation error and forward model error.

$$e_{observation} = \sqrt{e^2_{measurements} + e^2_{representation} + e^2_{forward\ model}} \qquad \text{(Eqn. 4.4)}$$

The measurement error is the sum of all factors affecting the accuracy of the measurement including instrumentation error and CO extraction system error. In [Brenninkmeijer, 1993], he estimated the maximum absolute uncertainty (m.a.u.) of CO concentration as 2% and of $\delta^{18}O$ as 1 ‰. The same extraction system design for analyzing CO concentration and measuring isotopic ratios are used in this study. The errors of measurements presented here (1 σ) are calculated to be 1.3% and 0.27‰ respectively through the more than 300 calibration runs. Therefore, the m.a.u. of our data sets are also estimated as 2% for concentration since the standard deviation is similar to the [Brenninkmeijer, 1993] results. Since, for $\delta^{18}O$ measurements, the systematic error produced from the Schütze oxidant is dominant and is less than 1‰, the m.a.u. is estimated at 1‰ (Table 4.1) [Brenninkmeijer, 1993; Mak and Brenninkmeijer, 1994].

Table 4.1 Estimated and measured uncertainties in isotopic and concentration measurements

Quantity	Unit	uncertainty (1σ)		e.m.a.u*
		Brenninkmeijer 1993	This study	
CO	ppbv	1.70%	1.31%	2%
$\delta^{18}O$	‰, VSMOW	0.40 ‰	0.27 ‰	1 ‰

* e.m.a.u denotes estimated maximum absolute uncertainty, i.e., sum of systematic and random errors

To apply the errors to the Bayesian inversion approach, it is necessary to convert the [CO] and $\delta^{18}O$ error to the error of [$C^{16}O$] and [$C^{18}O$]. The error of [$C^{16}O$] is considered to be the same as that for [CO]. The $\delta^{18}O$ error is converted for [$C^{18}O$] error using both [$C^{16}O$] error and $\delta^{18}O$ error because, by the definition of the delta, $\delta^{18}O$ is the ratio of $C^{16}O$ to the $C^{18}O$. Thus, the total measurement error is propagated to 5.41%. Typically in CO inversion studies, the measurement error has been evaluated as less than 2% [Palmer et al., 2003; Arellano et al., 2004]. However, 5.5% for the measurement error was applied in here since the uncertainty of isotope ratio is commonly higher than the uncertainty of the concentration due to the trace amount of the minor isotopes.

Because, practically, there is no 'true' model to measure the uncertainties of the chemical transport model, errors in forward models are very difficult to quantify. Thus, sometimes the uncertainties of the forward model are neglected in the inversion analyses and the model is assumed to be perfect [Petron et al., 2002].

In this study, the errors related to the forward chemical transport model (representation error and forward model error) are considered. The errors are treated as described below.

Representation error is an aggregated error of the mismatch of spatial and temporal scale between the model and observation. Usually, for analyzing both concentration and isotopic ratios of carbon monoxide, air samples are collected for a couple of hours at a surface station while, in the model, the size of corresponding grid box is $2.8^{\circ} \times 2.8^{\circ}$ and the concentration is averaged for a day. Thus, uncertainties arise from the representativeness of the observation to the entire grid cell. Since the carbon monoxide monitoring sites used for this inversion analysis are located in remote locations, local sources minimally affect the CO concentration and isotopic ratios. Also, it is assumed that CO is well-mixed in the atmosphere on the scale of each model grid box because the average lifetime of CO is several months. Therefore, the contribution of spatial and temporal mismatch to the uncertainty analysis is considered to be minimal. In [Palmer et al., 2003], aircraft measurements in each model grid box were used to define the representation error. The variability of the direct measurements was approximately 5-10% in each $2^{\circ} \times 2.5^{\circ}$ grid. The representation error is analyzed by calculating the average of the variance of monthly modeled mixing ratios and monthly observations and 8% of the concentration is obtained from the simulation results [Bousquet et al., 1999a; Bousquet et al., 1999b; Kasibhatla et al., 2002].

Another uncertainty related to the model is forward modeling error. It comprises from errors that arise from inaccurate chemical reactions such as missing reactions, transport and model parameters such as reaction rate constants and the kinetic isotope effect. Error estimation is performed following [Palmer et al., 2003] which assumed the residual of the relative error i.e., the standard deviation of $(K_a-y)/y$ where K_a denotes modeled concentration and y is observed concentration, represents the uncertainties of chemical transport model. In this study the forward modeling error was calculated to be 8.5% of the concentration.

The observation error covariance matrix $\mathbf{S_e}$ is derived from the sum of the measurement error and representation error and forward chemical model error. The total observation error is approximately 13% with the uncertainty originating from the imperfect model is more than twice that of the measurement error. Considering unknown and unevaluated possible error factors, 15% is used in this study for the total observation error in the inversion analyses [Heimann and Kaminski, 1999; Pétron et al., 2002; Palmer et al., 2003; Arellano et al., 2004; Müller and Stavrakou, 2005; Chen and Prinn, 2006; Palmer et al., 2006].

4.2.2 Uncertainties in a priori source estimates: $\mathbf{S_a}$ (*a priori* source)

Assigning the proper uncertainty level of a priori source strength estimates

($\mathbf{S_a}$) is also as important as defining the observation error covariance matrix ($\mathbf{S_e}$). Sometimes $\mathbf{S_a}$ can significantly affect optimized source strength estimates and/or error analyses.

The bottom-up estimations of CO source strengths are still containing large error ranges as well as the top-down source estimations are widely ranged. Thus, the choice of uncertainties level of *a priori* source estimations is started from weakly constraining the sources which assign the largest possible values of each entry of the error covariance matrix. In Bian et al., 2007, the uncertainty of global annual emissions of biomass burning CO was estimated at 30% however they also indicated that the regional variations are often much higher (factor of 2 ~ 5). Duncan et al., 2007 showed a 25% uncertainty remains for fossil fuel CO despite rigorous and extensive bottom-up estimates. Also, the inconsistency of source estimates from the previous inversion analyses shown in Figure 1.1 indicates that the uncertainty of each source is at least 20% for anthropogenic, 50% for biomass burning, 100% for biogenic hydrocarbon oxidation, 15% for CH_4 oxidation [Bergamaschi et al., 2000a; Petron et al., 2002; Petron et al., 2004; Muller and Stavrakou, 2005; Kasibhatla et al., 2002; Arellano et al., 2004; Arellano et al., 2006]. In general, allowing more flexibility for the *a priori* source estimates is safe to initiate the inversion analyses, if there is not enough information about the accuracy of the source strength estimates. Previous studies also carefully started inversion analyses using weak constraints: 50% of *a priori*

source strength estimates [Palmer et al., 2003; Arellano et al., 2004; Heald et al., 2004; Arellano et al., 2006; Duncan et al., 2007]. In this study, to find the best estimate of the *a priori* source error covariance matrix ($\mathbf{S_a}$), a sensitivity test was performed to analyze the response of inverse modeling with varying Sa: 10%, 20%, 50%, 100% and 200%.

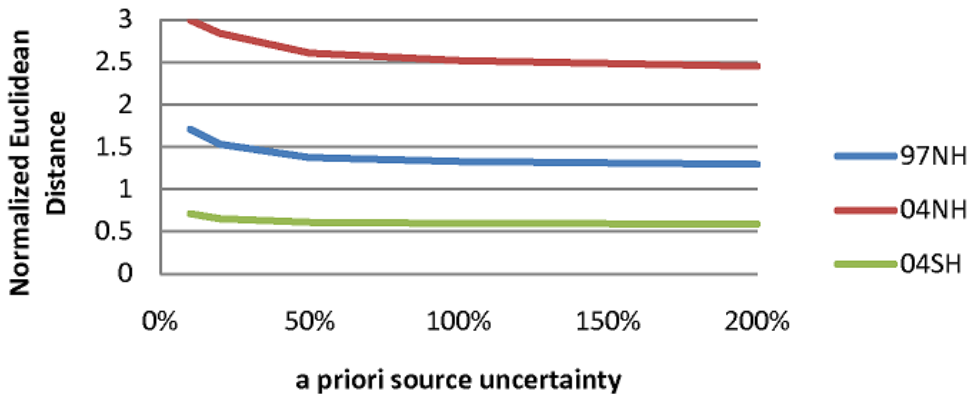

Figure 4.2 Averaged distance between the measurements and *a posteriori* CO concentrations

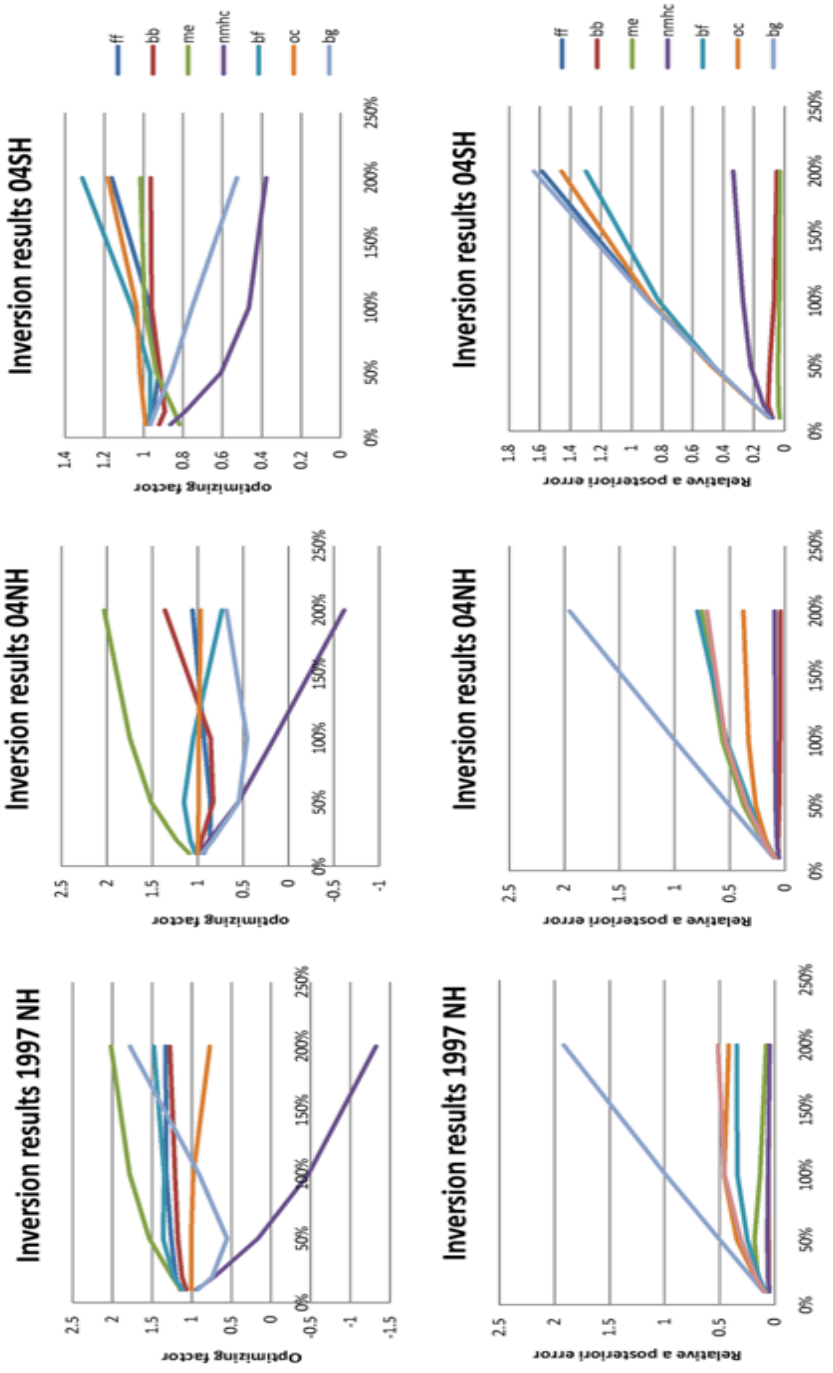

Figure 4.3 Inversion results of each source with different *a priori* source uncertainties

In Figure 4.2 and 4.3, the smaller optimized model-observation difference was found with higher *a priori* source uncertainties ($\mathbf{S_a}$) however, frequently, the inversions with larger uncertainties failed to constrain the sources. Not only *a posteriori* errors are increased after inversion for some cases but also unrealistically huge source changes or even negative sources are obtained. Assigning more than 100% of the uncertainties of each CO source tends to ignore the *a priori* information too much during the inversion process. Whereas giving a large confidence to the *a priori* source information such as 10% or 20% uncertainty, despite the known error of the *a priori* source estimates, the inversion processes are over-dependent to the *a priori* information and results in a small difference between before and after optimization. Optimization results are evaluated by the normalized Euclidean distance (E) expressed by:

$$E = \frac{1}{N}\sqrt{\sum_{i=1}^{N}(a_i - b_i)^2} \qquad \text{(Eqn. 4.5)}$$

where a is optimized concentrations, b is observed concentrations and *i* is an index of each data point. The distance between the measured concentration and the optimized concentration converged to a specific value after assigning higher than 50% of source uncertainties in all three cases (1997 NH, 2004 NH and 2004 SH); the inversion results are insensitive to larger than 50% error covariance matrices (Figure 4.2).

Hence 50% of the current source estimations are determined to be the

most proper uncertainty range, based on our sensitivity test results and prior investigations. Plus, instead of assigning same errors for the all sources, additional constraints were given to the methane oxidation source and fossil fuel source. Because atmospheric methane has a long lifetime (~10 years; [Lawrence et al., 2001; Horowitz et al., 2003; Emmons et al., 2010]), its reservoir is relatively well known and only 7% of its interannual variability was observed during the past two decades (from 1978 ~ 1998) [Dentener et al., 2003; IPCC 2001]. Moreover, in these model studies, the CH_4 oxidation source is directly scaled to the NOAA GMD surface measurements. Therefore, 10% is assigned for the *a priori* error of methane derived CO. For the fossil fuel source, many inversion studies have been updating the fossil fuel source inventory (Figure 1.1) and is, compared to the natural sources, relatively well known. Since *a posteriori* error of fossil fuel emission inventory in [Petron et al., 2004] was evaluated as 13% in global average and the variability of anthropogenic source strength estimates showed in Fig 1.1 was 18%, the uncertainties of fossil fuel source are estimated at 20% in this study. Thus, the *a priori* source estimation errors (S_a) are assumed diagonal matrix and set 10% for CH_4 oxidation source, 20% for fossil fuel source and 50% for all other sources unless S_a is noted.

4.3 Number of observations

Theoretically, in this study, the inversion system is always over-determined since there are more observations (N_y) than unknowns (N_x). Annual fluxes of seven CO sources (N_x= 7; fossil fuel, biofuel, biomass burning, CH_4 oxidation, NMHC oxidation, biogenic and ocean) are optimized with monthly averaged one year measurements of each station; 12 observations per station. Thus, the dimension of observation (N_x) is 12 x # of stations (2~4 stations) and so $N_x < N_y$. Plus, the N_x is doubled since isotope measurements are also included in the inversion analyses. Therefore, despite using the observations from only 2 ~ 4 stations in each hemisphere, the inversion system is free from the ill-conditioned problem [Pétron et al., 2002].

4.4 Inversion schemes; incorporation of isotopic ratio measurements to the source optimization

Since certain CO sources have unique isotopic source signatures, isotopes provide additional information about the sources. Thus, coupling the concentration and isotope information should improve the inverse modeling results and reduce the uncertainties of the flux estimates [Criss, 1999; Enting, 2002].

Because of the difficulties of measuring isotopes and requirements of additional efforts for isotope modeling, there has been only one previous study

implemented with isotope information for the top-down estimation of CO source strengths [Bergamaschi et al., 2000a]. Moreover, only limited numbers of inverse modeling analyses for other species incorporate both isotopic ratio data and concentration data for optimizing global budgets [Hein et al., 1997b; Bergamaschi et al., 2000a; Miller et al., 2002; Mikaloff Fletcher et al., 2004; Bousquet et al., 2006; Rayner et al., 2008a; Lassey et al., 2000].

In spite of the benefit of including isotope information on inversion analyses, inversion schemes applied in previous studies have not been fully utilized because of following problems:

1) Correlated concentration and isotopic ratio in the inversion process.

For example, in [Mikaloff Fletcher et al., 2004], the following equation is used for an additional constraint of the methane source.

$$\delta_j^{obs} y_j^{obs} - \delta_j^{model} y_j^{model} = \sum_{i=1}^{n\ of\ src} H_{i,j} x_i \delta_i^{source} \qquad \text{(Eqn. 4.6)}$$

where y^{model} is the modeled and y^{obs} is the observed concentration at station j, x_i is the source strength for the source i, δ and δ^{obs} are modeled and measured isotope ratio respectively, $\delta^{src}{}_i$ is isotopic source signature of source I and H_i is the basis function which describes the signal described at the station after one time step in response to an arbitrary, steady source from the source i. In this formulation, the source strength is expressed as a combination of the mixing ratio and the isotopic ratio terms. Thus, the isotope information did not constrain the sources

independently. In other previous isotope inversion studies, to relate source strengths and isotopic ratios, they introduced assumptions. Because it sometimes fails to work for some species having strong seasonal or interannual variability of isotope ratios [Hein et al., 1997a] and errors raised from the assumption are propagated in the inversion system, the benefit of adding isotope information will be diminished [Hein et al., 1997a; Manning et al., 1997; Enting, 2002].

2) Introduced isotope information as a supplementary constraint.

In both [Bergamaschi et al., 2000a; Rayner et al., 2008b], the inversion results are dominantly controlled by the mixing ratios, in spite of including isotope measurements in the inversion analysis, since the number of sampling stations for concentration measurement is more than six times the number of CO isotope sampling stations.

3) Improper weighting assignments for the concentration and isotopic ratio data.

Since the unit of concentration and isotopic ratio is different (for carbon monoxide, ppbv and per mil for concentration and δ, respectively), the meaning of unity for the model-observation difference is different for concentration and isotope ratio. The impact of the different units should be correctly accounted in the inversion [Pilkington, 2006b]. Previous studies [Hein et al., 1997a; Bergamaschi et al., 2000a; Rayner et al., 2008b] have solved the inverse problems through minimizing the model-observation difference without consideration of

balancing the two properties (concentration and isotope ratio) which implies the role of isotopes in the prior inversion analyses have not been fully utilized to constrain the sources.

Furthermore, for carbon monoxide, in contrast to carbon dioxide or methane, its lifetime is short and, therefore, its temporal variation is relatively large. This is especially important for $C^{18}O$. For instance, in the Northern Hemisphere mid-latitude, the typical inter-seasonal variation of $\delta^{13}CO_2$ is 0.4 per mil, $\delta^{13}CH_4$ is 0.5 per mil, $\delta^{13}CO$ is 5 per mil and $\delta C^{18}O$ is 8 per mil [Miller et al., 2002; GLOBALVIEW-CH_4 [National Oceanic and Atmospheric Administration (NOAA), 2001]; Mak and Kra, 1999; Mak et al., 2003; This study]. Thus, if the long-lived species' isotope inverting methodologies are analogously applied to the CO isotope inversion, nonlinearity problems develop and can affect the inversion results [Hein et al., 1997a].

In this study, a two stage isotope inversion scheme is devised that is able to avoid the shortcomings of the previous methods as well as more effectively constrain the sources of atmospheric CO. In CO source optimization, instead of approaching concentrations and δ values, they are decomposed to $[C^{16}O]$ and $[C^{18}O]$ and used to optimize the sources. This technique enabled us to obviate two issues; nonlinearity of the relation between source strength and isotope ratio and weighting problem for balancing the significance of concentration and isotopic ratio.

4.4.1 Decoupled inversion

Since $C^{16}O$ and $C^{18}O$ are assumed to be uncorrelated, the sources of $C^{16}O$ and $C^{18}O$ can be individually optimized by using each [$C^{16}O$] and [$C^{18}O$] information:

$$\begin{aligned} {}^{16O}\hat{\mathbf{x}} &= {}^{16O}\mathbf{x}_a + ({}^{16O}\mathbf{K}^T\mathbf{S}_e^{-1}\,{}^{16O}\mathbf{K} + \mathbf{S}_a^{-1})^{-1}\,{}^{16O}\mathbf{K}^T\mathbf{S}_e^{-1}({}^{16O}\mathbf{y} - {}^{16O}\mathbf{K}\,{}^{16O}\mathbf{x}_a) \\ {}^{18O}\hat{\mathbf{x}} &= {}^{18O}\mathbf{x}_a + ({}^{18O}\mathbf{K}^T\mathbf{S}_e^{-1}\,{}^{18O}\mathbf{K} + \mathbf{S}_a^{-1})^{-1}\,{}^{18O}\mathbf{K}^T\mathbf{S}_e^{-1}({}^{18O}\mathbf{y} - {}^{18O}\mathbf{K}\,{}^{18O}\mathbf{x}_a) \end{aligned} \quad \text{(Eqn 4.7)}$$

where, ^{16}O and ^{18}O indicate the $C^{16}O$ and $C^{18}O$ data sets.

Therefore, while the formulation of the decoupled inversion is the same as the concentration-only Bayesian synthesis inversion method, the two independent inversion results allow for the estimation of both *a posteriori* $C^{16}O$ and $C^{18}O$ source strengths. Also, the ratio of ${}^{16O}\hat{\mathbf{x}}$ to ${}^{18O}\hat{\mathbf{x}}$ provides *a posteriori* $\delta^{18}O$ signature of the CO sources (Eqn. 3.4).

4.4.2 Coupled (simultaneous) inversion

Two different joint inversion approaches that incorporate concentration and isotopic ratio data sets were tested in this study. One is a simultaneous inversion technique; the concentration and isotope information constrain the sources in one inversion process. The other is a sequential inversion technique; each of the measured properties constrains the sources in two consecutive

inversion processes. (Figure 4.5)

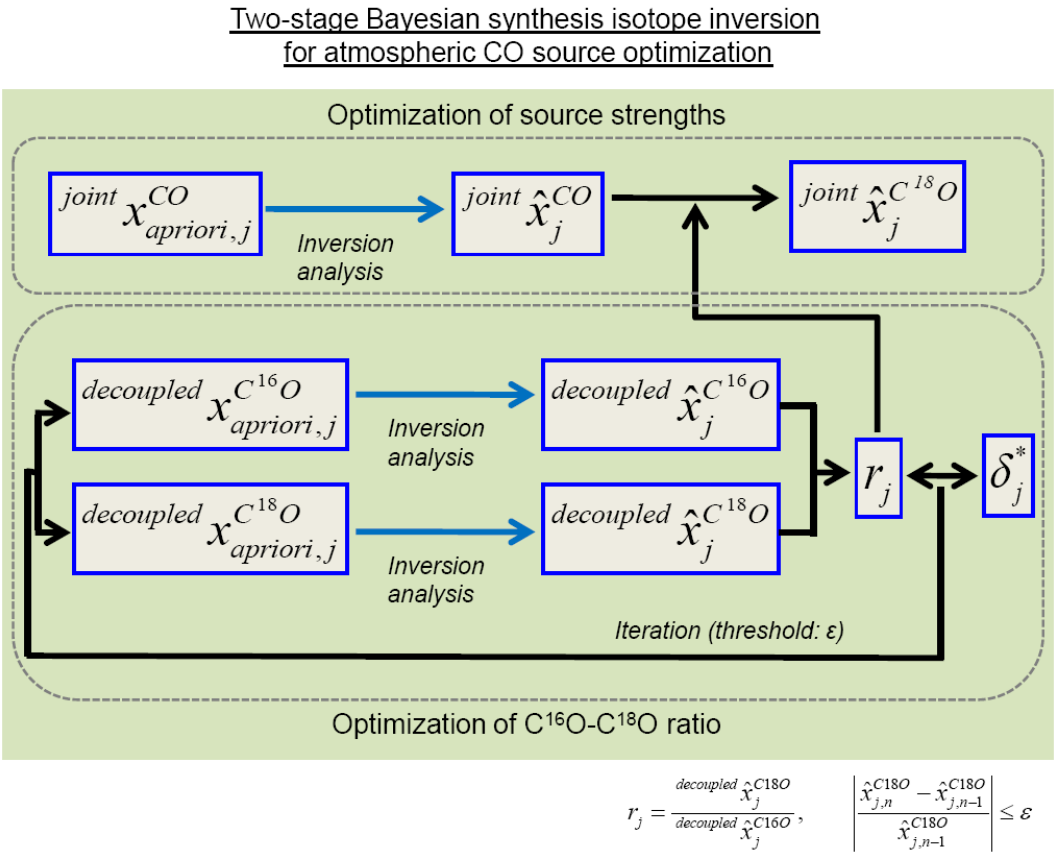

Figure 4.4 Schematic diagram for the two-stage Bayesian synthesis isotope inversion for atmospheric carbon monoxide

In the simultaneous inversion, both modeled and observed concentration and isotopic ratio are coupled in the solution matrices for the inverse problem:

$$\hat{\mathbf{x}} = \mathbf{x_a} + \left(\begin{bmatrix} {}^{16O}\mathbf{K} \\ {}^{18O}\mathbf{K} \end{bmatrix}^{\mathbf{T}} \mathbf{S_e^{-1}} \begin{bmatrix} {}^{16O}\mathbf{K} \\ {}^{18O}\mathbf{K} \end{bmatrix} + \mathbf{S_a^{-1}} \right) \begin{bmatrix} {}^{16O}\mathbf{K} \\ {}^{18O}\mathbf{K} \end{bmatrix}^{\mathbf{T}} \mathbf{S_e^{-1}} \left(\begin{bmatrix} {}^{16O}\mathbf{y} \\ {}^{18O}\mathbf{y} \end{bmatrix} - \begin{bmatrix} {}^{16O}\mathbf{K}\,{}^{16O}\mathbf{x_a} \\ {}^{18O}\mathbf{K}\,{}^{18O}\mathbf{x_a} \end{bmatrix} \right) \quad \text{(Eqn 4.8)}$$

Since the two independent measurement data sets (major and minor

isotopes; $C^{16}O$ and $C^{18}O$) are used to optimize the sources at the same time, the isotope information plays like an additional observational data set in the inversion system and, in comparison with the [CO]-only inversion, this renders more robust inverse modeling results.

Schematic diagram for simultaneous and sequential isotope inversion

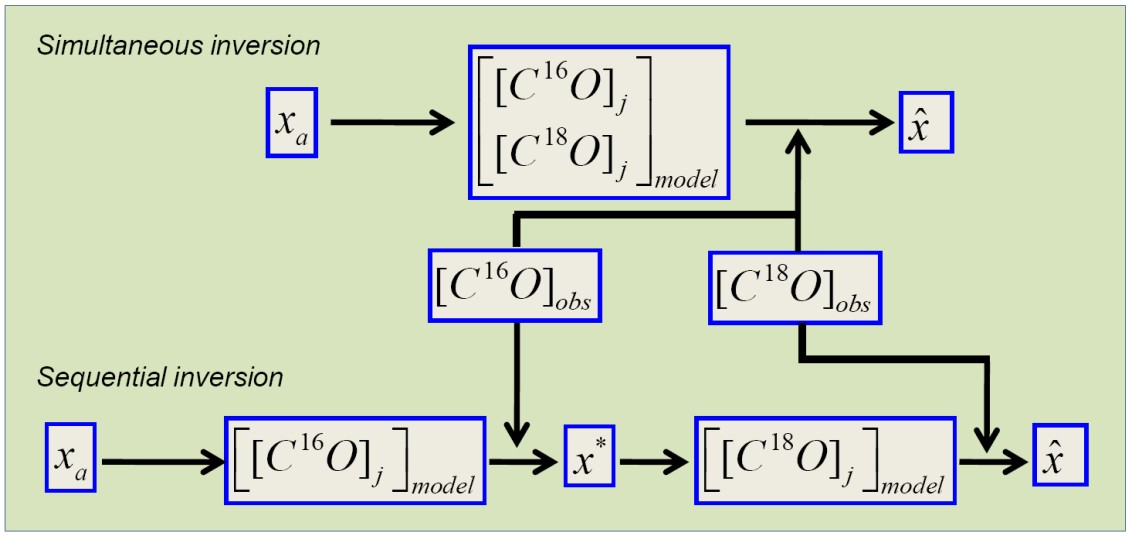

Figure 4.5 Schematic diagram showing the procedure of isotope information incorporation in simultaneous and sequential isotope inversion analysis

4.4.3 Sequential inversion

When simultaneously inverting different data sets that have a large difference in their magnitude (e.g., $[C^{16}O]$ and $[C^{18}O]$), a weighting issue is raised because the inversion results are dominantly constrained by the larger magnitude

measurement data. Proper weighting needs to be considered in the inversion. One of the methods to balance the contribution of two data sets is sequential use of observations, where the solution inverts one measurement data set first and the result provides the input for the inversion of the second observational information [Lines et al., 1988; Pilkington, 2006a]. In general, however, this method requires more effort in programming and requires more computing time because it has to invert for each data set.

In this study, the sequential use of concentration and isotope information is formulated as follows:

$$\begin{aligned} &\text{step 1}: \quad \mathbf{x}^{*} = \mathbf{x}_a + \left({}^{16O}\mathbf{K}^{T}\mathbf{S}_e^{-1}\,{}^{16O}\mathbf{K} + \mathbf{S}_a^{-1}\right)^{-1}\,{}^{16O}\mathbf{K}^{T}\mathbf{S}_e^{-1}\left({}^{16O}\mathbf{y} - {}^{16O}\mathbf{K}\mathbf{x}_a\right) \\ &\text{step 2}: \quad \hat{\mathbf{x}} = \mathbf{x}^{*} + \left({}^{18O}\mathbf{K}^{T}\mathbf{S}_e^{-1}\,{}^{18O}\mathbf{K} + \mathbf{S}_a^{-1}\right)^{-1}\,{}^{18O}\mathbf{K}^{T}\mathbf{S}_e^{-1}\left({}^{18O}\mathbf{y} - {}^{18O}\mathbf{K}\mathbf{x}^{*}\right) \end{aligned} \qquad \text{(Eqn. 4.9)}$$

where $\mathbf{x}^{*}$ is an intermediate estimated source strength vector that is acquired from the first step of the inversion process.

The joint inversion results of simultaneous use of concentration and isotope ratio and sequential use of them are compared in this study. The detailed result of the comparison is discussed in chapter 6.4 and here it is briefly described. Estimated *a posteriori* source uncertainties from the sequential inversion tend to be slightly smaller than errors from the simultaneous inversion. However, the optimized *a posteriori* source correction factors from the two inversion schemes are very close to each other. Thus this implies the importance of isotope ratios and concentrations are well-balanced in the simultaneous joint inversion method. This

suggests that simultaneous CO inversion scheme also constrains the sources effectively. Furthermore, similar results of sequential inversion (without using iteration) and simultaneous inversion imply that the linearity assumption for both $C^{16}O$ and $C^{18}O$ are correct.

4.4.4 Optimization of atmospheric CO source strengths and $\delta^{18}O$ of the sources

Estimating the fluxes of each carbon monoxide source by jointly inverting [$C^{16}O$] and [$C^{18}O$] is the primary purpose of this study. In addition to this, $C^{18}O$ source strength estimates are derived from the optimized CO source strengths and *a posteriori* isotopic ratio (r_j) of each source obtained from the decoupled inversion run (Figure 4.4). Although the same prescribed isotopic source signatures can be applied to calculate *a posteriori* isotope ratios, *Bergamaschi 2000b* showed that applying *a posteriori* carbon isotopic source signature, instead of using fixed isotopic source signature, provides more robust inversion results as well as our comparison of the inversion results with fixed and updated oxygen isotopic source signature confirmed their result for the oxygen isotopic source signatures (chapter 6). Thus, the $\delta^{18}O$ source signature optimization process is implemented in the joint inversion system in lieu of assuming fixed isotopic ratio of the sources. Optimized $\delta^{18}O$ source signatures calculated from the *a posteriori*

CO and $C^{18}O$ source strengths provides an additional benefit of including isotopic signature in inverse modeling. It allows for the verification of the joint inversion results by showing the fit of the optimized $\delta^{18}O$ values to the observations, while the [CO]-only inversions can confirm the results by comparing measurements with *a posteriori* CO concentrations only.

To optimize the isotopic source signature, the $C^{16}O$-$C^{18}O$ ratio is iteratively optimized from the decoupled run since it has been known that isotope ratio is a nonlinear function of the source strengths [Bergamaschi et al., 2000a]. Therefore, an iterative method that updates the Jacobian matrix (**K,** Eqn. 4.1) in each iteration was used to solve the inverse problem (Figure 4.4). Iterations were performed for each source and continued until the solution reaches a convergence;

$$\left| \frac{\hat{x}_{j,n}^{C18O} - \hat{x}_{j,n-1}^{C18O}}{\hat{x}_{j,n-1}^{C18O}} \right| \leq \varepsilon \,. \qquad \text{(Eqn. 4.10)}$$

During the iterations, the isotopic ratios were allowed to vary within a certain range (ε). The threshold is assigned differently for each source by current understanding level of the isotopic source signature. For fossil fuel source, 2‰ is assigned for the threshold since the previous estimates of the isotope signatures are reported in between 22‰ and 24‰ [Stevens et al., 1972; Brenninkmeijer, 1993; Stevens and Wagner, 1989; Brenninkmeijer and Rockmann, 1997] and the direct measurements on the exhaust from individual automobile running normally indicate the variations of $\delta^{18}O$ of CO as ±1.0‰ [Tsunogai et al., 2003]. The

previous global estimation of $\delta^{18}O$ from the biomass burning was 16.3‰ and 18‰ (1.7‰ difference) [Brenninkmeijer, 1993; Stevensens et al., 1972] and the uncertainties reported for biomass burning source signature were ±1‰ [Stevens and Wagner, 1989; Bergamaschi et al., 1998]. However, 5‰ is allocated for the threshold of biomass burning source because Kato et al., 1999 indicated that very wide range (3‰ ~ 26‰) of $\delta^{18}O$ from their chamber experiment. For the ε of the other sources, since there is one number reported for $\delta^{18}O$ of the sources, ±5‰ is estimated for ε, analogous to that for the biomass burning source that has a large variability of source signature.

The role of isotope information is expanded in the inverse modeling analysis with the optimized source signatures. This enables the separation of the *a posteriori* source estimates to the inventories of major and minor isotopes while the joint inversion gives updated information of the CO source strengths.

4.4.5 Optimization of modeled concentration and $\delta^{18}O$

Since observed concentrations are expressed as (Eqn. 4.1), the relationship between the measured and optimized modeled concentrations can be expressed as:

$$\hat{y} = \mathbf{K}\hat{x} + \hat{e} \qquad \text{(Eqn. 4.11)}$$

where $\mathbf{K}\hat{x}$ represent the optimized concentrations ($\hat{y}$) and $\hat{e}$ is *a posteriori* error matrix.

Updating the modeled isotopic ratios with the optimized source information is more complicated because isotope ratio (δ) is the 'relative' abundances of the two isotopologues. The implementation of the *a posteriori* isotopic source signatures to the optimization of modeled [$C^{16}O$] and [$C^{18}O$] is shown in below.

modeled concentration of isotopologues are expressed as :

$$a = \sum_j K_{a,j} x_{a,j}, \quad b = \sum_j K_{b,j} x_{b,j}$$

where *i* is an index for major and minor isotope (a : major isotope, b : minor isotope) and *j* is an index for the sources. We assume two sources for simplification.
The abundance of major and minor isotope can be linearly related by using isotopic source ratio (γ_j).

$$x_{a,j} = \gamma_j x_{b,j}$$

The concentration of a and b can be rewritten in a matrix form :

$$\begin{pmatrix} \mathbf{a} \\ \mathbf{b} \end{pmatrix} = \begin{pmatrix} \mathbf{K_{a,1}} & \mathbf{K_{a,2}} \\ \mathbf{K_{b,1}}/\boldsymbol{\gamma_1} & \mathbf{K_{b,2}}/\boldsymbol{\gamma_2} \end{pmatrix} \begin{pmatrix} \mathbf{x_{a,1}} \\ \mathbf{x_{a,2}} \end{pmatrix} = \begin{pmatrix} \mathbf{K_{a,1}x_{a,1}} & \mathbf{K_{a,2}x_{a,2}} \\ \mathbf{K_{b,1}x_{a,1}}/\boldsymbol{\gamma_1} & \mathbf{K_{b,2}x_{a,2}}/\boldsymbol{\gamma_2} \end{pmatrix} \begin{pmatrix} \mathbf{f_1} \\ \mathbf{f_2} \end{pmatrix}$$

a unit source strength factor : $f_1 = f_2 = 1$

$$= \begin{pmatrix} \mathbf{a_1^*} & \mathbf{a_2^*} \\ \mathbf{b_1^*} & \mathbf{b_2^*} \end{pmatrix} \begin{pmatrix} \mathbf{f_1} \\ \mathbf{f_2} \end{pmatrix}$$

where a_1^*, a_2^*, b_1^*, and b_2^* represent the modeled concentration.

The optimized f_j can be obtained by the inversion analysis.

let *a posteriori* $f_j = \hat{f}_j$ and *a posteriori a* can be expressed as

$$\hat{a} = \sum_j K_{a,j} \hat{x}_{a,j} = \sum_j K_{a,j} x_{a,j} \hat{f}_j$$

a posteriori linear relation between the major and the minor isotope is :

$$\hat{x}_{a,j} = \gamma^*_j \hat{x}_{b,j}$$

also using updated isotopic source ratio (γ^*_j), *a posteriori b* is expressed as a function of *a priori* modeled concentration ($K_{b,j} x_{b,j}$).

$$\hat{b} = \sum_j K_{b,j} \hat{x}_{b,j} = \sum_j K_{b,j} \frac{\hat{x}_{a,j}}{\gamma^*_j} = \sum_j K_{b,j} \frac{x_{a,j} \hat{f}_j}{\gamma^*_j} = \sum_j K_{b,j} \frac{\gamma_j x_{b,j} \hat{f}_j}{\gamma^*_j}$$

and this gives :

$$\hat{b} = \sum_j \frac{\gamma_j}{\gamma^*_j} K_{b,j} x_{b,j} \hat{f}_j$$

for fixed isotopic source signatures $\frac{\gamma_j}{\gamma^*_j} = 1$

If isotopic source signatures are well defined, $\gamma_j/\gamma_j{}^*$ should be close to 1 and no further treatment for updating *a posteriori* source signature information is necessary. For the oxygen isotopes of CO, in comparison with the fixed isotopic source ratios (chapter 6), *a posteriori* $\delta^{18}O$ is closer to the observation with the updated isotopic source information. This implies the joint inversion analysis provides more useful results if a posteriori source information is applied along with the optimized source strengths when isotopic source signatures contain large error.

5. Simulated Atmospheric [CO] and $\delta^{18}O$

5.1 Model evaluation

In a chemical transport model (CTM), the accuracy of a forward model result is crucial for producing both reliable source strength estimates and analyses of the modeled results. For the inversion analysis, because it relies on the assumption that the physical-chemical connection between the parameters (e.g., source strengths and reaction constants) and the observed properties (e.g., concentration and isotopic ratio) are known, if the CTM does not simulate the real measurement accurately, its source estimates would be worthless even though all of the mathematical assumptions are correct. The performance of CTMs is commonly validated by comparing model output with direct measurements. To get more confidence in our forward modeling results, NOAA (National Oceanic and Atmospheric Administration) GMD (Global Monitoring division) CO concentration ground measurements are included in the model evaluation. Precision of their measurements is <2%. [Novelli et al., 1992; Novelli et al., 1998; Novelli et al., 2003]. Since Mauna Loa (altitude: 3397m) and Izaña (altitude: 2360m) are located above the inversion layer, they represent free tropospheric air which is not directly affected by surface emissions. Due to the influence of surface emissions and short lifetime of CO the additional model-observation bias

can be observed from the other stations because they are normally located within the planetary boundary layer,

Three different measures are used here to assess the model performance: chi-square (goodness of fit) test, model-observation difference and correlation. Usually the 'correlation' represents dissimilarity of the trend or patterns between the modeled property and measured property and the 'distance' shows the offset between the model and measurements. If a model accurately reproduces observational data the distance (d) will be close to '0' and correlation ($\rho_{x,y}$) will be close to '1'. The 'correlation' and the 'distance' are expressed as:

Model - observation difference :

$$\boldsymbol{d} = \frac{1}{\boldsymbol{N}} \sum_{\boldsymbol{i}}^{\boldsymbol{N}} | \boldsymbol{x_i} - \boldsymbol{y_i} |$$

(Eqn. 5.1)

Correlation coefficient :

$$\rho_{x,y} = \frac{\frac{1}{\boldsymbol{N}} \sum_{\boldsymbol{i}=1}^{\boldsymbol{N}} (\boldsymbol{x_i} - \mu_x)(\boldsymbol{y_i} - \mu_y)}{\sqrt{\frac{1}{\boldsymbol{N}} \sum_{\boldsymbol{i}=1}^{\boldsymbol{N}} (\boldsymbol{x_i} - \mu_x)^2} \sqrt{\frac{1}{\boldsymbol{N}} \sum_{\boldsymbol{i}=1}^{\boldsymbol{N}} (\boldsymbol{y_i} - \mu_y)^2}}$$

where, x_i is modeled concentration or isotopic ratios at station i and y_i is concentration or isotope ratio. Due to the limited availability of the measurements (weekly or bi-weekly sample), we used monthly averaged modeled and observational data to assess the reproducibility of model. The results of the evaluation at each station are shown in Table 5.1.

Table 5.1 Model-observation difference, correlation and chi-square of each station

Station	Latitude	Difference		Correlation		Chi-square	
		[CO]	$\delta^{18}O$	[CO]	$\delta^{18}O$	[CO]	$\delta^{18}O$
Alert	82° 27' N	14.973	1.034	0.933	0.978	0.391	0.129
Spitzbergen	78° 54' N	12.220	0.986	0.917	0.961	0.226	0.123
Iceland	63° 15' N	9.028	1.929	0.926	0.929	0.171	0.709
Izaña	28° 18' N	13.555	1.321	0.921	0.928	0.561	0.364
Mauna Loa	19° 32' N	12.017	4.832	0.694	0.656	0.730	5.109
Barbados	13° 10' N	18.140	4.621	0.721	0.704	1.655	4.576
Baring Head	41° 18' S	6.400	3.253	0.789	0.555	0.831	5.299
Scott Base	77° 51' S	6.195	2.491	0.843	0.728	0.606	1.976

The goodness of fit of a model describes how well the simulated result fits the measured data set. A statistical measure chi-square is used to determine the performance of the model and it is defined by

chi - square and reduced chi - square :

$$\chi^2 = \sum_{i}^{N} \frac{(x_i - y_i)^2}{\sigma_{y,i}^2}, \qquad \chi_{red}^2 = \frac{\chi^2}{\nu} \qquad \text{(Eqn. 5.2)}$$

The reduced chi-square (χ_{red}^2) is a quantity that a chi-square divided by the number of degrees of freedom (ν) and this estimates the ratio of the variance of modeled data set to the variance of measured data set. In this test, ν is equal to the number of observations. If χ_{red}^2 is close to 1 this indicates the observed data is well explained by the model and if it is much larger than 1 it means the model did

not fully capture the observational data set. A χ_{red}^2 much less than 1 or close to zero indicates that the model is improperly fitting the noise or the uncertainty of the observations are over estimated (over-fitting data).

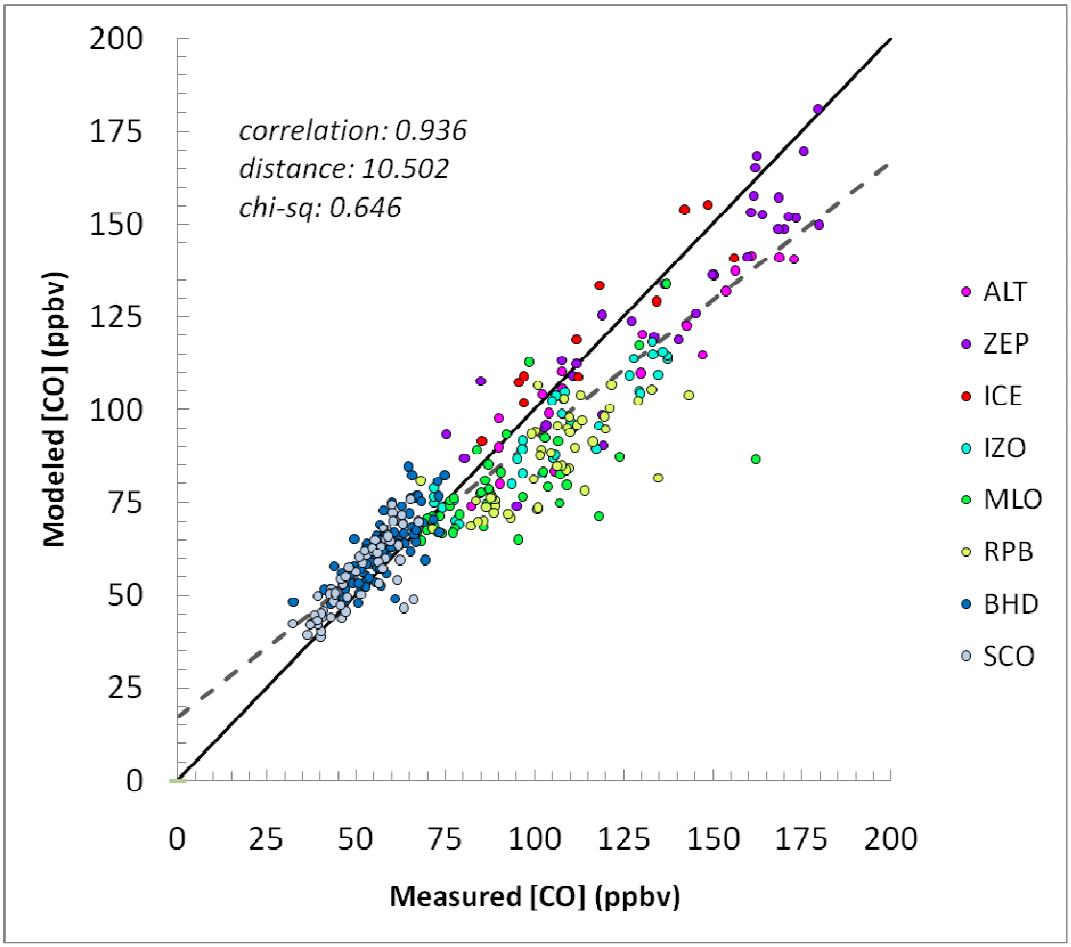

Figure 5.1 A scatter plot of measured versus modeled concentration of CO. The solid line depicts 1:1 correspondence and the dashed line is regression line of all measurements.

In this study, the model simulated the observations fairly well in both

concentration and isotope ratio. For all stations, the modeled and measured concentration showed a strong correlation (ρ = 0.94) and the mean model-observation difference was 10.5ppbv. This implies the model captures the seasonal and interannual variation of the [CO] sufficiently while the model did not fully reproduce the absolute values of the measurement. Figure 5.1 and Figure 5.3 shows Southern Hemispheric CO concentrations are slightly over estimated by the model (SCO: 6.2 ppbv, BHD: 6.4 ppbv). This possibly resulted from the underestimation of [OH] or overestimation of some sources. However, if [OH] is increased, the modeled $\delta^{18}O$ will be more depleted and further removed from the 1:1 correlation line (Figure 5.2). Hence, to fit both $\delta^{18}O$ and [CO], it is required to reduce sources having a negative $\delta^{18}O$ signature (NMHC and CH_4 oxidation source).

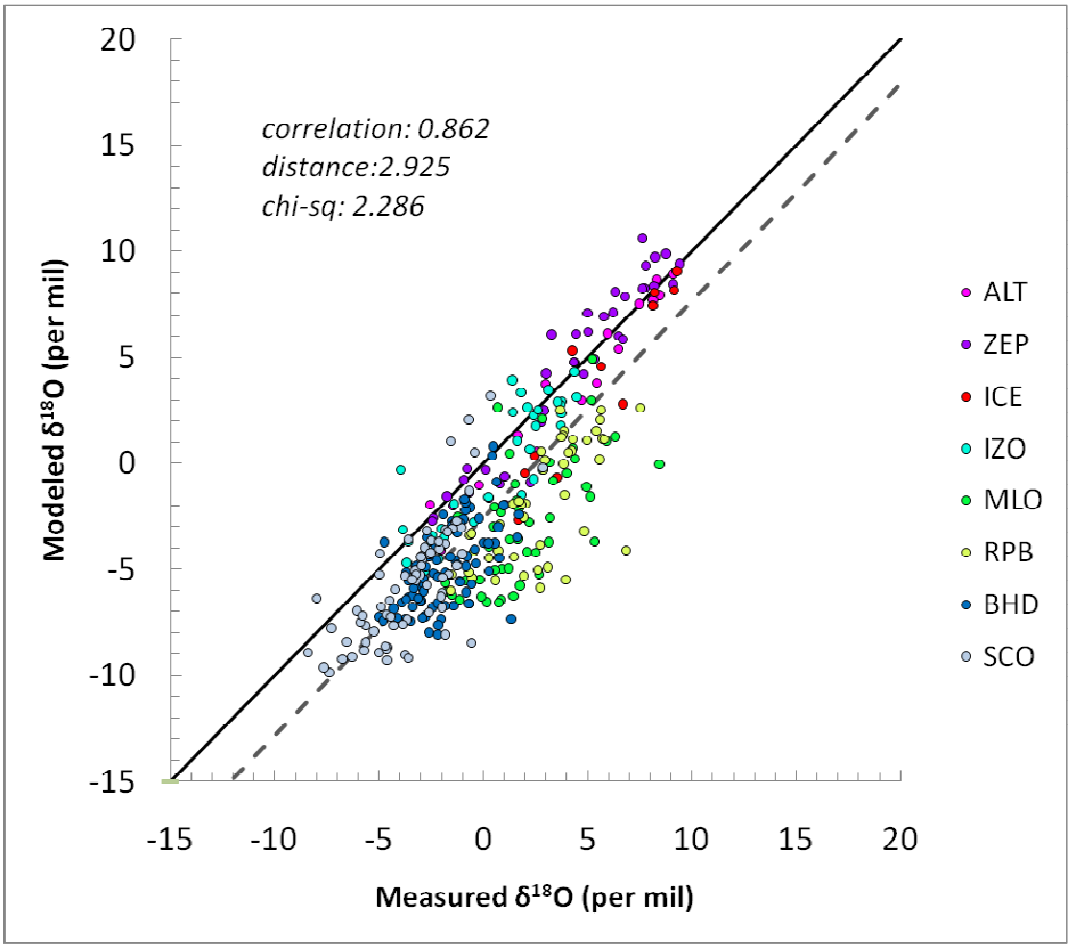

Figure 5.2 A scatter plot of measured versus modeled $\delta^{18}O$ of CO. The solid line depicts 1:1 correspondence and the dashed line is regression line of all measurements.

Since the NMHC oxidation source has a strong seasonality (Appendix A), even if the source strengths are decreased, it cannot explain the year-round overestimate of [CO]. In Manning et al., 1997, they estimated CO yield from the CH_4 oxidation is less than 0.7 based on $\delta^{13}C$ measurements while 1 is used for the yield in this study which is also assumed in [Duncan et al., 2007]. Detailed

discussion about the CO yield from the CH_4 oxidation is discussed in chapter 5.2.1. This suggests the presented CH_4 oxidation source might be overestimated in the Southern Hemisphere. In the Northern Hemisphere, especially during the winter, modeled concentrations are generally lower than measured concentrations (Figure 5.1 and Figure 5.3). For $\delta^{18}O$, the model accurately reproduced observations at high latitude stations (ICE, ZEP, ALT) while modeled $\delta^{18}O$ was lighter than observations at mid- and low latitude stations. In high latitudes, the dominant sources (fossil fuel and biofuel combustion) have isotopic signatures that are similar to the average signature, thus, the influence of their inaccurate strengths is small, particularly during winter. For example, the wintertime oxygen isotope ratio of biofuel in high latitude is approximately 12‰ (Appendix A) and total $\delta^{18}O$ is approximately 8‰ (Figure 5.3), it is the most probable major source that minimally affects $\delta^{18}O$ simulation result and improves the concentration fitting if the source inventory is increased. In the mid- and low latitude NH, underestimations of both [CO] and $\delta^{18}O$ informed that the ^{18}O enriched sources (fossil fuel, biofuel and biomass burning) are underestimated.

The χ_{red}^2 of the forward model run for CO concentration was 0.65 and of $\delta^{18}O$ was 2.29. This is comparable to the results from [Bergamaschi et al., 2000b] and [Bergamaschi et al., 2000a]. Depending on emission scenario, $\chi_{red}^2 = 1.9 \sim 2.5$ were estimated for CO concentration and $\chi_{red}^2 = 0.4 \sim 0.9$ were estimated for $\delta^{18}O$ with optimized a posteriori emissions. Thus, a more accurate top-down global CO

source estimate was achieved here. In general, the modeled $\delta^{18}O$ shows good agreement measurements, however, the simulation results of CO concentration were even more reliable; $\rho_{[CO]}$=0.94 > $\rho_{\delta 18O}$ =0.86 and $\chi_{red}^{2}{}_{[CO]}$=0.65 < $\chi_{red}^{2}{}_{\delta 18O}$=2.29. This supports the discrepancies of global CO source distributions of previous studies shown in Figure 1.1; the current estimation of total CO emission is relatively close to reality, whereas the strength of each source is less certain. Also, the $\delta^{18}O$ signatures of natural sources such and biomass burning and NMHC oxidation source have more variability and uncertainty and this might have added an additional error in the $C^{18}O$ simulation (Table 1.2).

Figure 9.3 MOZART-4 simulation results; The gray dots are modeled [CO] and $\delta^{18}O$, the green dots are NOAA [CO] and the blue dots are [CO] and $\delta^{18}O$ used in this study.

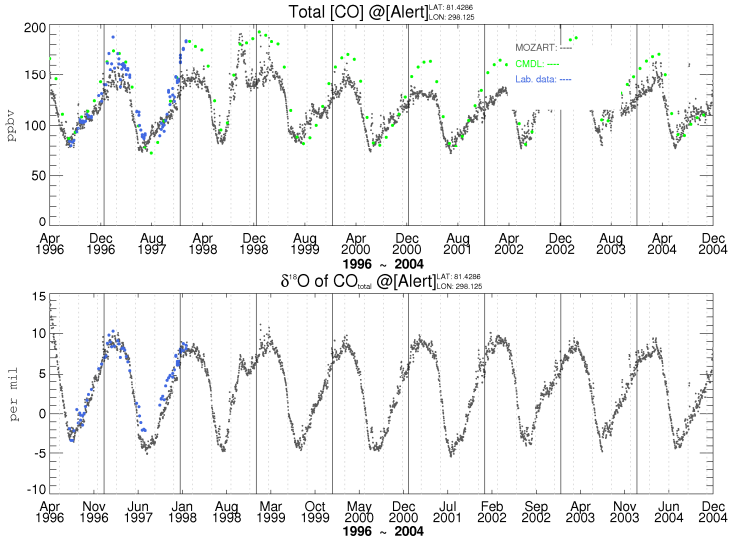

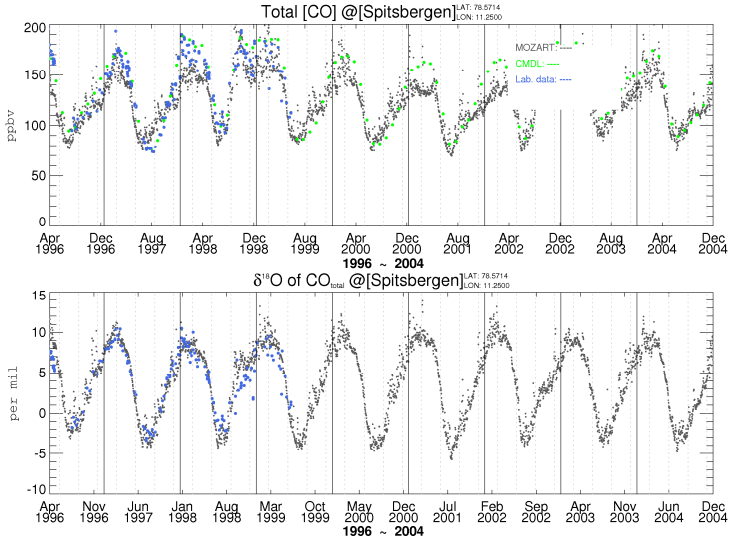
Total [CO] @[Spitsbergen]
LAT: 78.5714
LON: 11.2500
MOZART: ----
CMDL: ----
Lab. data: ----
ppbv
1996 ~ 2004
δ18O of COtotal @[Spitsbergen]
per mil

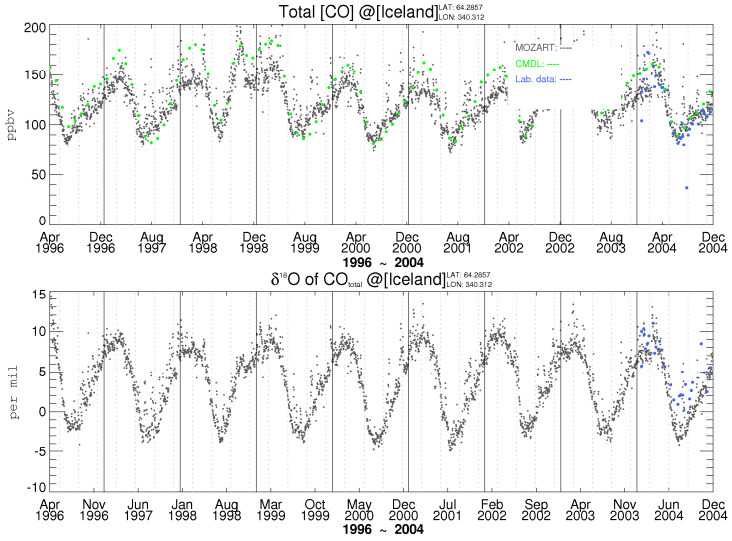
Total [CO] @[Iceland]
LAT: 64.2857
LON: 340.312
MOZART: ----
CMDL: ----
Lab. data: ----
ppbv
1996 ~ 2004
δ18O of COtotal @[Iceland]
per mil

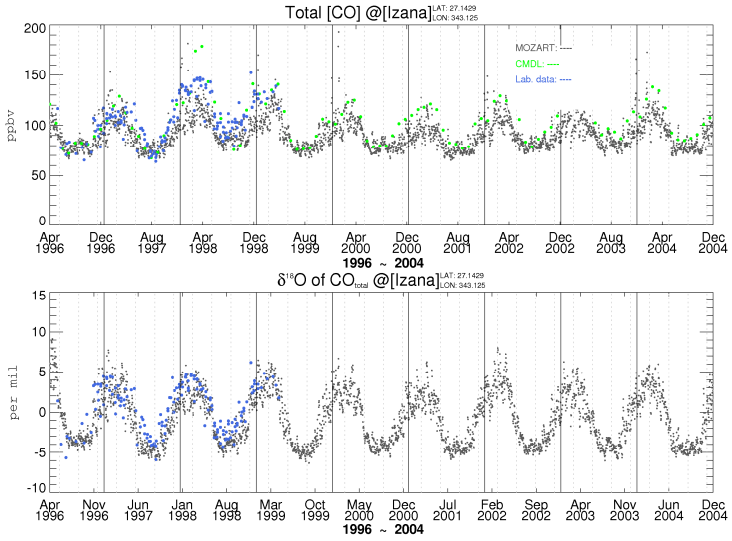
Total [CO] @[Izana] LAT: 27.1429 LON: 343.125
MOZART: ----
CMDL: ----
Lab. data: ----
ppbv
200
150
100
50
0
Apr 1996
Dec 1996
Aug 1997
Apr 1998
Dec 1998
Aug 1999
Apr 2000
Dec 2000
Aug 2001
Apr 2002
Dec 2002
Aug 2003
Apr 2004
Dec 2004
1996 ~ 2004
δ18O of COtotal @[Izana] LAT: 27.1429 LON: 343.125
per mil
15
10
5
0
-5
-10
Apr 1996
Nov 1996
Jun 1997
Jan 1998
Aug 1998
Mar 1999
Oct 1999
May 2000
Dec 2000
Jul 2001
Feb 2002
Sep 2002
Apr 2003
Nov 2003
Jun 2004
Dec 2004
1996 ~ 2004

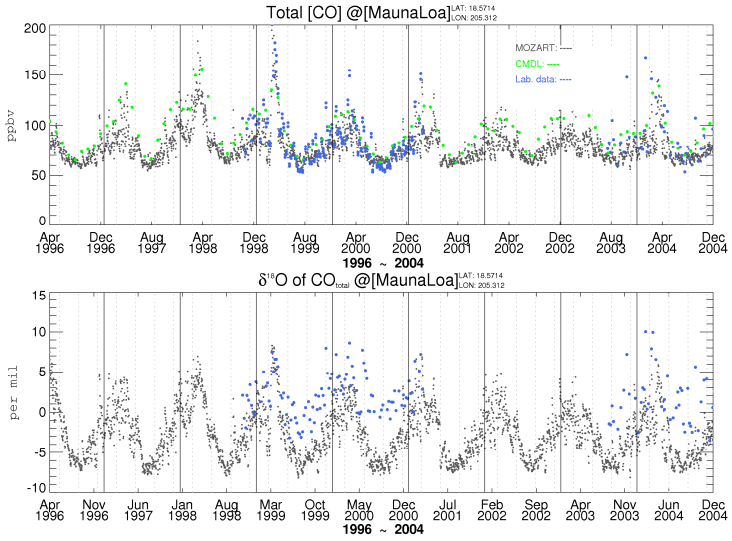
Total [CO] @[MaunaLoa] LAT: 18.5714 LON: 205.312
MOZART: ----
CMDL: ----
Lab. data: ----
ppbv
200
150
100
50
0
Apr 1996
Dec 1996
Aug 1997
Apr 1998
Dec 1998
Aug 1999
Apr 2000
Dec 2000
Aug 2001
Apr 2002
Dec 2002
Aug 2003
Apr 2004
Dec 2004
1996 ~ 2004
δ18O of COtotal @[MaunaLoa] LAT: 18.5714 LON: 205.312
per mil
15
10
5
0
-5
-10
Apr 1996
Nov 1996
Jun 1997
Jan 1998
Aug 1998
Mar 1999
Oct 1999
May 2000
Dec 2000
Jul 2001
Feb 2002
Sep 2002
Apr 2003
Nov 2003
Jun 2004
Dec 2004
1996 ~ 2004

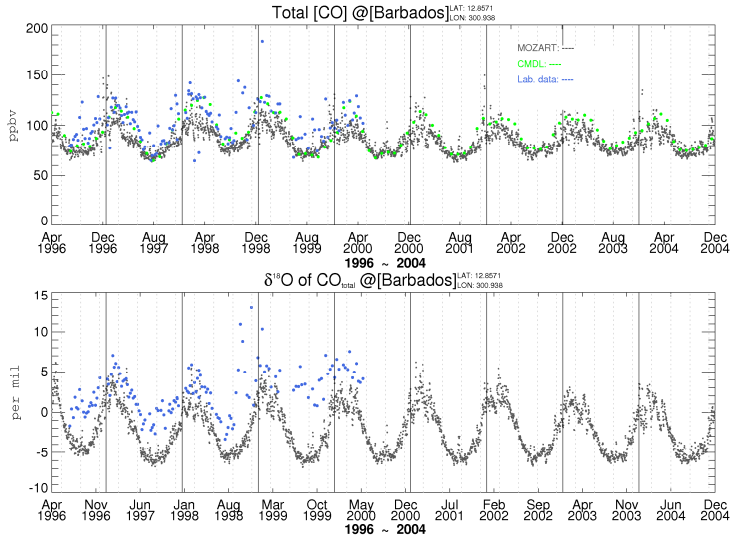
Total [CO] @[Barbados]LAT: 12.8571 LON: 300.938
MOZART: ----
CMDL: ----
Lab. data: ----
ppbv
200
150
100
50
0
Apr 1996
Dec 1996
Aug 1997
Apr 1998
Dec 1998
Aug 1999
Apr 2000
Dec 2000
Aug 2001
Apr 2002
Dec 2002
Aug 2003
Apr 2004
Dec 2004
1996 ~ 2004
δ18O of COtotal @[Barbados]LAT: 12.8571 LON: 300.938
per mil
15
10
5
0
-5
-10
Apr 1996
Nov 1996
Jun 1997
Jan 1998
Aug 1998
Mar 1999
Oct 1999
May 2000
Dec 2000
Jul 2001
Feb 2002
Sep 2002
Apr 2003
Nov 2003
Jun 2004
Dec 2004
1996 ~ 2004

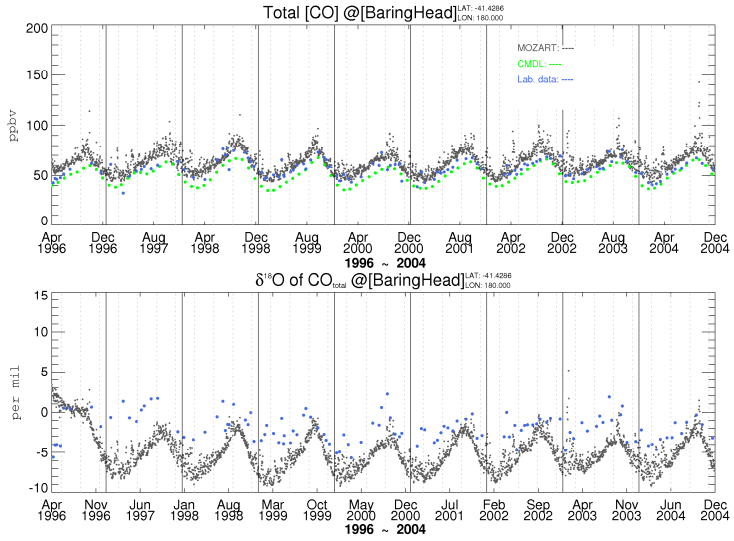
Total [CO] @[BaringHead]LAT: -41.4286 LON: 180.000
MOZART: ----
CMDL: ----
Lab. data: ----
ppbv
200
150
100
50
0
Apr 1996
Dec 1996
Aug 1997
Apr 1998
Dec 1998
Aug 1999
Apr 2000
Dec 2000
Aug 2001
Apr 2002
Dec 2002
Aug 2003
Apr 2004
Dec 2004
1996 ~ 2004
δ18O of COtotal @[BaringHead]LAT: -41.4286 LON: 180.000
per mil
15
10
5
0
-5
-10
Apr 1996
Nov 1996
Jun 1997
Jan 1998
Aug 1998
Mar 1999
Oct 1999
May 2000
Dec 2000
Jul 2001
Feb 2002
Sep 2002
Apr 2003
Nov 2003
Jun 2004
Dec 2004
1996 ~ 2004

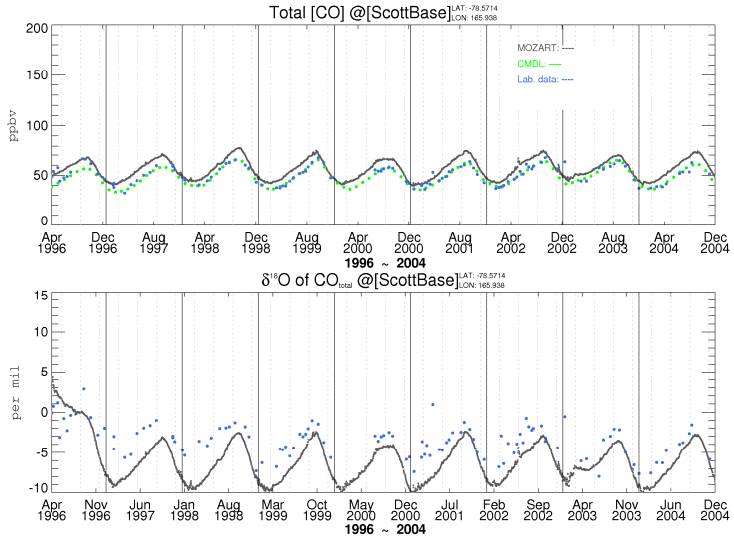

5.2 Simulated CO and $\delta^{18}O$ from each source of CO

5.2.1 Oxidation from Methane

Globally, methane oxidation is the single biggest source of CO (Table 1.1 and Table 3.1) except during the winter of Northern Hemisphere high latitude where the fossil fuel contribution is dominant. Since methane derived CO is produced from the CH_4 + OH reaction (Figure 5.4), it is controlled by the OH concentration which is dependent on sunlight and thus has a seasonal variation. However, OH reacts with CO and removes it from the atmosphere as well, so the net seasonal variation of methane-derived CO is reduced and is less than 5ppbv

(Appendix B). Also, its interannual variation is small compared to other sources, since the life time of CH_4 is long (~10years) and the change of CH_4 reservoir over time is small. The annual CO production from the methane oxidation in this simulation is 875TgCO/yr (Table 3.1) and is close to the top end of previous estimates (Figure 1.1).

Table 5.2 1997 – 2004 averaged source contribution at each station (ppbv)

	Fossil fuel	Biomass burning	CH4 oxidation	NMHC oxidation	Biofuel	Biogenic	Ocean	Total
ALT	33.9	12.4	26.6	20.3	11.5	9.9	0.7	115.1
ZEP	38.0	12.7	26.7	20.8	12.5	10.1	0.7	121.4
ICE	38.9	11.3	27.1	20.5	11.4	10.7	0.9	120.9
IZO	18.2	9.4	29.1	17.0	10.2	5.0	0.4	89.4
MLO	11.8	8.6	28.4	13.9	10.2	3.6	0.4	77.0
RPB	13.7	9.8	31.6	14.3	9.1	4.1	0.7	83.3
BHD	3.1	8.4	26.1	14.7	2.4	3.8	1.9	60.4
SCO	2.5	7.4	24.7	12.0	2.2	2.9	1.6	53.3

Carbon monoxide yield from methane oxidation (α_{CH4}) has been estimated to be less than 1 (0.82, Tie et al., [1992]; 0.7, Manning et al., [1997]; Novelli et al., [1999]; 0.86, Bergamaschi et al., [2000b]; 0.95). In this study, α_{CH4} is assumed as 1 and this is also derived in recent studies ([Duncan et al., 2007] and [Kasibhatla et al., 2002]). In a high-NOx environment, CH_4 is rapidly oxidized to formaldehyde (Figure 5.4). Since the lifetime of formaldehyde is short (ca. 5

hours, Arlander et al., 1995), it photodissociates or reacts with OH and produces CO rather than scavenged in clouds or fogs [Jacob, 2000]. Thus, in high-NOx condition, there is no significant removal process of chemicals in the CH_4 oxidation chain. In a low-NOx environment [Kleinman, 1991], a relatively long lived intermediate methyl hydroperoxide (CH_3OOH) is produced in CH_4 to CO reaction paths. The lifetime of CH_3OOH is hours to days in warm and sunlit conditions [Wang et al., 2002; Jaeglé et al., 2000] and several weeks in cold and dark condition [Snow et al., 2003]. However, due to the low solubility of CH_3OOH [Magi et al., 1997], its deposition velocity is assumed very small. Therefore, during the CH_4 + OH → CO, no noticeable atmospheric losses of intermediates have been reported, and a yield of 1 is assumed for CO. However, compared to the high-NOx environment, in a low-NOx environment, there are more chances of scavenging which results $\alpha_{CH4} < 1$ since the lifetime of CH_3OOH is relatively long. This implies that Southern Hemispheric α_{CH4} is likely smaller than Northern Hemisphere's since the concentration of NOx in Southern Hemisphere is lower than in the Northern Hemisphere [Kasibhatla et al., 1993]. In Manning et al., 1997, $\alpha_{CH4} < 0.8$ is obtained from the isotope mass balance calculation using Southern Hemispheric CO and isotope measurement. In this study, the optimized methane oxidation source consistently suggested to increase current methane-derived CO inventory by 10% in Northern Hemisphere and decrease by 3% in Southern Hemisphere (discussed in chapter 6) implying α_{CH4} of

Southern Hemisphere is relatively smaller than that of the Northern Hemisphere. Plus, the under estimation of methane oxidation source in Southern Hemisphere was speculated in the previous section.

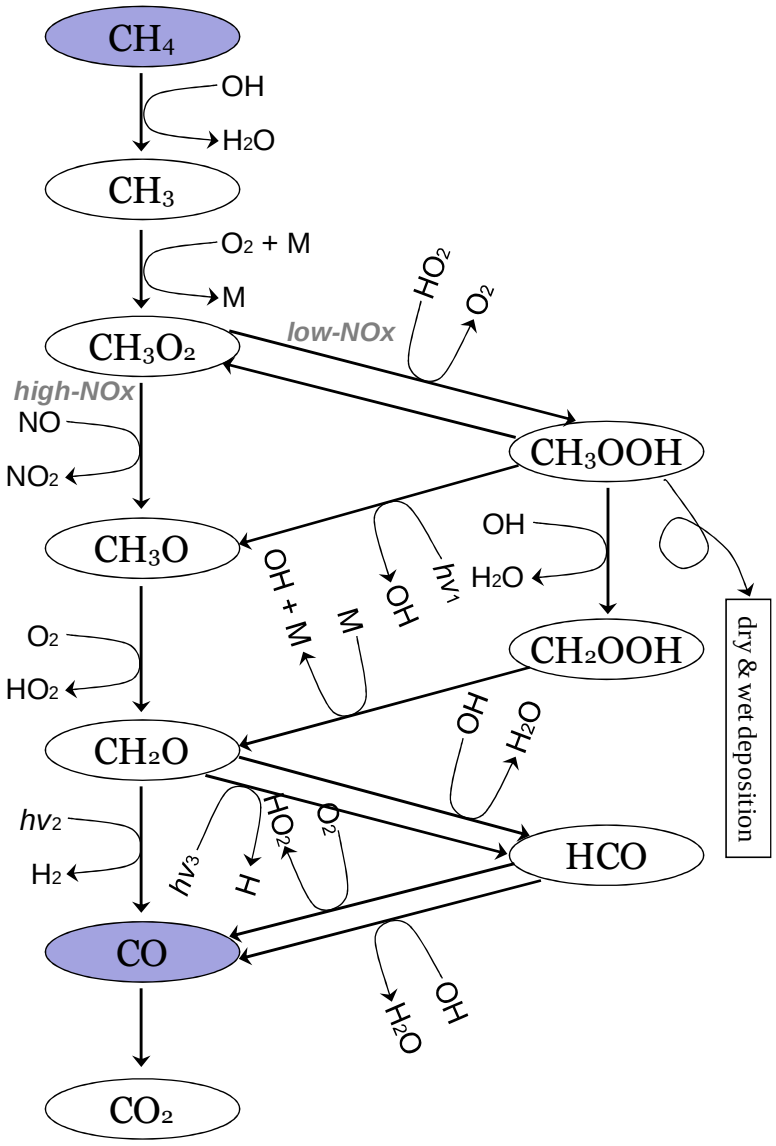

Figure 5.4 Reaction scheme of CO production from CH_4 oxidation [Brasseur et al., 1999]

For simulated $\delta^{18}O$, even though the methane derived CO is the largest component of total CO distribution, the concentration of CO from methane oxidation is fairly constant temporally and spatially in the atmosphere (Appendix A) since CH_4 itself is rather ubiquitous in the troposphere. Its influence to the seasonal and interannual variation of total isotope ratio is not significant.

5.2.2 Oxidation from NMHC (Non-methane hydrocarbon)

Non-methane hydrocarbon (NMHC) oxidation is one of the major sources of CO, and most NMHCs are produced from vegetation [Guenther et al., 1995; Bergamaschi et al., 2000a; Pacifico et al., 2009]. More than 50% of NMHC (biogenic + anthropogenic) derived CO is from the oxidation of isoprene and the monoterpenes [Pfister et al., 2007; Duncan et al., 2007; Bergamaschi et al., 2000a]. Therefore, this source is sensitive to vegetation distribution and environmental parameters including temperature, sunlight, and soil moisture [Guenther et al., 1995; Guenther et al., 2006; Müller et al., 2008]. In this study, the *a priori* estimate of annual production of CO from NMHC oxidation is 230TgCO in the Southern Hemisphere and 310TgCO in the Northern Hemisphere and most of this is produced in the tropics (Table 3.1). Seasonal variation of NMHC derived [CO] in the tropical region (2.4ppbv; IZO, MLO and RPB) is

smaller than that in high latitudes (12.1ppbv; ALT, ZEP, ICE) since both OH concentration and NMHC emission are relatively constant year round (Table 5.2 and Appendix B). In high latitudes, the minimum in NMHC derived CO occurs in early summer because the sunlight reached maximum. NMHC derived CO sharply increases and reaches a maximum in late summer to early autumn since the sink reaction decreases while the maximum biogenic NMHC emission is occurred in late summer [Palmer et al., 2006]. Also, CO production from the NMHC oxidation is very sensitive to the variation of interannual climate conditions such as ENSO since plant emissions are taking a dominant part of the NMHC source. Details about the interannual variation of the NMHC source are described in chapter 6.

Along with the methane oxidation source, the NMHC oxidation source has the most depleted oxygen isotope source (0‰). Because NMHC-derived CO shows relatively stronger seasonality and interannual variability than that of CO from methane oxidation, it is critical to understand the change of $\delta^{18}O$ in the troposphere. In the Northern Hemisphere high latitudes, the most depleted $\delta^{18}O$ from NMHC oxidation was captured in the model in early summer due to increased sunlight and not enough local NMHC production. Also, the NMHC derived CO transported from the low latitudes are relatively more depleted because $C^{18}O$ is preferentially removed from CO pool reacting with OH. After reaching the $\delta^{18}O$ minimum, it is rapidly enriched in the atmosphere until mid-

autumn because sunlight starts to decrease and the local NMHC production is enough to provide relatively $\delta^{18}O$-enriched NMHC derived CO. $\delta^{18}O$ of CO from NMHC oxidation in low latitudes is approximately -10‰ and quite constant since there is relatively little seasonal variation of [OH] [Spivakovsky et al., 2000] and high isoprene production compared to high latitudes [Guenther et al., 1995; Müller et al., 2008]. In the Southern Hemisphere, the most NMHC is emitted from the tropics. The NMHC-derived $\delta^{18}O$ in the extra-tropical area shows strong seasonality since it is remote from the source regions: tropics. The minimum $\delta^{18}O$ occurred in austral summer and it reached below -15‰ because of high OH concentration and little local NMHC emission.

Table 5.3 1997 – 2004 averaged oxygen isotope source signatures at each station (‰)

	Fossil fuel	Biomass burning	CH4 oxidation	NMHC oxidation	Biofuel	Biogenic	Ocean	Total
ALT	19.0	9.7	-8.7	-8.3	10.4	-5.5	7.8	3.9
ZEP	19.5	10.0	-8.6	-8.1	11.1	-5.3	8.2	4.8
ICE	19.5	9.1	-8.5	-8.2	10.4	-5.0	9.8	4.6
IZO	15.8	6.6	-8.7	-10.3	8.3	-9.5	4.1	-0.3
MLO	13.6	5.8	-9.1	-12.0	8.1	-11.9	3.8	-2.1
RPB	13.9	6.1	-8.1	-12.3	7.1	-11.1	8.3	-1.8
BHD	11.5	6.4	-9.0	-10.0	1.0	-8.2	10.4	-5.0
SCO	9.3	5.3	-9.4	-11.8	0.6	-10.5	9.2	-6.1

5.2.3 Fossil and biofuel use

Fossil fuel use is the largest anthropogenic source of carbon monoxide and it plays an important role in CO distribution in the Northern Hemisphere extratropics. Especially in the wintertime, there is little sunlight in high latitudes, thus most CO is accumulated in the atmosphere and it takes the largest part of CO sources. Also, since more than 50% of the total fossil fuel source is produced from the U.S. [U.S.EPA, 2000] and the efficiency of emission control devices are dependent on temperature [Stump et al., 1989], Duncan et al., 2007 estimated the seasonal variation of fossil fuel use as ±8% about the annual mean. In this study, the maximum *a priori* fossil fuel CO emission was prescribed during the spring (MAM; Fig 5.5) and its seasonal variation was ±14% from the annual mean in >30˚N region and ±9% from the annual mean in 30˚S - 30˚N region. Therefore, in the Northern Hemisphere extratropics, CO concentration from fossil fuel combustion increased very fast in the winter and stayed high until spring (Appendix A). In the tropics, its importance is decreased and comparable with the other major sources but CH_4 oxidation. Carbon monoxide emission from the Northern Hemisphere is 340TgCO/yr and that from the Southern Hemisphere is only 25TgCO/yr (Table 3.1). Thus, it is a minor source in Southern Hemisphere. Biofuel use is another major anthropogenic source of CO and it is also biased to

the Northern Hemisphere (NH: 276 TgCO/yr, SH: 38 TgCO/yr).

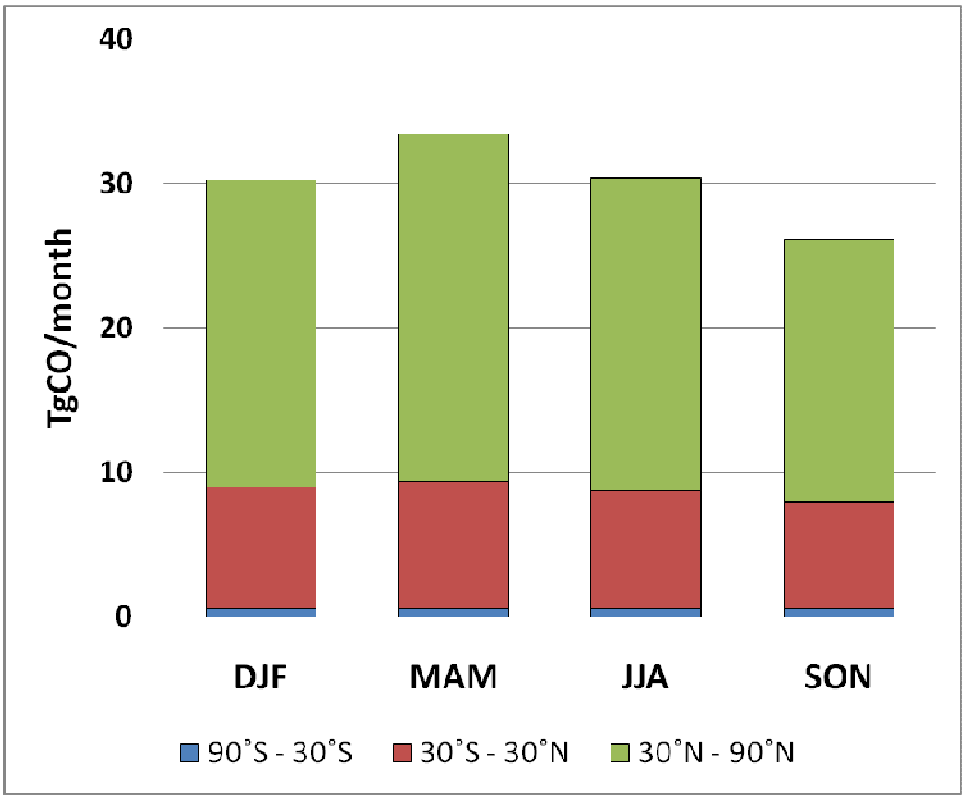

Figure 5.5 *A priori* seasonal distribution of CO from fossil fuel combustion

Carbon monoxide from fossil fuel combustion is the most $\delta^{18}O$ enriched source. In Northern Hemisphere winter high latitudes, $\delta^{18}O$ is dominantly controlled by fossil fuel source due to its high concentration and enriched isotopic signature. However its influence on $\delta^{18}O$ decreases in the low latitudes and is minor in the Southern Hemisphere.

5.2.4 Biomass burning source

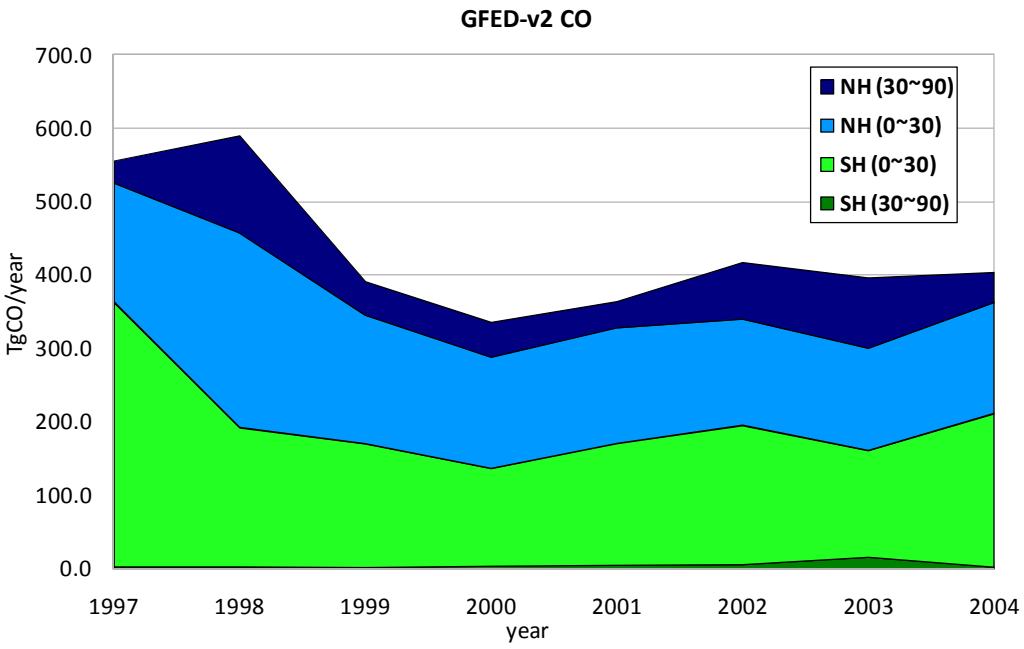

Figure 5.6 Interannual variation of zonal distribution of GFED-v2 CO emission

Biomass burning is another main source of atmospheric carbon monoxide and exhibits a strong seasonality. Especially in the Southern Hemisphere, the correlation between NMHC-derived CO and CO from biomass burning is strong (ρ_{BHD} = 0.77, ρ_{SCO} = 0.63) since both sources are actively produced in the same region (tropics; <30˚S) and during the same season (dry season; June ~ November) (Appendix B). According to the GFED-v2 CO emission inventory [van der Werf et al., 2006], due to the difference in land distribution between Northern Hemisphere and Southern Hemisphere, approximately 97% of biomass

burning CO is produced in the tropics in the Southern Hemisphere and 73% in the Northern Hemisphere (Figure 5.6).

In comparison with the other sources of CO, biomass burning has a large interannual fluctuation. However, MOZART-4 with the GFED-v2 inventory captured the biomass burning signals very well in both concentration and isotope ratio. For instance, a huge CO peak was detected at Mauna Loa in spring 1999 (Fig 5.3). Based on model simulations, strong biomass burning events from south Asia increased the concentration and the modeling results agreed very well to the observed concentration and $\delta^{18}O$.

The oxygen isotope signature of biomass burning has been reported to have a wide range [Kato et al., 1999] since it is affected by various factors such as burning temperature (flaming and smoldering), vegetation species, and $\delta^{18}O$ of precipitation. Also, its very limited field measurements add an additional error to the isotope source signature estimation. Despite the difficulties of specifying a number for $\delta^{18}O$ of biomass burning source, an averaged isotope source signature is still very useful in constraining the CO budget in global or hemispheric scale [Bergamaschi et al., 2000a]. It was reported from 15‰ to 18‰ [Stevens and Wagner, 1989; Brenninkmeijer, 1993; Bergamaschi et al., 1998] and the similar results of the $\delta^{18}O$ of biomass burning are estimated in this study through the sensitivity test and Keeling plot method (discussed in section 5.4 and 5.5). In the Northern Hemisphere high latitudes, where the contribution of $\delta^{18}O$ enriched

source - fossil fuel use - is significant, the influence of widely ranged potential $\delta^{18}O$ of biomass burning to the source strengths is considered as minimal because the biomass burning source signatures are close to the atmospheric δ18O (Table 5.3). However, accurate estimation of isotopic source signature from the biomass burning is important for $\delta^{18}O$ simulation in tropics and in the Southern Hemisphere.

Because, the $\delta^{18}O$ from combustion processes (e.g. biomass burning) are more enriched in ^{18}O compared to NMHC-derived CO (Table 1.2), it provides a useful constraint separating the biomass burning source to the NMHC oxidation source which is very limited by concentration information solely. Especially in the Southern Hemisphere, since NMHC derived CO and biomass burning CO are produced from the same region and season with similar source strengths, the oxygen isotope information provides useful information to separate the sources.

The seasonal variation of $\delta^{18}O$ from biomass burning is similar to that from NMHC oxidation except in tropic regions. The seasonality is found in tropics as well since wild fires are active during the dry season while NMHC oxidation is quite constant year-round.

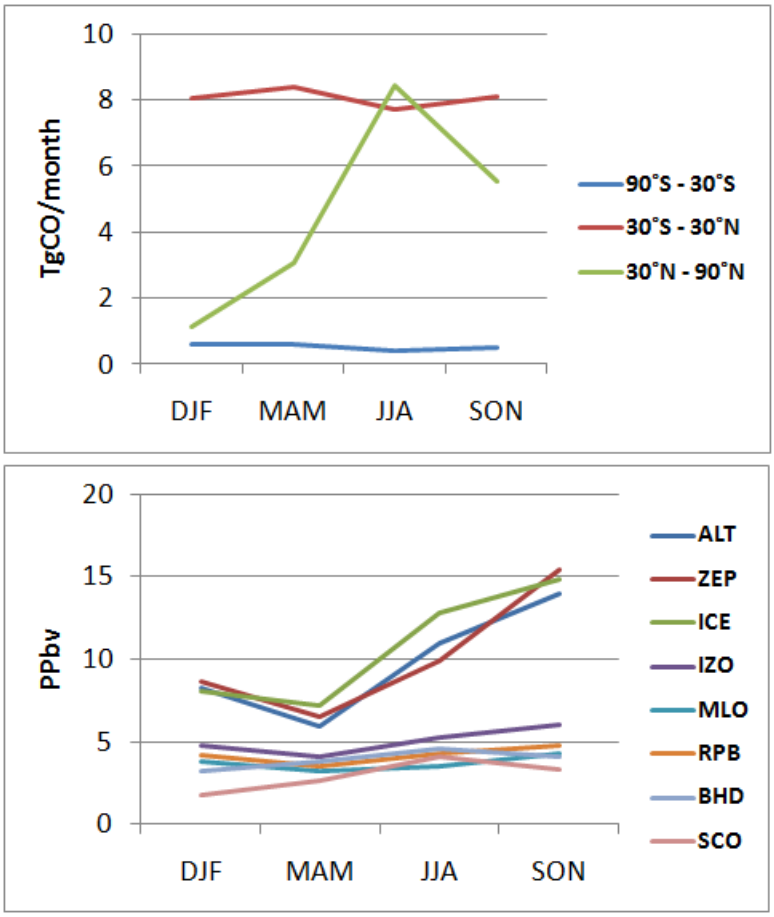

Figure 5.7 Seasonal distribution of biogenic CO emission (upper panel) and modeled CO concentration from the biogenic emission (bottom panel)

5.2.5 Other sources

The effect of CO emissions from the minor CO sources (direct biogenic emission: 160TgCO/year and oceanic emission: 20TgCO/year) to the total CO concentration is very limited in global scale and they can be considered in small temporal and regional scales such as in forest or in coastal area. Similar to

biogenic NMHC emissions, direct biogenic CO emission showed a maximum during summer (JJA) in the Northern Hemisphere high latitude (Figure 5.7). In the tropics, the emissions kept relatively high year-round with little seasonal variation. In the Southern Hemisphere extratropics, the emission was negligible due to the small land cover. The maximum biogenic [CO] was observed during autumn months (SON) because the sunlight is declining while the residual of summer biogenic [CO] is still influencing the SON biogenic [CO]. Despite the high biogenic emissions of tropics, direct biogenic [CO] is smaller than 5 ppbv because of high OH concentration. The influence of the minor sources to the $\delta^{18}O$ is also tiny due to their small contribution for total CO concentration.

5.3 Inter-hemispheric mixing of CO

The effect of CO sources emitted from the opposite hemisphere was quantified for fossil fuel, biofuel and biomass burning CO. Table 5.4 shows the contribution of Southern Hemispheric fossil fuel, biofuel and biomass burning at the Northern Hemispheric stations. In the Northern Hemisphere, the effect of Southern Hemispheric anthropogenic sources was minimal due to their small source strengths. In the Southern Hemisphere, Northern Hemispheric anthropogenic (fossil fuel and biofuel use) CO accounts for up to 53% of total biofuel [CO] and 40% of total fossil fuel [CO]. The contributions of Northern

Hemispheric anthropogenic sources are close to 50% of the total Southern Hemispheric anthropogenic CO, because of the ten times smaller Southern Hemispheric anthropogenic CO emission. The concentration of Northern Hemispheric anthropogenic CO is 2.2 ~ 3.1 ppbv which is corresponding to the less than 2% of total [CO] and implies limited transport of Northern Hemispheric anthropogenic CO. Thus the importance of inter-hemispheric exchange of anthropogenic sources to the Southern Hemispheric CO mixing ratio is not significant.

Table 5.4 Influence of emissions of opposite hemisphere at each station

Station	ALT	ZEP	ICE	IZO	MLO	RPB	BHD	SCO
SH-[CO]ff/total-[CO]ff	0.3%	0.2%	0.2%	0.9%	1.9%	1.4%	66.0%	60.4%
SH-[CO]ff/total-[CO]	0.1%	0.1%	0.1%	0.2%	0.3%	0.2%	98.3%	98.3%
NH-[CO]ff/total-[CO]ff	99.7%	99.8%	99.8%	99.1%	98.1%	98.6%	34.0%	39.6%
NH-[CO]ff/total-[CO]	99.9%	99.9%	99.9%	99.8%	99.7%	99.8%	1.7%	1.7%
SH-[CO]bf/total-[CO]bf	1.6%	1.4%	1.6%	3.5%	3.9%	5.2%	47.3%	47.2%
SH-[CO]bf/total-[CO]	0.1%	0.1%	0.1%	0.4%	0.5%	0.5%	98.1%	98.0%
NH-[CO]bf/total-[CO]bf	98.4%	98.6%	98.4%	96.5%	96.1%	94.8%	52.7%	52.8%
NH-[CO]bf/total-[CO]	99.9%	99.9%	99.9%	99.6%	99.5%	99.5%	1.9%	2.0%
SH-[CO]bb/total-[CO]bb	8.1%	7.7%	8.9%	19.1%	21.3%	26.0%	83.7%	82.4%
SH-[CO]bb/total-[CO]	0.8%	0.8%	0.8%	1.9%	2.3%	2.9%	97.9%	97.7%
NH-[CO]bb/total-[CO]bb	91.9%	92.3%	91.1%	80.9%	78.7%	74.0%	16.3%	17.6%
NH-[CO]bb/total-[CO]	99.2%	99.2%	99.2%	98.1%	97.7%	97.1%	2.1%	2.3%

Most of the biomass burning CO is produced from the low latitudes. 1997~2004 mean GFED-v2 inventory estimated 168Tg of CO is emitted from

between 0˚ and 30˚N and 195Tg of CO is emitted from between 0˚ and 30˚S which takes 73% and 97% of Northern Hemispheric and Southern Hemispheric biomass burning CO respectively (Fig 5.6). Since the majority of biomass burning occurred in the tropics (30˚S ~ 30˚N), comparing with the anthropogenic CO sources, relatively larger inter-hemispheric exchange of CO was expected. However, during the simulation period, in general, the effect of biomass burning CO from the opposite hemisphere was approximately 20% in low and mid latitude stations and it was less than 10% in high latitude stations (Table 5.4) while the influence of some intense wild fire events such as in October 1997 was calculated to be close to 50% of total biomass burning CO for some stations. The contribution of biomass burning CO for the opposite hemisphere to the total CO concentration was less than 3% for both hemispheres.

[Williams et al., 2002] performed aircraft measurements, during the winter monsoon (January ~ March 1999), across the ITCZ over the Indian Ocean between 0' and 10'S. They observed a sharp gradient of CO and O_3 mixing ratio across the ITCZ in the lower tropical free troposphere (approximately 0 ~ 8km). Also, Mak and Brenninkmeijer, 1998 measured CO concentration and isotopes in the free troposphere across the Pacific ITCZ in both August and February. They found a sharp concentration change at 10˚N ~ 20˚N during summer at the summertime mean location of ITCZ. These studies imply transport of CO across the ITCZ is limited. [Staudt et al., 2001] evaluated the effect of Southern

Hemispheric anthropogenic and biomass burning sources to the [CO] over the northeastern tropical Pacific (10˚N ~ 34˚N) based on their March to April 1999 model result. Southern Hemisphere anthropogenic (fossil fuel + biofuel) CO to the total anthropogenic CO was estimated at 2.9% and they derived 7.4% contribution of Southern Hemispheric biomass burning CO to the total biomass burning CO. Furthermore, the concentration of OH in the tropic regions is higher than the mid- and high latitudes [Emmons et al., 2010], this also restricts transport of CO across the tropics. The model simulation results performed in this study are consistent with these studies showing the insignificant contribution of CO from opposite hemisphere.

In the tropical Northern Hemisphere, the onset of biomass burning occurs in late fall and subsides in the beginning of wet season (NH late spring) [Sanhueza, 1999]. During the biomass burning season, the ITCZ is located in the Southern Hemisphere or near the equator. Thus, NH biomass burning plumes are dominantly transported northward. In the Southern Hemisphere, since the ITCZ is mainly oscillated in the NH, southern hemispheric biomass burning CO is prevalently transported towards the south regardless of its season. Therefore, despite most of biomass burning CO being produced in low latitudes, their inter-hemispheric exchange is limited because of the relation between the position of ITCZ and burning season.

5.4 Estimation of oxygen isotopic source signature from biomass burning

Since biomass burning has a strong seasonality and also is affected by interannual climate variations, its CO source strength is more difficult to estimate. At the onset of biomass burning, the concentration of carbon monoxide increases rapidly where the plume passes through (ex. 1999 Mauna Loa, Figure 5.3). Plus, the biomass burning events influence isotope composition of the air masses as well, while its impact to the $\delta^{18}O$ is varied by the source compositions of each location. Thus using isotope data sets along with concentration provides detailed information about the biomass burning source. However, because of the widely ranging oxygen isotope source signature reports, to constrain the biomass burning source on the global or hemispheric scale, it is important to use a reliable representative $\delta^{18}O$ source signature in the analyses.

In this study, the Keeling plot method is used to estimate the oxygen isotopic source signature. Its basis is the conservation of mass and the brief description of the method is as follows. If concentration of a background air is increased by a specific source, the background isotopic composition is also influenced by the source. By plotting the relationship between the reciprocal of concentrations and the isotopic ratios, the y-intercept of the regression line gives us the estimated isotopic ratio of the source. The Keeling plot has been used to

extract information on the isotopic composition of ecosystem fluxes and shown robust results [Keeling, 1958; Keeling, 1961; Pataki et al., 2003]. This technique also been applied to estimate isotopic source signatures of CO [Brenninkmeijer et al., 1999; Tsunogai et al., 2003; Saurer et al., 2009].

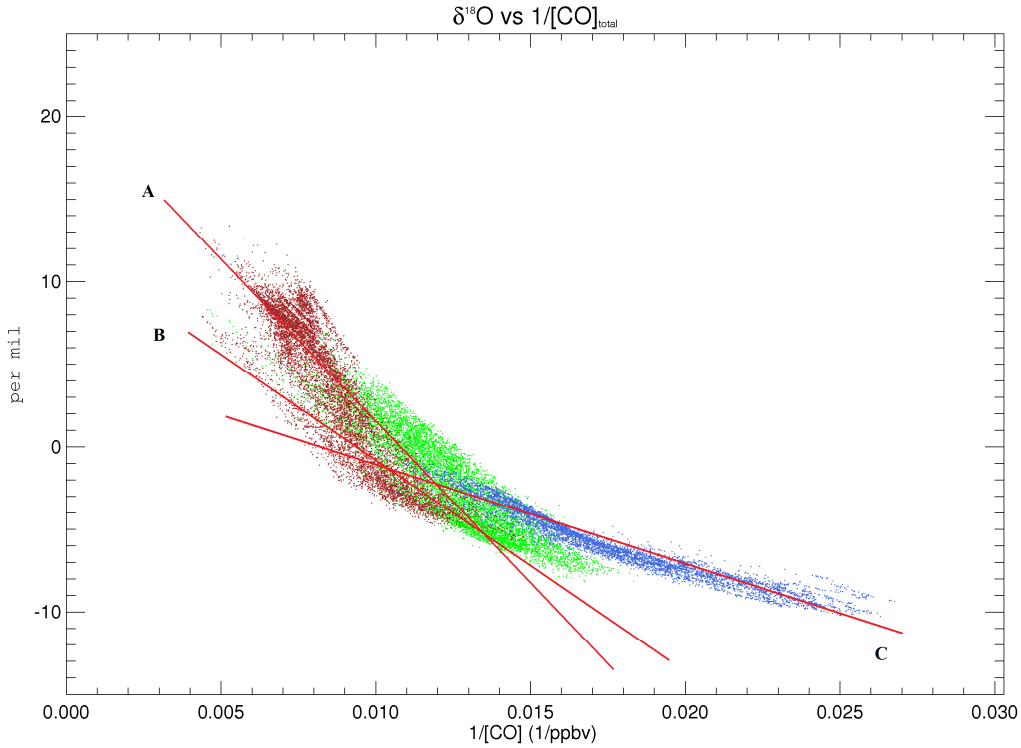

Figure 5.8 Modeled $\delta^{18}O$ of CO as a function of the inverse of the [CO]. Blue dots are the SH station (BHD and SCO) data sets, green dots are the NH mid- and low-latitude station (IZO, MLO and RPB) data sets, and brown dots are the NH high-latitude station (ICE, ZEP and ALT) data sets. The regression lines are estimated.

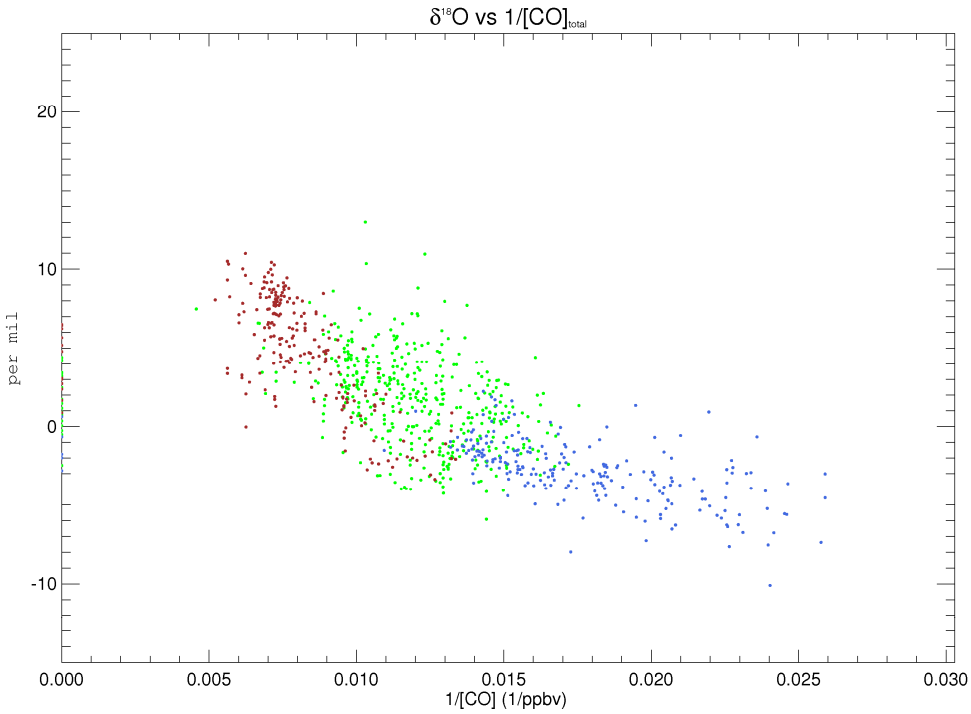

Figure 5.9 Same as Figure 5.8 but data sets are taken from real measurements

In Figure 5.8, modeled $\delta^{18}O$ and 1/[CO] are plotted for all 8 stations. Three slopes can be identified in the plot. The steepest slope (slope A) is comprised of data points presumably influenced by the fossil fuel source, which is the most enriched in oxygen-18. The data points comprising slope B is classified as those most reflecting biomass burning. The data sets where the CH_4 oxidation and NMHC oxidation sources (the most depleted sources) are most important fall along the slope C. These three slopes are also found in the observational data sets (Figure 5.9).

However, to estimate the isotopic source signatures quantitatively, it is necessary to choose observations dominantly affected by a source or a source mixture whose isotopic source signature will be estimated because there are five main sources of atmospheric CO: fossil fuel use, biofuel use, biomass burning, methane oxidation, and NMHC oxidation. Therefore, first, to best estimate the individual isotopic source signals, model results are used to look at the specific observations. Using MOZART output, the measurements where the contribution of biomass burning source is higher than 20% were selected. Next, the Northern Hemisphere high-latitude observations where dominantly influenced by fossil fuel source (Table 5.2) are removed since it is potentially masking the effect of biomass burning on the isotopic signatures even though its contribution is comparable. Plus, the Keeling plot method is valid when background air is influenced by a source or source mixture [Saurer et al., 2009]. Thus, the NH high-latitude measurements were hard to be used in this analysis since the fossil fuel source is independently added. In Figure 5.8, fossil fuel CO is added following the slope A while biomass burning CO is added following the slope B.

When the Keeling plot method is applied to a global scale carbon monoxide study, in contrast to long-lived trace gases such as carbon dioxide, the isotope fractionation occurring during the sink reaction can affect the result. During transportation, the CO + OH reaction continuously removes CO from the atmosphere and $\delta^{18}O$ becomes progressively more negative. Therefore, the

estimated isotopic source signature should take into account the kinetic isotope effect. However, in this study, the effect of the sink reaction is considered to be minimized because the observation stations used in this analysis are located in tropics or mid-latitude sites which are in close proximity to the source of biomass burning. Moreover, since observations where biomass burning comprises more than 20% of total [CO] is included in the analysis, the regression line showed in Figure 5.10 has a good linearity (r^2 = 0.714). This indicates a single source or source mixture having a relatively constant source composition is added to the background [CO] and the KIE of CO + OH reaction is insignificant. So, the observations fall along the regression line [Tsunogai et al., 2003; Saurer et al., 2009].

Figure 5.10 shows the result of the Keeling plot analysis and the estimated $\delta^{18}O$ source signature (y-intercept) was 9‰ and its slope was similar to slope B in Figure 5.8. However, this needs an additional interpretation because biomass burning is not a single source contributing the [CO] addition but the mixture of biomass burning and other CO sources contributed the addition. Thus, based on the modeled source distribution, the source signals are described below.

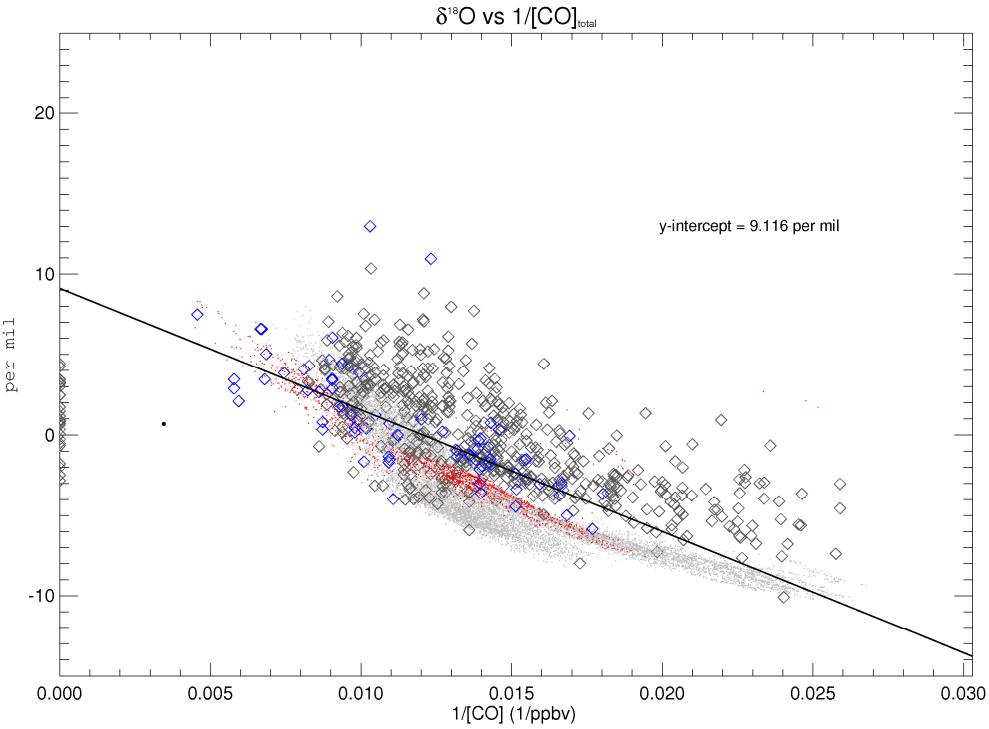

Figure 5.10 Modeled (small dots) and measured (open diamonds) $\delta^{18}O$ of CO as a function of 1/[CO]. The NH high-latitude data sets are removed. The red dots are modeled data sets where the contribution of biomass burning is greater than 20%. The blue diamonds are observations corresponding to the red dots. The regression line is calculated based on the blue diamonds and its y-intercept is 9.12‰; the two data points $\delta^{18}O$ >10 ‰ are excluded.

Since the source composition of the observations following the Keeling plot is considered as relatively constant, the y intercept of the Keeling plot (Y) can be expressed as:

$$Y = \sum_i \alpha_i \delta_i \qquad \text{(Eqn. 5.3)}$$

where α is source contribution of a source i and δ is isotope source signature of

source *i*.

And an unknown isotope source signature of source *x* (δ_x) can be derived from rearranging Eqn. 5.3:

$$\delta_x = \frac{Y - \sum_j \alpha_j \delta_j}{\alpha_x} \qquad \text{(Eqn. 5.4)}$$

where $j = i$ except x.

In the Keeling plot analysis (Figure 5.10) the mean contribution of fossil fuel was 8.5% and its $\delta^{18}O$ is relatively known precisely compared to the other sources (Table 1.1). Thus, the influence of the fossil fuel source is removed by applying Equation 5.4 and the biofuel source is combined with biomass burning since, in term of $\delta^{18}O$, CO is produced from the same process: 'burning wood or plants'. The relation of the other sources (methane oxidation, NMHC oxidation, and biofuel + biomass burning) is shown in Figure 5.11. The oxygen isotope source signature was estimated at 21‰ with the $\delta^{18}O$ of NMHC oxidation and CH_4 oxidation used in the forward model simulation: 0‰ for both sources.

[Kato et al., 1999] reported $\delta^{18}O$ higher than 23.5‰ which is $\delta^{18}O$ of atmospheric oxygen, from their controlled laboratory plants burning experiment. They suggested that since $\delta^{18}O$ of cellulose is typically higher than 23.5‰ [Saurer et al., 1997] the oxygen in the cellulose is also involved in CO production in the biomass burning. Moreover, during the dry condition which is also biomass burning favorable condition, $\delta^{18}O$ of cellulose is more enriched [Burk and Stuiver,

1981; Saurer et al., 2000] and CO takes more than 50% of gases produced from the pyrolysis of cellulose [*Lin et al.*, 2009]. This estimated isotopic signature is significantly higher than all previously reported $\delta^{18}O$ of biomass burning estimates. In order to get a more reliable biomass burning oxygen isotope signature, further research about more accurate $\delta^{18}O$ estimation of CH_4 oxidation and NMHC oxidation sources are required because $\delta^{18}O$ of these sources are important parameters determining $\delta^{18}O$ of biomass burning from the Keeling plot method (Figure 5.11)

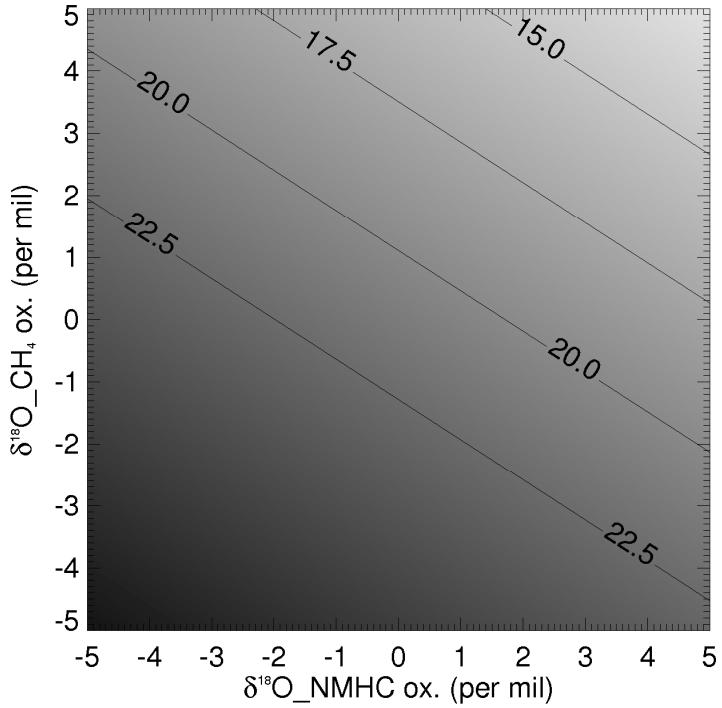

Figure 5.11 Estimated $\delta^{18}O$ of biomass burning as a function of $\delta^{18}O$ of NMHC oxidation and CH4 oxidation

5.5 The effect of $\delta^{18}O$ of biomass burning to $\delta^{18}O$ simulation

The sensitivity of the modeled $\delta^{18}O$ to different $\delta^{18}O$ source signatures of biomass burning and biofuel sources has been determined. Biomass burning is a major source of CO but the isotopic signature of this source is hard to define because it varies with burning stage (temperature) and vegetation type [Kato et al., 1999] (Table 1.2). In the mid- to high-latitude NH, where the influence of oxygen enriched fossil fuel source is large, $\delta^{18}O$ is less sensitive to the change of $\delta^{18}O$ values from biomass burning because its possible isotopic signatures are similar to the range of observed $\delta^{18}O$. On the other hand, sensitivity studies demonstrate the effectiveness for constraining the isotopic signature from biomass burning in the tropics (both NH and SH) and extra-tropical Southern Hemisphere because the contribution from fossil fuel is not significant in those areas. Previously, $\delta^{18}O$ from biomass burning has been reported to be 16.3‰ from burning organic matter in the laboratory [Brenninkmeijer 1993] and 18±1‰ from a controlled burn of pine forest. [Stevens and Wagner, 1989]. The sensitivity tests are consistent with this as a globally averaged signature. The tracer version of MOZART was run with four different oxygen isotope signature of biomass burning: 13‰, 15‰, 17.5‰ and 20‰. The results show that the best isotopic ratios are indicated at 20‰ in model-observation difference and the χ^2 between modeled and measured

values are also optimal at 20‰ (Table 5.5). Thus, the globally averaged isotopic source signature of $\delta^{18}O$ from biomass burning is estimated to be close to 20‰. A similar $\delta^{18}O$ from biomass burning was obtained from the Keeling plot discussed in the previous section.

Table 5.5 Statistical comparison of observed and modeled d1 $\delta^{18}O$ for different $\delta^{18}O$ of biomass burning

$\delta^{18}O$ signature (‰)	13	15	17.5	20
correlation (ρ)	0.86	0.86	0.86	0.86
model-obs difference (ppbv)	3.67	3.32	2.93	2.59
χ^2	3.25	2.78	2.29	1.88

6. Optimized Global CO Budget from Joint Inversion of [CO] and $\delta^{18}O$

6.1 Optimized atmospheric CO sources for 1997, 1998 and 2004

The global atmospheric carbon monoxide budget is estimated for 1997, 1998 and 2004 using inversion analyses. The sources are constrained by both CO concentration and oxygen isotope ratio ($\delta^{18}O$) information. Concentration and $\delta^{18}O$ are either simultaneously or sequentially applied to constrain the *a priori* CO sources and the former method is used to discuss the inversion results unless otherwise noted. The results of applying different inversion techniques will be explained more in detail later in this chapter.

Frequently the result of inversion analysis is expressed as correction or optimization factor that is the ratio of a posteriori estimates to the prescribed *a priori* source fluxes.

$$*\textbf{Optimization factor}\ (f)$$

$$f_i = \frac{\hat{x}_i}{x_{a,i}} \qquad \text{(Eqn. 6.1)}$$

where x_a and $x^{\wedge}$ is *a priori* and *a posteriori* source strength of source *i*. Thus, if an optimization factor is greater than 1 then this means the current estimate of a source strength is underestimated and suggested to increase.

6.1.1 Optimized fossil fuel and biofuel source strength

While fossil fuel and biofuel are both anthropogenic sources of CO, the inversion analysis showed very different results (Table 6.1). In the Southern Hemisphere, the optimization factors of fossil fuel and biofuel sources are close to the unity. This implies that the anthropogenic sources of CO in the Southern Hemisphere were accurately estimated. The fossil fuel source changed less than 2% after inversion and biofuel estimates changed less than 5% except in 1997, during which the *a posteriori* biofuel source decreased 15%. Since the anthropogenic sources play a minor role in the Southern Hemisphere, the measurements did not constrain the sources tightly. The reductions of their uncertainties are relatively small compared to those in the northern hemisphere where the sources are major components of total CO concentration.

In the Northern Hemisphere, the optimized fossil fuel emission inventory was adjusted less than approximately ±15% for the three years. This indicates the *a priori* fossil fuel source strength [Pétron et al., 2004] is close to the actual fossil fuel CO emission in both hemispheres. Plus, a slight decreasing trend of the optimization factor is found which suggests carbon monoxide emissions from fossil fuel combustion decreased from +10% (1997) to –13% (2004), in spite of a 20% increase in annual global fossil fuel consumption from 1990 to 2005 [World

Resources Institute, http://earthtrends.wri.org]. Northern Hemisphere biofuel emission changed significantly after the inversion. It increased 79% in 1997 and 64% in 1998, and 31% in 2004. In comparison with the fossil fuel source, the biofuel source showed a larger source adjustment with a larger *a posteriori* error covariance. This indicates there are large uncertainties in biofuel source estimate. The biofuel source also demonstrated downward tendency of optimization factor which indicates the use of biofuel decreased from 1997 to 2004.

Table 6.1 Optimization factors (*f*) and a posteriori uncertainty (*e*) of each CO source

	Fossil Fuel		**Bio. Burn.**		**CH_4 Ox.**		**NMHC Ox.**		**Biofuel**		**Ocean**		**Biogenic**	
	f	***e***	***f***	***e***	***f***	***e***	***f***	***e***	***f***	***e***	***f***	***e***	***f***	***e***
1997NH	1.10	1.7%	1.33	8.8%	1.12	0.8%	0.72	7.8%	1.79	12.6%	1.05	24.9%	0.53	15.1%
1998NH	0.98	2.3%	0.89	4.0%	1.11	0.8%	1.48	9.1%	1.64	12.5%	1.06	24.9%	0.79	20.0%
2004NH	0.87	1.6%	0.94	18.4%	1.10	0.8%	1.07	9.4%	1.31	10.9%	1.00	24.9%	0.47	16.9%
1997SH	0.98	4.0%	0.97	7.5%	0.97	0.6%	0.67	7.0%	0.86	23.0%	0.96	22.2%	0.79	23.1%
1998SH	1.00	4.0%	0.75	6.9%	0.98	0.7%	0.85	7.8%	1.01	23.8%	0.98	22.4%	0.99	23.0%
2004SH	0.99	4.0%	0.93	4.7%	0.98	0.7%	0.52	6.5%	0.96	23.1%	0.98	22.5%	0.84	23.0%

6.1.2 Optimized biomass burning source strength

Since GFED-v2 [van der Werf et al., 2006] inventory was used for the biomass burning source strength in this study which has been extensively used for other biomass burning gas emissions studies [Gloudemans et al., 2009; Wang et al., 2009; Turquety et al., 2008; Chen et al., 2009; Emmons et al., 2010], only small corrections were expected. There was only a small difference between the *a priori* and *a posteriori* source strengths for 1998 and 2004. However, for 1997 during which was a high fire year, the inversion results suggest an increase of 33% for the Northern Hemispheric biomass burning CO indicating GFED-v2 missed some sources of the biomass burning CO. Also, the inventory was not adjusted much for the Southern Hemispheric biomass burning CO. In general, the joint inversion analyses estimated ca. 10% less CO than the GFED-v2 inventory on average.

6.1.3 Optimized chemical oxidation source strengths

The methane oxidation source is the biggest source of CO. However, because its life time is long (~ 10 years) and reservoir is large, this source is already relatively well-constrained compared to the other sources of CO. The joint inversion

analysis confirmed this. For all three years, the optimization factors are relatively constant in each hemisphere; 1.10 ~ 1.12 in the Northern Hemisphere and 0.97 ~ 0.98 in the Southern Hemisphere.

Biogenic NMHC emission is the largest component of the NMHC oxidation source of CO (>80% of total NMHC derived CO; [Duncan et al., 2007; Bergamaschi et al., 2002a]). Isoprene emissions are estimated to be ~ 75% of the total natural NMHC emissions [Pfister et al., 2007]. Therefore, this source is expected to be sensitive to environmental factors such as temperature and precipitation patterns. Since there was a strong El Niño event in 1997 followed by a strong La Niña in 98 – 99, the emission change was clearly seen in the inversion analysis and a strong correlation between ENSO index and NMHC derived CO source was found as well. Also, NMHC derived CO was more sensitively responded to the ENSO index change in the Northern Hemisphere. The interannual variability of NMHC derived CO is addressed more in detail in section (6.3).

6.1.4 Optimized ocean and biogenic source strengths

The optimization factors of the ocean source were close to 1 and *a posteriori* uncertainty was not reduced much. Thus, this source was hardly constrained because of the small influence of the ocean on the atmospheric CO.

The inversion results of direct biogenic CO emission source suggest a reduction of the emission by up to 50%. However, due to the small contribution of the biogenic source, it has limited influence to the global CO. Similar to the ocean source, this source also was not tightly constrained as evidenced by a small reduction in uncertainty of the source.

6.1.5 Comparison to the previous CO sources strength estimates derived from inversion analyses

The global CO budget estimated in this study is compared to previous CO budget estimates (Table 6.2). Although direct comparison between this study and earlier studies is difficult due to the different years of data sets and source categories, most of the *a posteriori* emissions fall within the range of the previous estimates.

Table 6.2 The results of global CO budget estimation (this work) with comparison to previous global CO budget estimates

	a priori	*This work*		*Bergamaschi et al, 2000a*	*Petron et al, 2002*	*Petron et al, 2004*	*Muller and Stavrakou, 2005*	*Kasibhatla et al, 2002*	*Arellano et al, 2004*	*Arellano et al, 2006*
		a posteriori								
Year of observational data		1997	1998	2004	1993-1995	1990-1996	Apr. 2000 -Mar. 2001	1997	1993-1995	2000	Apr.2000 -Apr.2001
Fossil fuel (FF)	365	397	359	321		309	365				
Biofuel (BF)	313	524	489	396		561	318				
FF + BF	678	922	849	716	642	870	683	760	857 (768)	844-923	841
Biomass burning	516	609	498	377	722	606	408	359	561 (467)	508-579	501
Anthropogenic HC oxidation					166						
Biogenic HC oxidation					507				477 (362)	175-209	394
Total NMHC oxidation	543	377	656	454				774			
Methane oxidation	875	923	923	919	830			870	949 (709)	767	820
Ocean	20	20	20	20	23	20		23			
Biogenic	160	100	138	97		167		142			
Total surface emission	1375	1651	1505	1210	1364	1528-1694	1091	1261	1418 (1235)	1352-1502	1342
Total oxidation source	1418	1300	1579	1373	1503	1461-1536	1650	1644			
Total source	2793	2951	3084	2583	2891	2960-3067	2741	2928	2846 (2306)	2294-2478	2556

The total direct CO emission was 1210 ~ 1651 TgCO/year and the total chemical production of CO was 1300 ~ 1579TgCO/year. Those show large ranges because of the large interannual variability of biomass burning CO (direct emission) and biogenic NMHC derived CO (chemical production). Both of the improved CO inventories are also placed within the previously reported estimated value ranges; 1091 ~ 1663 TgCO/year for direct emission and 1461 ~ 1644 TgCO/year for chemical production.

The total CO emission and the individual *a priori* sources are mostly updated by the inversion analysis (this study) within the range of previous source estimates. Hence, isotope information adjusts the each source strength more precisely and accurately while keeping the total CO emission.

6.2 *a posteriori* [CO] and $\delta^{18}O$

In order to see the effect of updated source inventories on the CO concentration and $\delta^{18}O$, the difference between *a posteriori* [CO] and $\delta^{18}O$ and observations are analyzed. The new source inventory is more reliable if, in comparison with the model–observation difference which is based on the *a priori* source information, the difference between *a posteriori* source strengths derived [CO] and $\delta^{18}O$ is reduced.

The model–observation differences of $\delta^{18}O$ are apparently enhanced by more than 50% when the *a posteriori* source strengths are applied (Figure 6.1, Figure 6.3 and Appendix C). Also, the modeled concentration showed better fit to the measurement with the updated source inventory (Figure 6.1). Although, since the forward concentration simulation already reproduced the observations quite well (Figure 5.1), the improvement of *a posteriori* CO concentration is not as clear as *a posteriori* $\delta^{18}O$ (Figure 6.2 and Fig 6.3), the modeled concentrations are around 45% closer to the observations (Fig 6.1). Figure 6.2 shows the *a posteriori* inventory especially improves wintertime modeled [CO]. While the *a posteriori* source emissions are estimated for each year and do not contains seasonality, this implies certain sources are significantly underestimated during the winter. The *a posteriori* $\delta^{18}O$ decreased the overall offset of model-observation difference (Figure 6.3) and the improvement was more noticeable in the Southern Hemisphere (Figure 6.1).

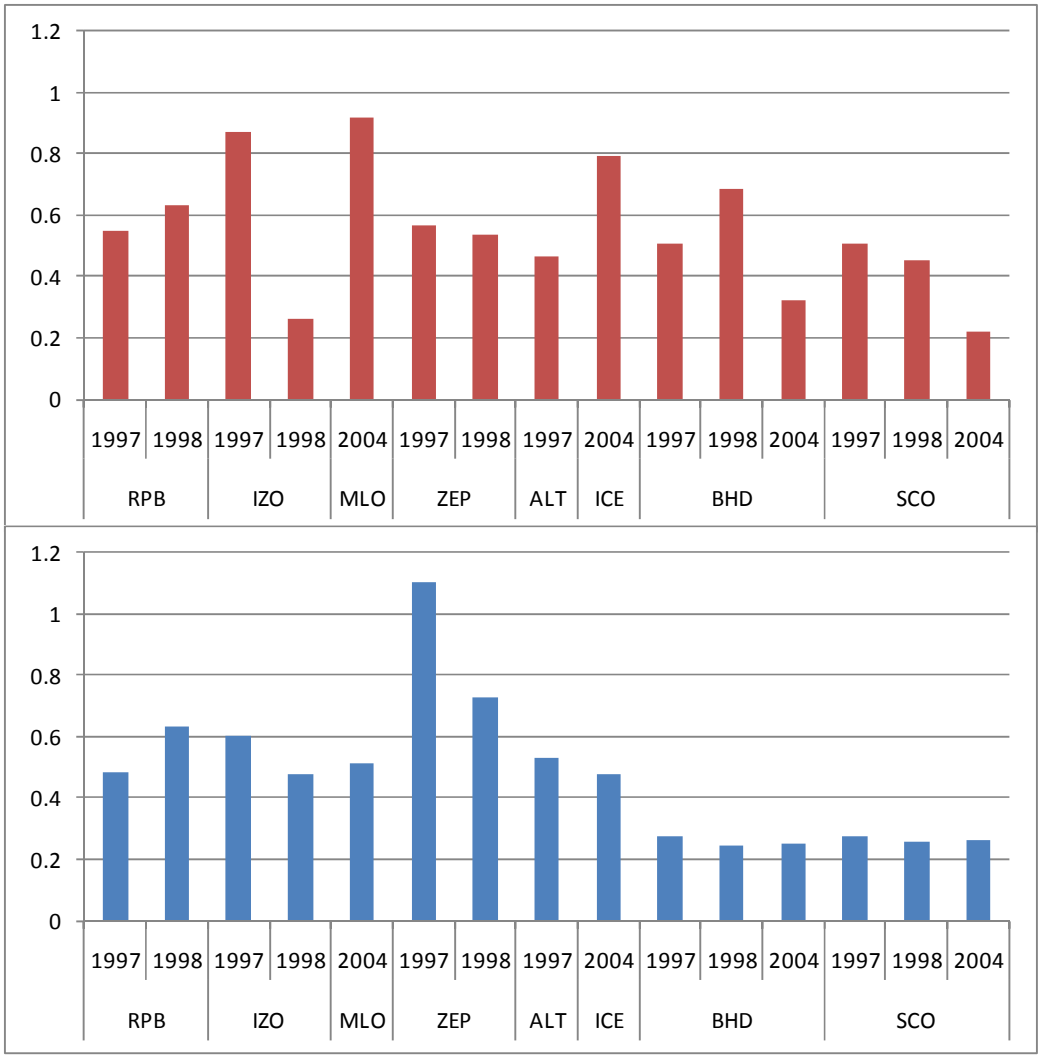

Figure 6.1 The ratio of *a priori* model-observation difference to *a posteriori* model-observation difference for concentration simulation (upper panel) and $\delta^{18}O$ simulation (bottom panel)

In summary, these results indicate that each updated source contributed to improving the both modeled [CO] and $\delta^{18}O$ while there was relatively small adjustment of total CO inventory (Table 6.2). Thus, this suggests that an accurate estimation of source strength distribution is more important than the optimization

of total CO emission in CO inversion analyses. Due to the advantages of including isotope information to the inversion analysis, more realistic source distributions were derived which sufficiently satisfy both measured [CO] and $\delta^{18}O$. Moreover, the improved $\delta^{18}O$ fits provide additional confidence to the inversion results while the [CO]-only inversions can be verified by concentration only.

Figure 6.2 Comparison of *a priori* (brown line) and *a posteriori* (blue line) modeled surface [CO] with measurements (blue dots).

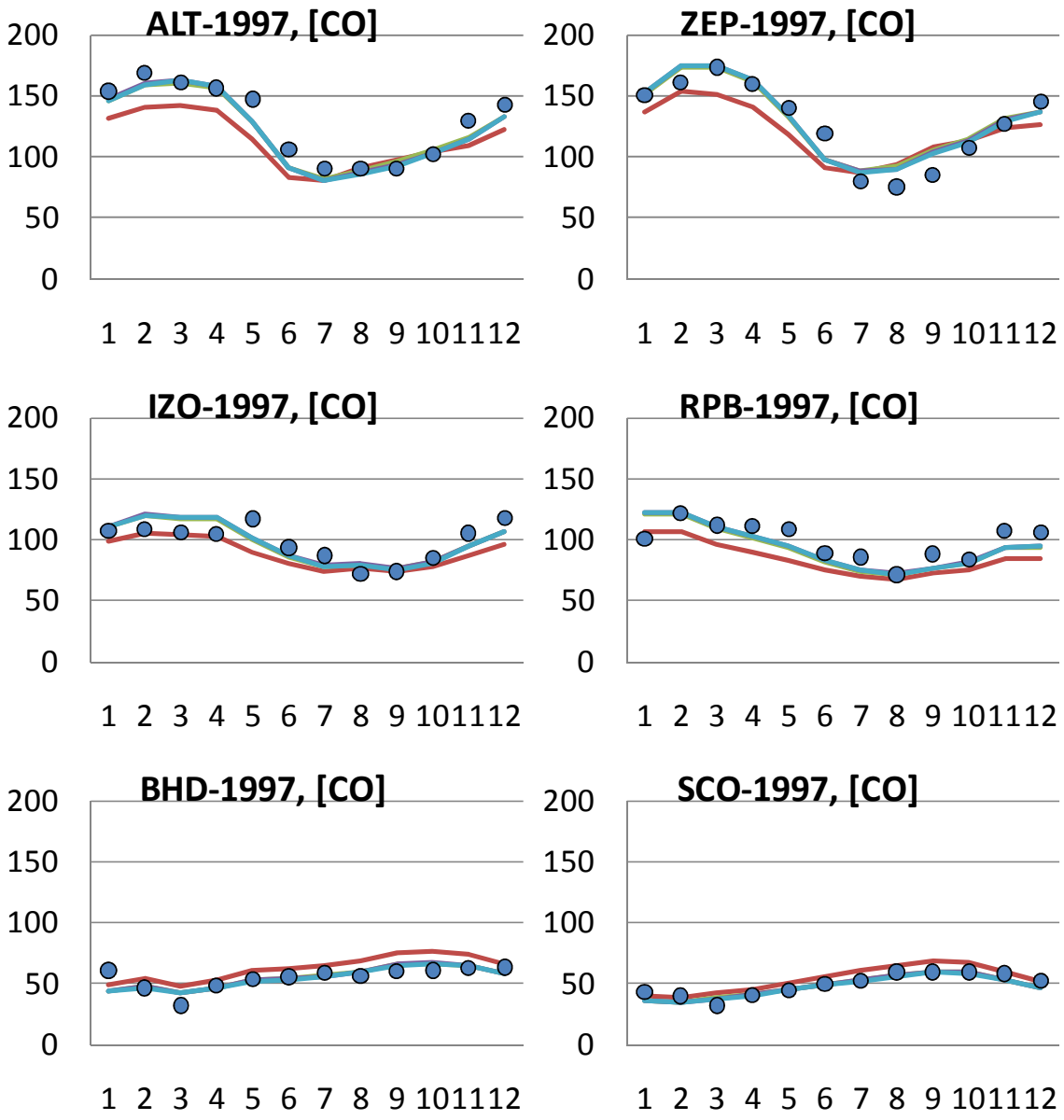

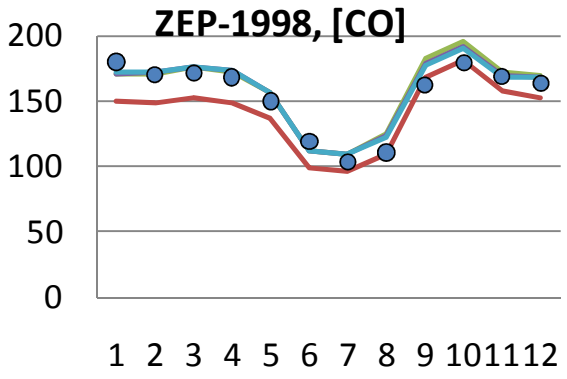
ZEP-1998, [CO]
200
150
100
50
0
1 2 3 4 5 6 7 8 9 10 11 12

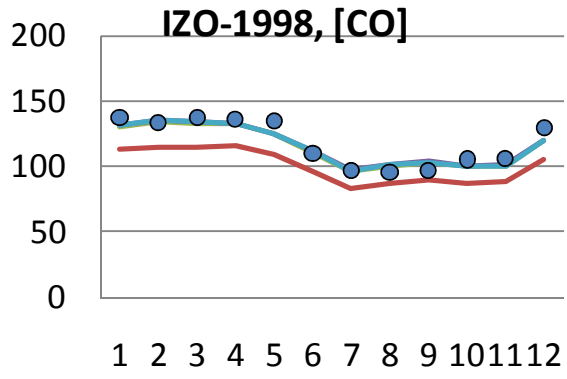
IZO-1998, [CO]
200
150
100
50
0
1 2 3 4 5 6 7 8 9 10 11 12

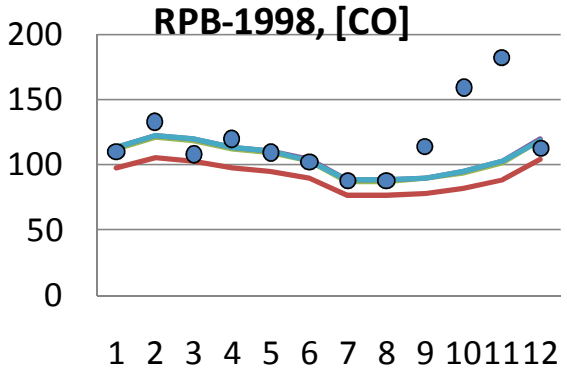
RPB-1998, [CO]
200
150
100
50
0
1 2 3 4 5 6 7 8 9 10 11 12

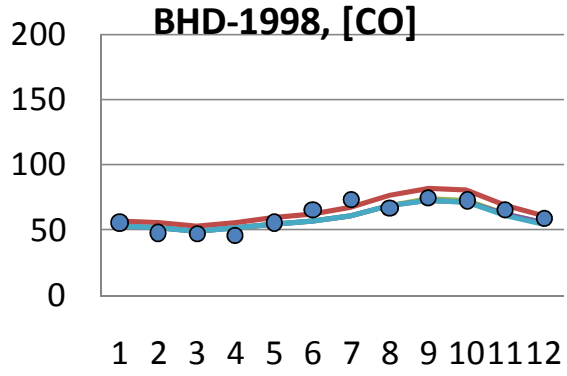
BHD-1998, [CO]
200
150
100
50
0
1 2 3 4 5 6 7 8 9 10 11 12

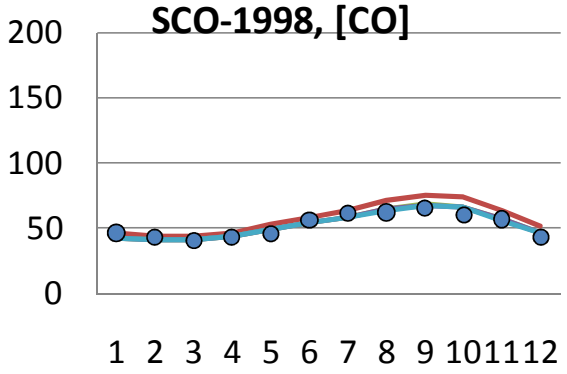
SCO-1998, [CO]
200
150
100
50
0
1 2 3 4 5 6 7 8 9 10 11 12

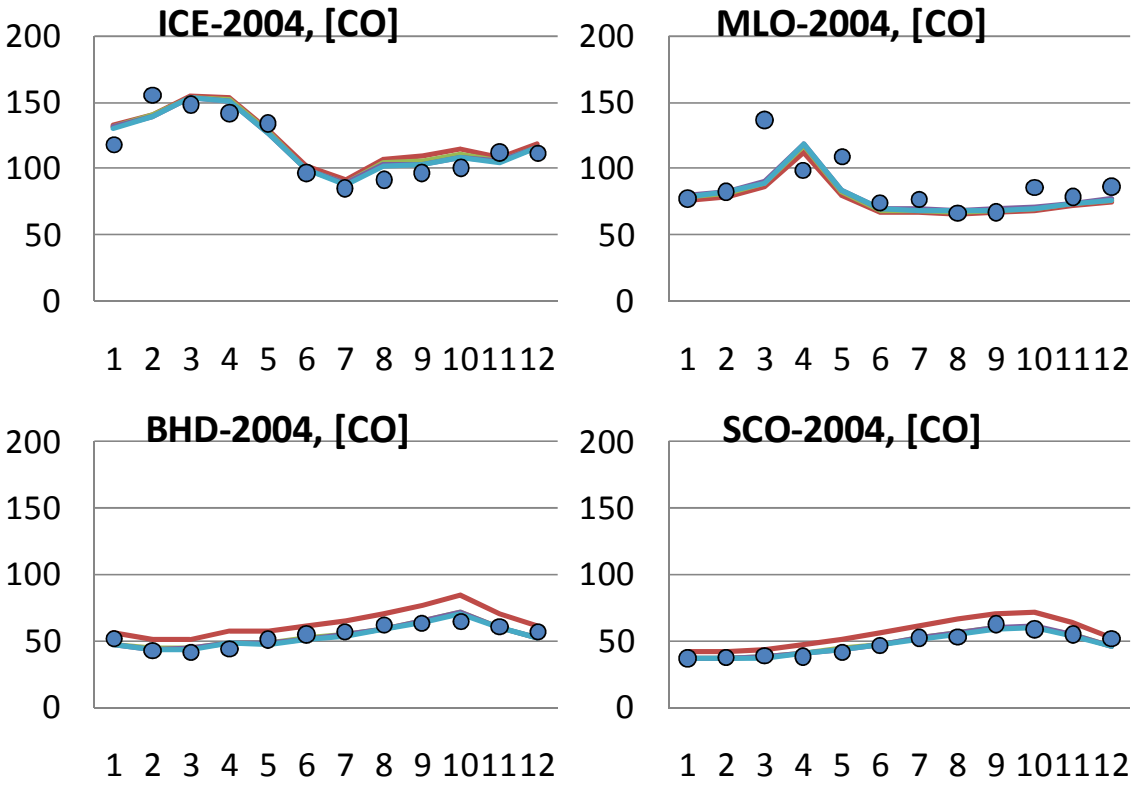
ICE-2004, [CO]
MLO-2004, [CO]
BHD-2004, [CO]
SCO-2004, [CO]
200
150
100
50
0
1 2 3 4 5 6 7 8 9 10 11 12

Figure 6.3 Comparison of *a priori* (brown line) and *a posteriori* modeled surface $\delta^{18}O$ with measurements (blue dots). Green and purple lines denote *a posteriori* $\delta^{18}O$ from simultaneous inversion (adjusted isotope source signature) and sequential inversion (adjusted isotope source signature) respectively. Orange line is *a posteriori* $\delta^{18}O$ with fixed isotope source signature.

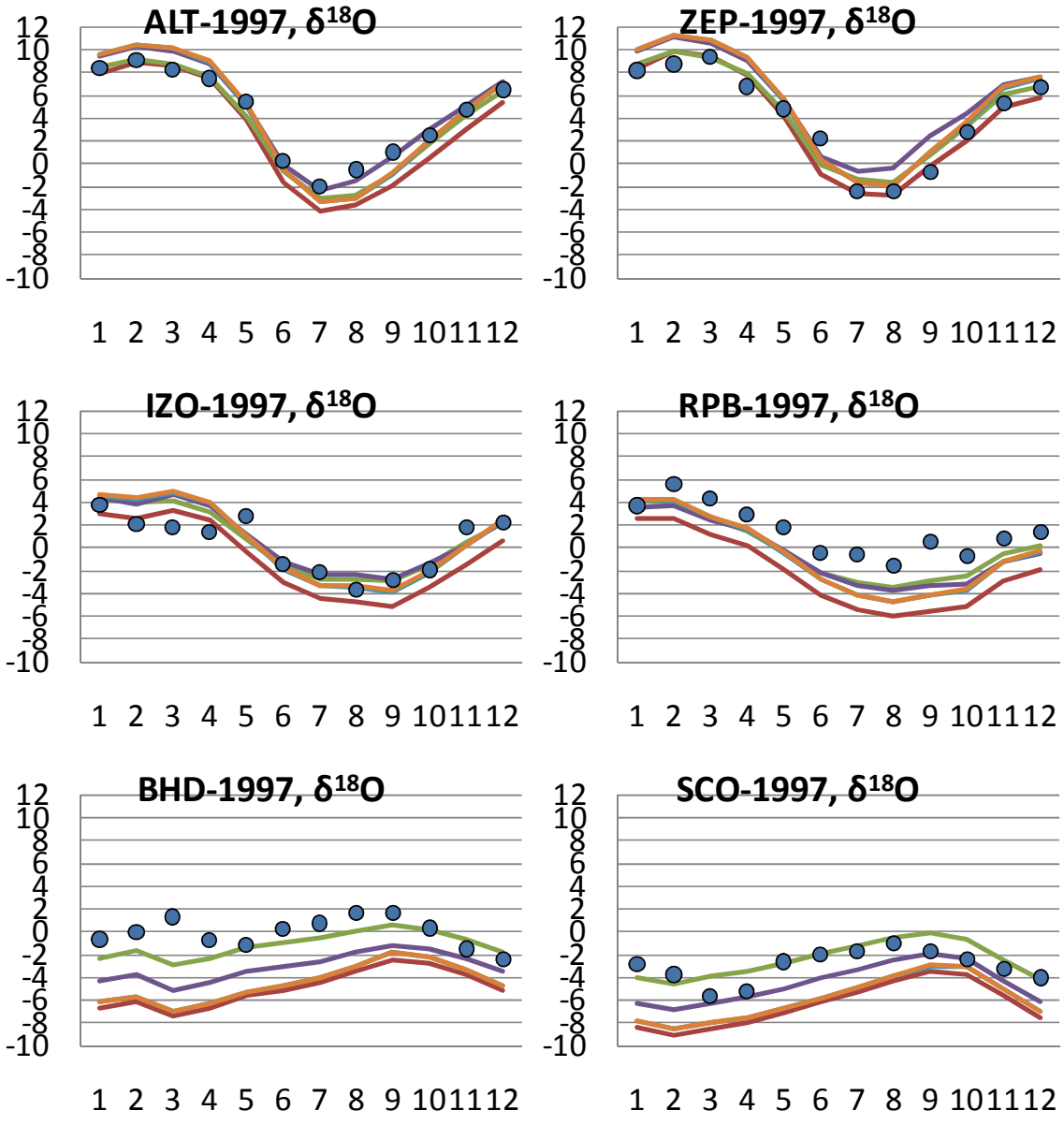

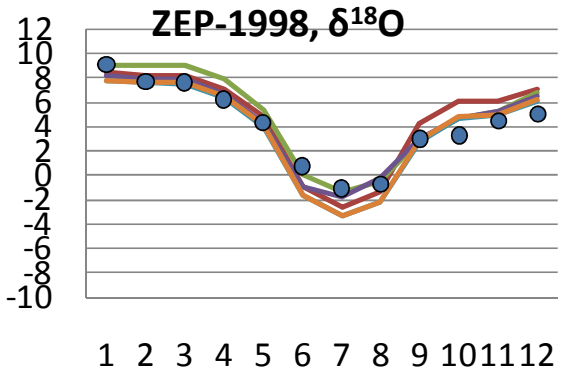
ZEP-1998, δ18O
12 10 8 6 4 2 0 -2 -4 -6 -8 -10
1 2 3 4 5 6 7 8 9 10 11 12

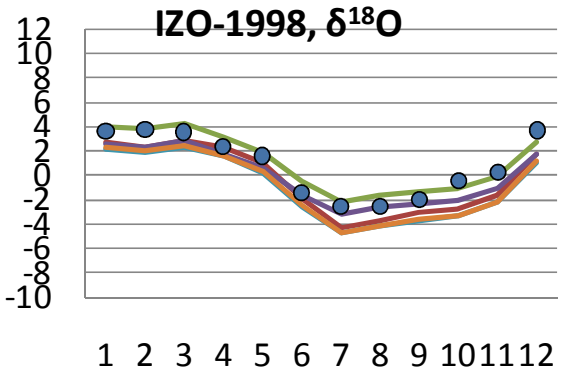
IZO-1998, δ18O
12 10 8 6 4 2 0 -2 -4 -6 -8 -10
1 2 3 4 5 6 7 8 9 10 11 12

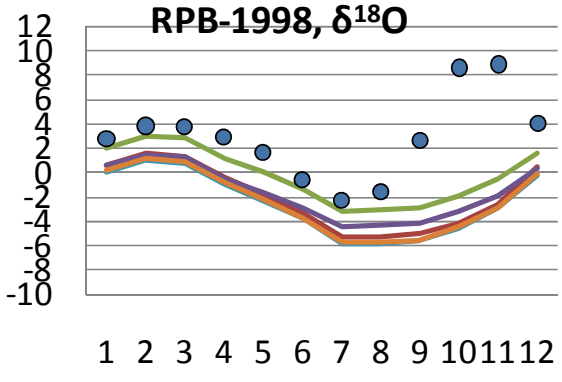
RPB-1998, δ18O
12 10 8 6 4 2 0 -2 -4 -6 -8 -10
1 2 3 4 5 6 7 8 9 10 11 12

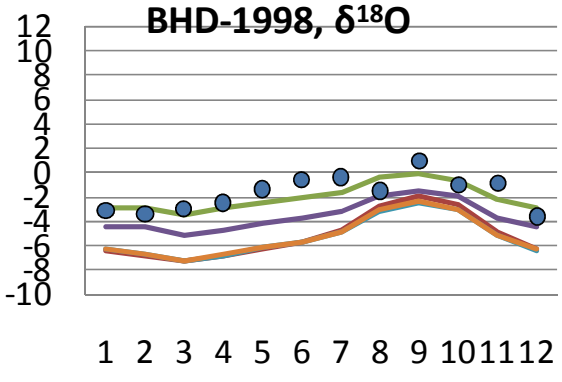
BHD-1998, δ18O
12 10 8 6 4 2 0 -2 -4 -6 -8 -10
1 2 3 4 5 6 7 8 9 10 11 12

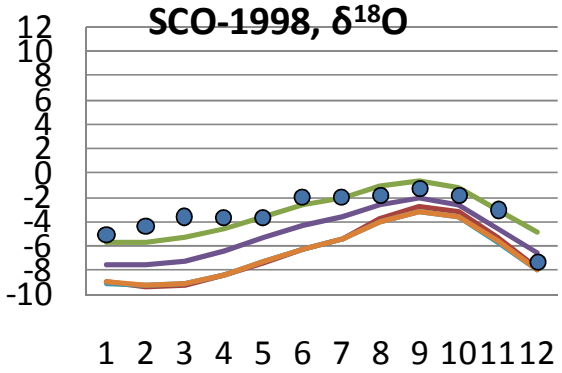
SCO-1998, δ18O
12 10 8 6 4 2 0 -2 -4 -6 -8 -10
1 2 3 4 5 6 7 8 9 10 11 12

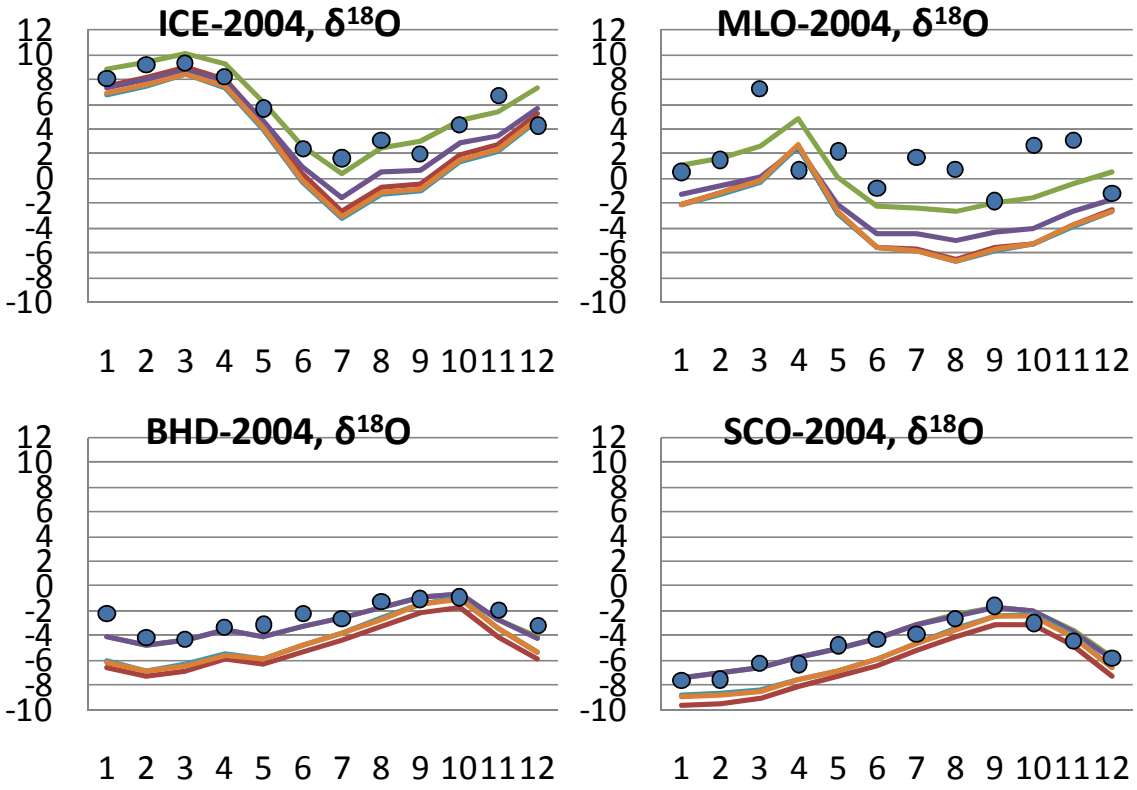

6.3 Interannual source change: NMHC oxidation source

Natural NMHCs are sensitive to climate variations, since the emission flux from vegetation is a function of various factors such as LAI (Leaf Area Index), PPFD (Photo synthetic Photon Flux Density), solar radiation flux, and soil water content. For example, [Müller et al., 2008] shows that global isoprene emission was enhanced 13% during the 97-98 El Niño event and found 20% variations in their simulation periods (1995~2006).

Despite the increasing importance of NMHCs in atmospheric chemistry and climate change [Shindell et al., 2007; Shindell et al., 2008], the short lifetime of NMHCs (minutes to days) makes it difficult to study extensively and their measurements are limited. NMHCs react with atmospheric oxidants such as hydroxyl radicals and are oxidized to carbon monoxide, whose lifetime is relatively long (2~3 months in global average) compared to NMHCs. Thus, non-methane hydrocarbon derived CO can be used as a good proxy of the global NMHCs flux.

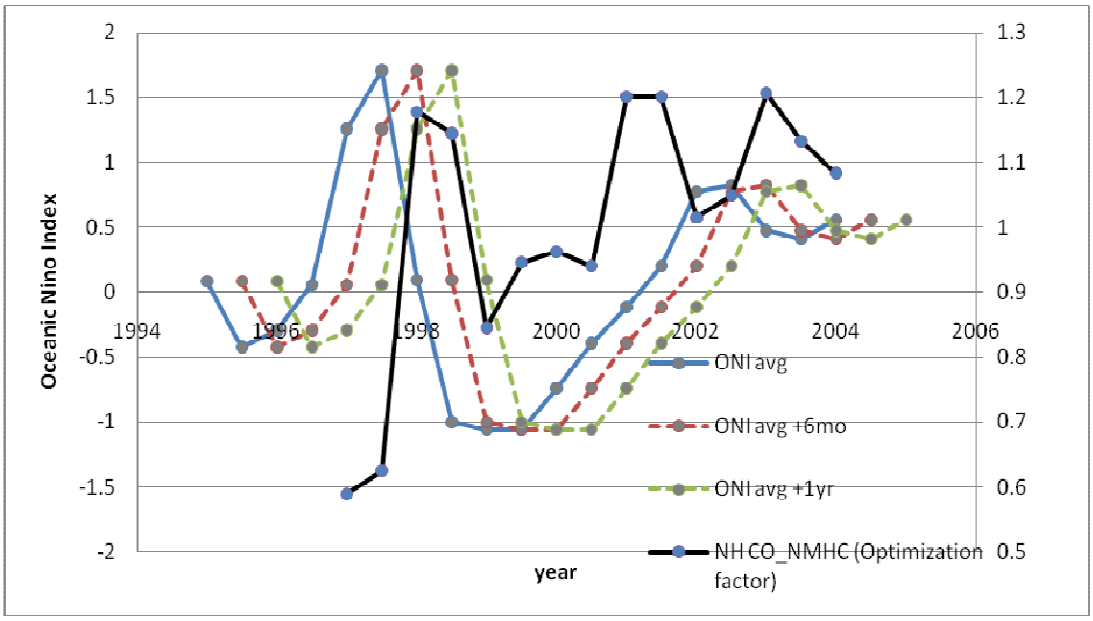

Figure 6.4 Comparison of Oceanic Nino Index (blue line) and optimization factor of NMHC oxidation source (black line). Dotted lines are 6 month (brown) and 12 month (green) offset of Oceanic Nino Index.

NMHCs are known to be one of the major sources of tropospheric CO

[Bergamaschi et al., 2000a; Müller and Stavrakou, 2005; Duncan et al., 2007] and isoprene is responsible for about 75% of VOC-derived CO and approximately 13% of the total CO [Pfister et al., 2008a; Pacifico et al., 2009]. Since each carbon in isoprene (C_5H_8) yields 0.2 ~ 0.4 CO [Miyoshi et al., 1999; Bergamaschi et al., 2000b; Granier et al., 2000; Duncan et al., 2007; Pfister et al., 2008a], one mole of isoprene produces 1 ~ 2 mole of CO and it is the most dominant species of the NMHCs [Pfister et al., 2008a]. Therefore, CO from NMHC oxidations is primarily affected by isoprene emission change.

Since NMHC-derived CO is tagged in the model simulation, interannual variation of this source could be quantitatively evaluated. Bayesian synthesis inversion technique is applied to constrain the NMHC oxidation source of CO for 8 years (1997 ~ 2004). The inversion scheme is basically same as described in chapter 4, but only [CO] measurements are used in this analysis. Observational data are taken from the 11 Northern Hemisphere NOAA GMD global monitoring stations (Table 6.3) which represent global background air. Hence, the NMHC oxidation source is constrained for the NH. The inversion analysis was performed for every 6 months interval with 1 year observations estimating 1 year's source inventory (ex. Jan. 1997 to Dec. 1997, Jul 1997 to Jun 1998, Jan. 1998 to Dec. 1998, … and Jan 2004 to Dec 2004). [CO]-$\delta^{18}O$ joint inversion results (chapter 6.1) were available for 1997, 1998 and 2004 and these are consistent with the NOAA GMD [CO]-only inversion results and thus added more confidence to the

results (Figure 6.6).

Table 6.3 NOAA GMD sites used in this study

Station	Code	Latitude	Longitude	Altitude (m)
Spitsbergen	zep	78.90	11.88	475
Barrow	brw	71.32	-156.61	11
OceanStationM	stm	66.00	2.00	0
NiwotRidge	nwr	40.05	-105.58	3523
Utah	uta	39.90	-113.72	1320
Bermuda	bmw	32.27	-64.88	30
Izana	izo	28.31	-16.50	2360
KeyBiscayne	key	25.67	-80.16	3
Assekrem	ask	23.18	5.42	2728
Guam	gmi	13.43	144.78	1
Barbados	rpb	13.17	-59.43	45

Previously, high isoprene emissions during the El Niño events and low isoprene emissions during the La Niña events are reported from several modeling studies [Naik et al., 2004; Lathière et al., 2006; Müller et al., 2008]. Since isoprene is a dominant species of NMHC oxidation source, to explain the interannual variation of *a posteriori* NMHC oxidation source, it has been plotted together with ONI (Oceanic Niño Index, NOAA) [Smith et al., 2008]. The inversion result is showed in Figure 6.4. The black lines are optimization factors of CO from NMHC oxidation and the blue line is ONI. The dashed red and dashed green lines are 6 months and 1 year offset of the blue line; ONI. There is a

good agreement between 6 or 12 months offset ONI and optimized NMHC derived CO inventory. [Müller et al., 2008] also pointed out there is a positive correlation between 6 months delayed ONI and modeled global isoprene flux. Therefore the response by vegetation can be delayed at least 6 months from the center of the ENSO. During the positive phase of the ENSO (El Niño) periods (1997-1998 and 2002-2003) the NMHC-derived CO increased rapidly while the optimization factors are close to unity during the La Nina and normal phase.

In 2001, the inversion result corrected *a priori* NMHC-derived CO flux to increase 20% while 2001 was not only a non-El Nino year but also just after the long La Nina years (1998 – 2000). Thus, it was hard to expect the enhanced NMHC emission in that year. However, 2001 was one of the warmest years in past 100 years [Hansen et al., 2002; Hansen et al., 2006] and found a close relationship between global surface temperature [Hansen et al., 1996; Hansen et al., 2006] (http://data.giss.nasa.gov/gistemp/) and NMHCs source strength of CO (Figure 6.5). Since anthropogenic greenhouse gases are suspected for the 2001's record high global surface temperature [Hansen et al., 2002], this implies that natural NMHCs emissions are affected by both human activities and natural climate oscillations.

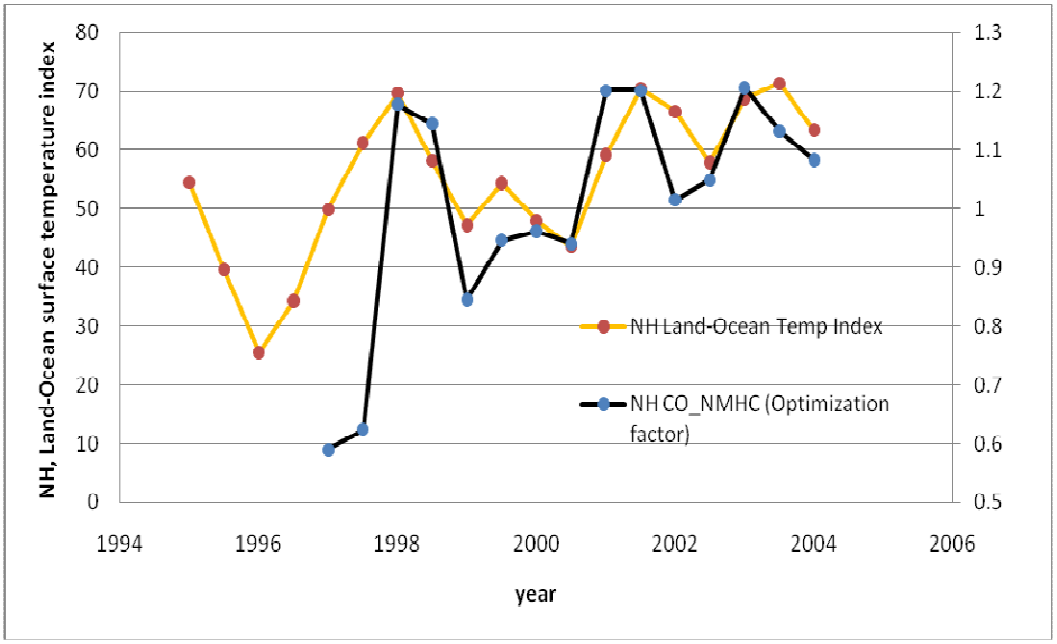

Figure 6.5 Comparison of Northern Hemisphere Land-Ocean surface temperature index (orange line) with optimization factor of NMHC oxidation source (black line).

NMHC oxidation source showed stronger correlation with the NH surface temperature (r=0.57, 1997~2004) than with 12 months offset ONI (r=0.34, 1997~2004; r=0.52, excluding 2001 data). In addition, NMHC source is instantly influenced by the change of surface temperature. The impact of an ENSO event on NMHC emission from vegetation was detected approximately after six months (Figure 6.4). This temporal delay may be considered to be the time that it takes for the observed oceanic ENSO change to affect terrestrial climate factors including surface temperature. Therefore, since the other climate factors which are not closely related to ENSO can also affect the NMHC fluxes during the plant's

response time, comparing with land-ocean temperature index [Hansen et al., 1996; Smith et al., 1996], the ONI-NMHC source change connection is relatively indirect and noisy like 2001's inversion result.

In summary, the interannual variation of NMHC emission was closely linked with ENSO and the global surface temperature. While the NMHCs fluxes are more sensitively correlated with the temperature change, ONI proceeded 6 to 12 months from the actual emission change.

The interannual variability of the Northern hemisphere NMHC oxidation source in the 1997 ~ 2004 period was up to 100% (Figure 6.4). Since there was both strong El Niño and La Niña occurred during the time period, this may be close to the maximum interannual variability of the source. [Müller et al., 2008] estimated the maximum interannual variability of global isoprene emission in the 1995–2006 as 20% and 16% during the 1997-2004 same as our inversion analysis period, while our top-down estimation of the Northern Hemispheric NMHC source strengths of CO varied ±52% from the mean value which is remarkably bigger than the modeled isoprene study result. However, the increase is reduced when *a posteriori* Southern Hemispheric NMHC source is included for the global scale analysis. In 1997 and 1998, since a strong La Niña was followed by a strong El Niño, the effect of ENSO on the global NMHCs flux change could be seen easily. During the extreme ENSO period, the result of the NH and the SH [CO]-$\delta^{18}O$ joint inversion is shown in Figure 6.7. The source optimization results

suggest that from 1997 to 1998 in the Northern Hemisphere NMHC source increased 106% and in the Southern Hemisphere it increased only 27%. Although the Northern Hemisphere has greater land coverage than the Southern Hemisphere, isoprene emission from the Southern Hemisphere is 1.2 to 1.6 times higher [Pfister et al., 2008a]. *A priori* NMHC-derived source was 232 TgCO/year from the SH and 310 TgCO/year production from the NH. Therefore, the global NMHC emission change was 74% and the error analysis was ±13% uncertainty.

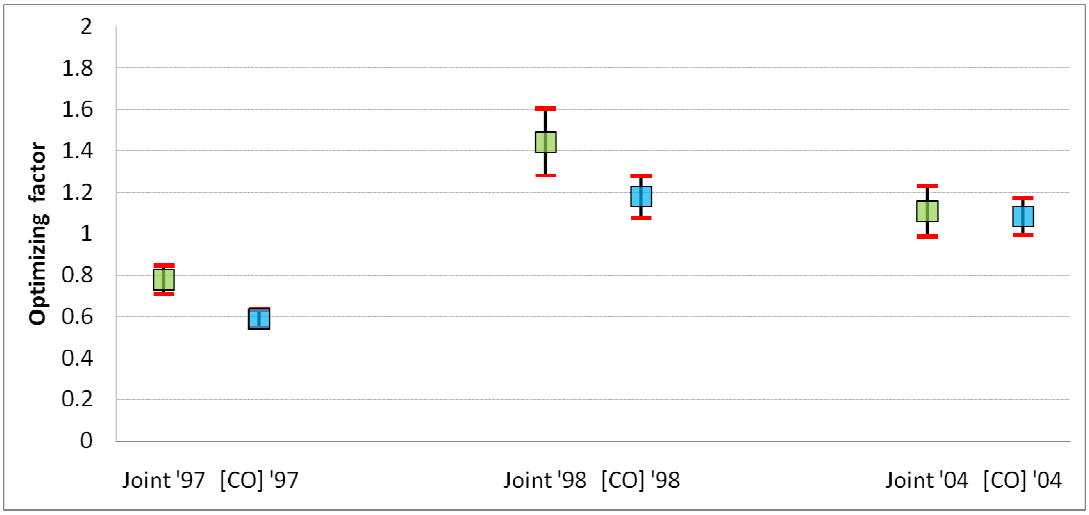

Figure 6.6 Comparison of *a posteriori* the Northern Hemisphere NMHC oxidation source of CO calculated from [CO]-$\delta^{18}O$ joint inversion (green squares) and NOAA GMD [CO] inversion (blue squares). Error bar is *a posteriori* uncertainty.

The inversion result indicated the response of the Southern Hemisphere is relatively insensitive to the effect of ENSO. [Guenther et al., 1995] shows that in the Northern Hemisphere 65% of the NMHCs are produced in between the

equator and 25˚N and in the Southern Hemisphere 90% of the emission occur in between the equator and 25˚S. This implies the effect of ENSO and surface temperature change to the vegetation is significant in the Northern Hemisphere. Plus, because of the small contribution of the anthropogenic sources and low concentration of total CO in the Southern Hemisphere, the relative impact of ENSO to total CO concentration will be comparable in both hemispheres.

Since the majority of biogenic NMHC source of CO is from isoprene oxidation, this interannual variation of *a posteriori* NMHC oxidation source is sufficient to confirm the previous studies found that strengthened NMHCs or isoprene emissions during the positive ENSO phase [Guenther et al., 1995; Lathière et al., 2006; Müller et al., 2008] as well as direct to amplify the previous magnitude of interannual natural NMHCs flux change estimates.

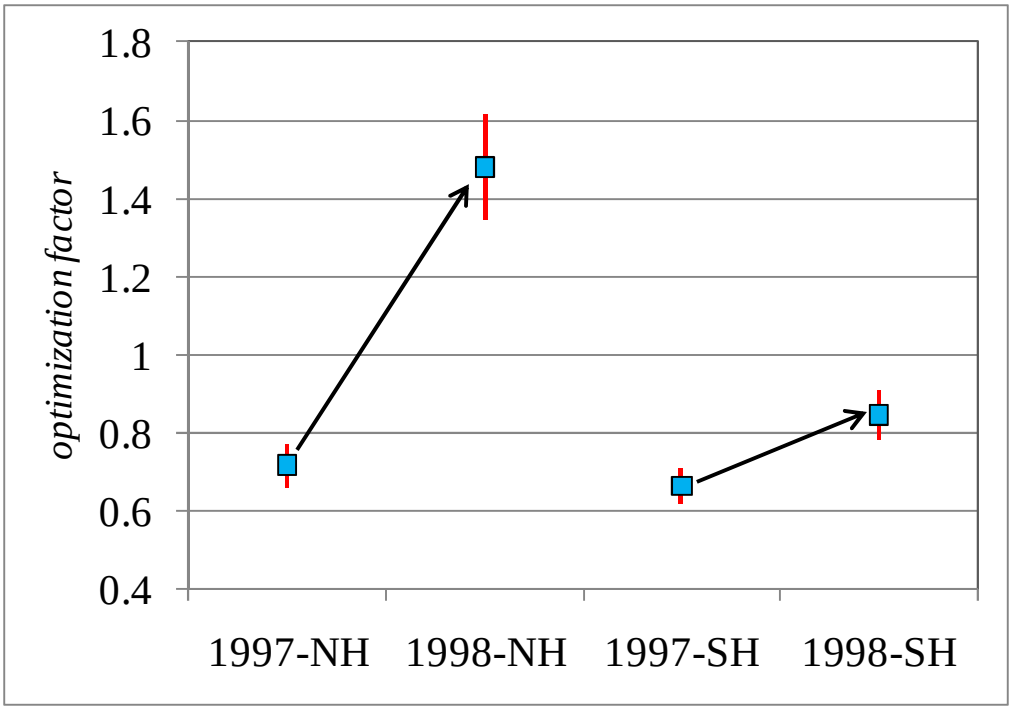

Figure 6.7 Optimization factors of NMHC oxidation source of CO calculated from the joint inversion analysis.

6.4 Inversion results by different inversion schemes: [CO]-only, sequential, and simultaneous inversion

Various inversion schemes are tested and discussed in this section to elucidate the influence of different isotope information combining methods on the *a posteriori* source strength estimates.

Joint application of isotope ratio and concentration measurements generally gives more robust inversion result since the isotope ratios provides additional constraint. In Figure 6.8, *a posteriori* uncertainties of the three different

inversion methods are presented. The sequential inversion provided the smallest uncertainties and always the biggest uncertainty was found in the [CO]-only inversion. The effect of different inversion methods is clearly shown in the biomass burning, NMHC oxidation and the Northern Hemisphere biofuel source because due to the small concentration of the minor source biogenic and ocean sources are loosely constrained and the smaller *a priori* source uncertainties of fossil fuel and methane oxidation limit the influence of each inversion method. In the sequential inversion, the inverted data sets and the obtained uncertainties from the first inversion step are used as initial values for the second inversion (Eqn. 4.9). The final uncertainties (error covariance, $\hat{\boldsymbol{S}}$; Eqn. 4.3) of each source strength from the sequential inversion is obtained from the intermediate *a posteriori* source uncertainty term which is already once reduced using $C^{16}O$ information while the joint simultaneous inversion constrains the source only once.

A basic underlying assumption of the Bayesian synthesis inversion is linear relation between the source strengths and measurements. If the relation is nonlinear, the inversion should be iterated until reaching a converged value. The linearity can be verified by comparing the result of sequential and simultaneous inversion. If the results are different, this implies at least one of the measurement data sets is not linear with source change. Since the *a posteriori* source strengths from the two different methods are very similar in this study (approximately ±2%

in average; Table 6.4), [$C^{16}O$] and [$C^{18}O$] hold linearity from source strengths change.

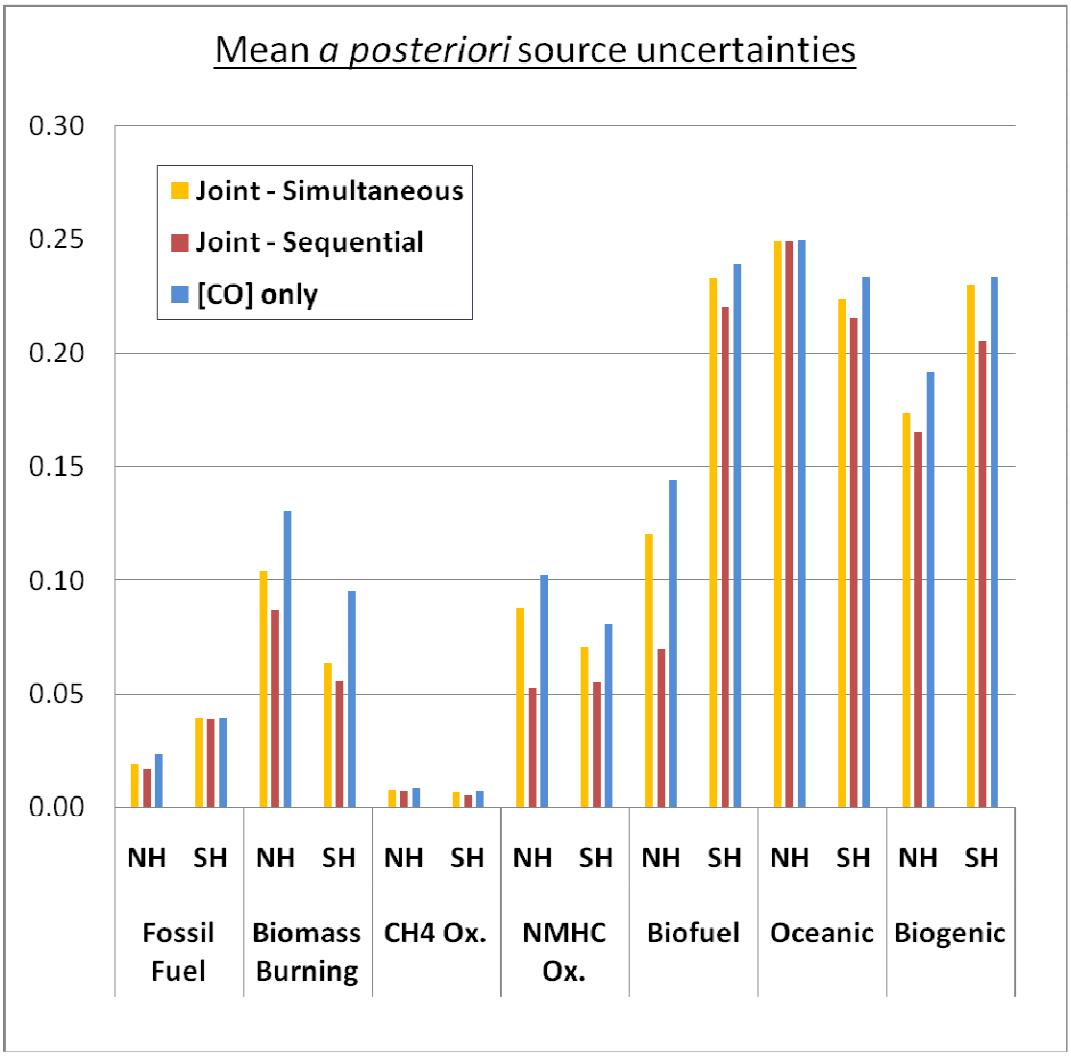

Figure 6.8 Comparison of a posteriori uncertainty of three different inversion schemes: [CO]-only, sequential and simultaneous inversion.

While the sequential and simultaneous inversions are clearly improve the

modeled $\delta^{18}O$ and estimated very similar *a posteriori* source strengths, the simultaneous inversion shows better fit to the observed $\delta^{18}O$ (Figure 6.3). The averaged differences to the observation were derived to be 1.3‰ and 1.9‰ for simultaneous inversion and sequential inversion respectively.

Table 6.4 The ratios of optimization factors. *seq/sim* is ratio of optimization factor of sequential inversion to that of simultaneous inversion and *[CO]/sim* is ratio of optimization factor of [CO]-only inversion to that of simultaneous inversion. Mean deviation from the unity (identical result) is ±1.7% for *seq/sim* and ±4.6% for *[CO]/sim*.

		Fossil Fuel	Bio. Burn.	CH4 Ox.	NMHC Ox.	Biofuel	Oceanic	Biogenic
1997NH	*seq/sim*	0.99	0.98	0.99	0.98	1.04	0.99	1.00
	[CO]/sim	1.01	0.99	0.96	1.14	0.92	0.98	1.17
1998NH	*seq/sim*	1.00	1.00	1.00	0.97	1.03	1.00	1.00
	[CO]/sim	1.05	1.07	0.97	0.97	0.91	0.98	1.15
2004NH	*seq/sim*	1.00	1.00	1.00	0.94	1.00	0.99	1.18
	[CO]/sim	1.05	1.06	0.96	0.96	0.94	1.00	1.38
1997SH	*seq/sim*	1.00	0.99	0.99	0.98	1.00	0.99	1.00
	[CO]/sim	1.01	0.97	1.00	0.99	1.04	1.00	1.07
1998SH	*seq/sim*	1.00	1.01	1.00	0.97	0.99	0.99	0.99
	[CO]/sim	1.00	1.04	1.00	0.98	0.98	1.00	0.98
2004SH	*seq/sim*	0.99	0.98	0.99	1.02	0.98	0.98	0.97
	[CO]/sim	1.00	0.98	0.99	1.05	0.99	0.98	1.03

In sum, insignificant *a posteriori* source inventory differences, especially between the joint sequential and joint simultaneous inversion, were found in the results of the three inversion schemes: [CO]-only, sequential and simultaneous inversion (Table 6.4). However, when [CO] and $\delta^{18}O$ are jointly used in the

inversion analyses, the optimized source strengths and $\delta^{18}O$ were reliable then the [CO]-only inversion results. The sequential use of the concentration and isotope information tend reduce the *a posteriori* uncertainties more effectively (precision) and the simultaneous use of them showed smaller model-observation difference (accuracy).

6.5 Comparison of the NOAA GMD [CO] inversion with [CO]+$\delta^{18}O$ inversion

In order to see the influence of number of observation stations and constituency of the inversion result with using different observational data sets, the sources of NH carbon monoxide are constrained with 11 NOAA GMD [CO] measurements. Inversion procedure is the same as inversion method described in chapter 6.3.

NOAA GMD [CO] inversion results are very similar to this study's inversion results: Joint inversion of [CO] and $\delta^{18}O$ and [CO]-only inversion (Figure 6.9). For the biofuel and biogenic source, although each method estimated notably different optimization factors, the discrepancies are within the uncertainty ranges.

Difference between *a posteriori* concentrations of each inversion result and measured concentrations are compared in Figure 6.10. Similar extent of

improvement from the *a priori* model-observation difference is found.

Therefore, consistency of *a posteriori* source strengths and model-observation difference between the GMD [CO] inversion and joint inversion results indicate that inversion results are sufficiently constrained despite the limited number of the observations.

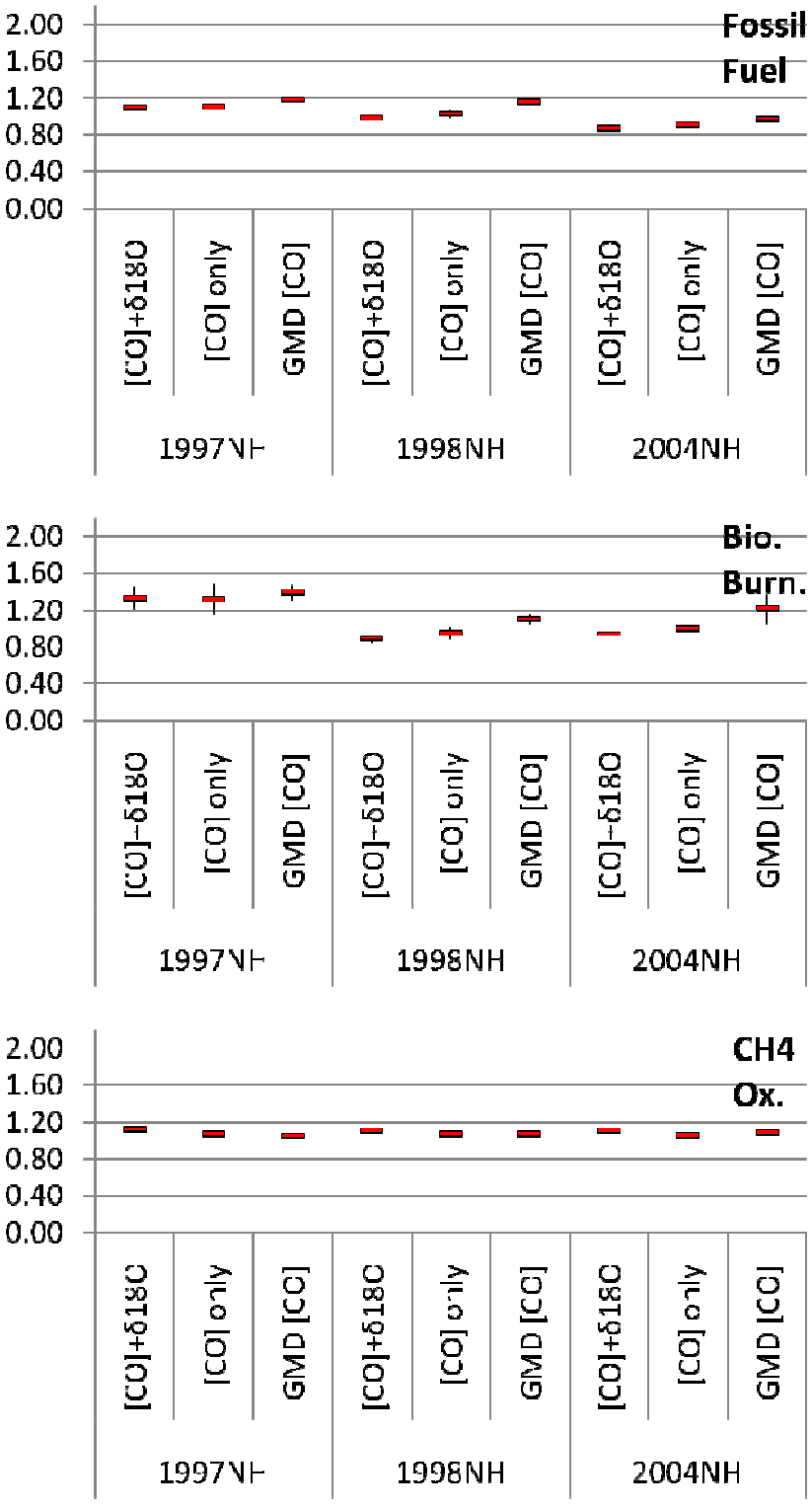
Fossil Fuel
Bio. Burn.
CH4 Ox.
2.00
1.60
1.20
0.80
0.40
0.00
[CO]+δ18O
[CO] only
GMD [CO]
1997NH
1998NH
2004NH

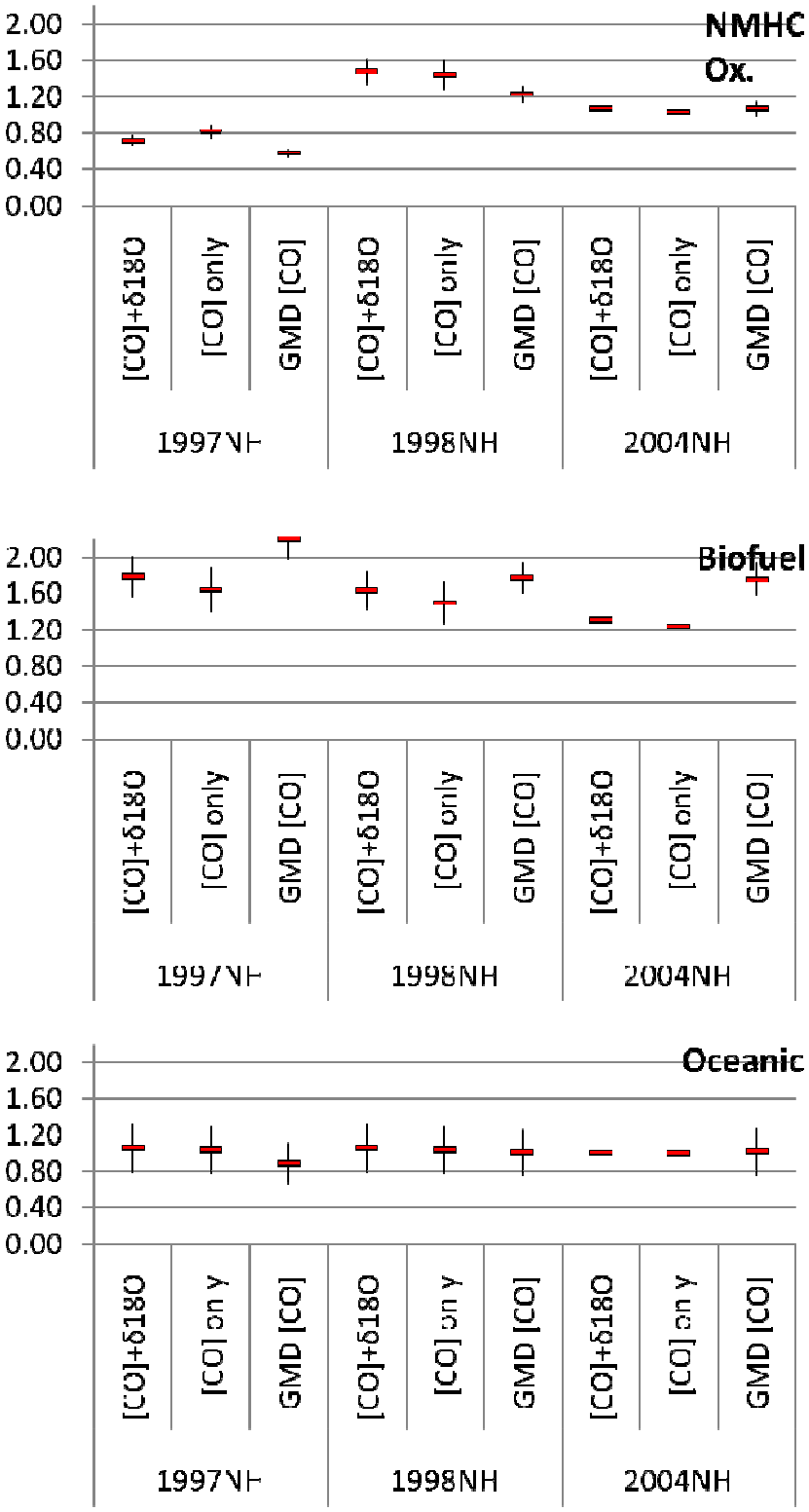
NMHC Ox.
2.00
1.60
1.20
0.80
0.40
0.00
[CO]+δ18O
[CO] only
GMD [CO]
1997NH
1998NH
2004NH
Biofuel
Oceanic

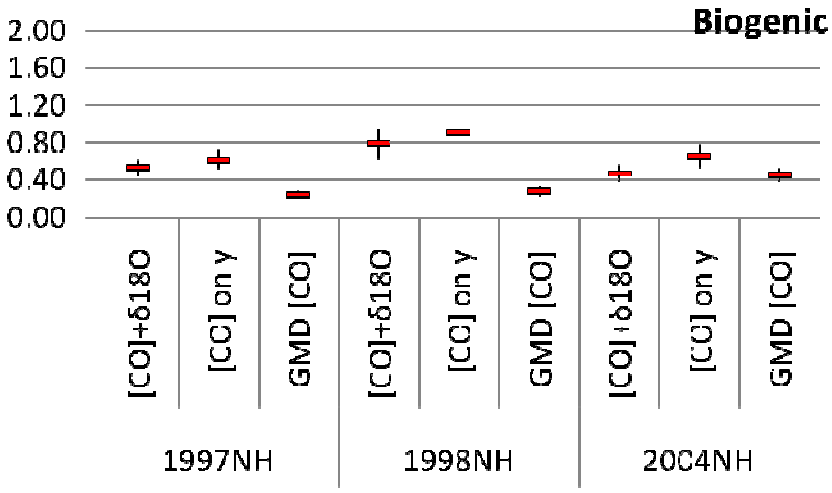

Figure 6.9 Comparison of optimization factors calculated from joint simultaneous inversion ([CO]+δ^{18}O), [CO]-only inversion and [CO]-only inversion using NOAA GMD [CO] (GMD[CO]).

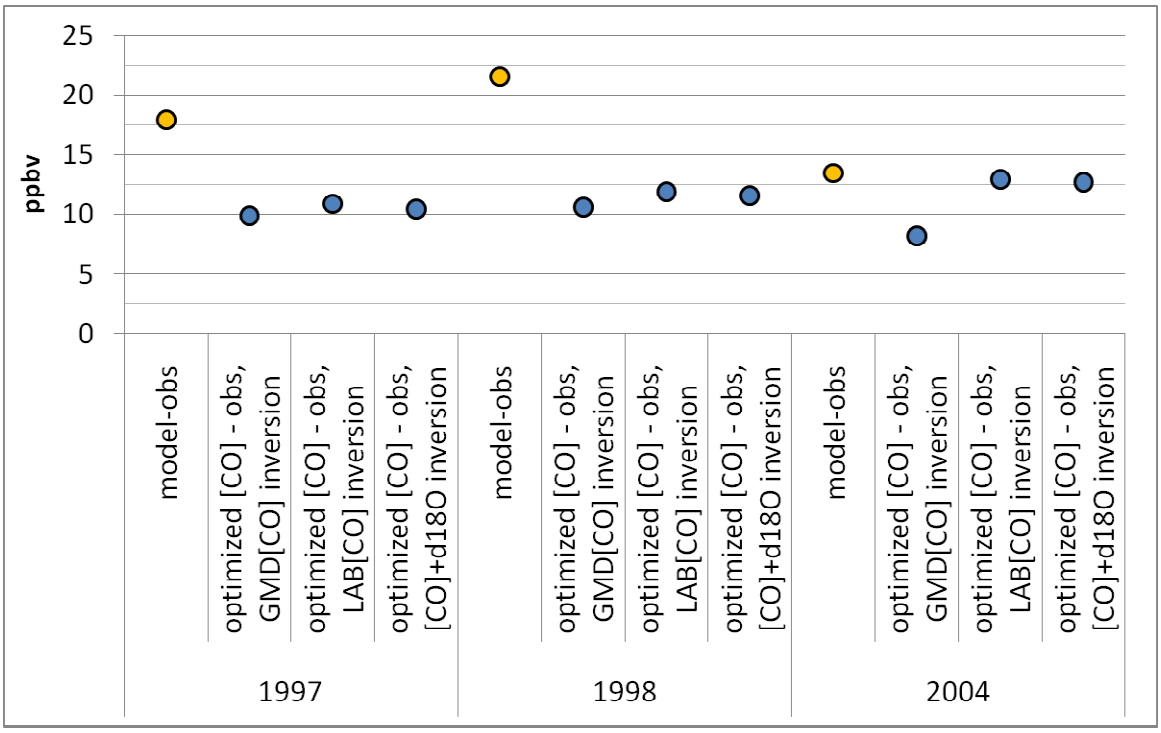

Figure 6.10 Comparison of model (*a priori* (orange dots) and *a posteriori* (blue dots)) – observation difference of the Northern Hemisphere.

6.6 Optimized $\delta^{18}O$ values of individual sources

A posteriori isotope source signatures of CO sources are shown in Table 6.5. Since the decoupled inversion (chapter 4.4.1) independently optimizes the $C^{16}O$ and $C^{18}O$ inventories, $\delta^{18}O$ source signature was optimized from this relation:

$$\hat{\delta}^{18}O_{source} = \left(\frac{\hat{x}_{C^{18}O}}{\hat{x}_{C^{16}O} / R_{standard}} - 1 \right) \times 1000 . \qquad \text{(Eqn. 6.2)}$$

The results are taken from the second iteration of the inversion and thresholds described in chapter 4.4.4 are applied.

Table 6.5 *a priori* and *a posteriori* isotope source signatures of CO sources

	Fossil fuel	Biomass burning	CH4 ox.	NMHC ox.	Biofuel	Ocean	Biogenic
97NH	21.5	18.2	2.9	1.3	14.7	18.2	-0.4
98NH	21.5	14.1	2.4	5.0	22.5	17.5	-1.5
04NH	21.5	12.5	2.5	5.0	15.4	16.0	5.0
97SH	23.5	12.5	3.0	5.0	18.1	20.0	5.0
98SH	23.8	12.5	2.2	5.0	18.5	19.2	4.5
04SH	23.2	12.5	0.9	5.0	16.2	17.7	2.7
a priori	23.5	17.5	0.0	0.0	17.5	15.0	0.0

The optimized $\delta^{18}O$ signature from fossil fuel combustion in the NH was 21.5‰ and it is lighter than the *a priori* source signature (23.5‰) while that in the SH adjusted less than 0.3‰. The inversion analysis consistently suggested significantly lighter oxygen isotope source signature compared to the *a priori* $\delta^{18}O$ signature excluding the 1997 NH result. Also, *a posteriori* methane oxidation and NMHC oxidation isotope source signatures are heavier than the *a priori* estimates (0‰). This result agrees with the Keeling plot result shown in Figure 5.11. A lighter $\delta^{18}O$ signature from biomass burning was derived from heavier $\delta^{18}O$ signatures from the oxidation sources. *A posteriori* ocean source signature was heavier than the *a priori* $\delta^{18}O$. The estimated $\delta^{18}O$ from biofuel use and biogenic emission were different to each inversion period.

7. Summary and Concluding Remarks

The simulation results of MOZART-4 reproduced the observations fairly well in both [CO] and $\delta^{18}O$. The modeled and measured concentration showed a strong correlation (ρ = 0.94) and the mean model-observation difference was 10.5ppbv. In general, the model underestimated the measurements in NH and overestimated in SH. For $\delta^{18}O$, the correlation between the model and observation was 0.86 and the mean model-observation difference was 3‰. The model accurately reproduced observed $\delta^{18}O$ at high latitude stations while modeled $\delta^{18}O$ was lighter than observations at mid- and low latitude stations. Also, the χ_{red}^2 of the forward model run for [CO] was 0.65 and of $\delta^{18}O$ was 2.29 confirming model successfully explained the most of observational data points.

Although 17.5‰ was applied for the $\delta^{18}O$ signature from biomass burning in the forward model, a wide range of the source signature has been estimated from the previous studies. The Keeling plot method and the sensitivity of modeled $\delta^{18}O$ with various $\delta^{18}O$ signatures from biomass burning were used to estimate the $\delta^{18}O$ from biomass burning. The Keeling plot approach estimated 21‰ and the sensitivity test suggested 20‰ for the oxygen isotope source signature of biomass burning. These are significantly heavier than the previously reported $\delta^{18}O$ from the biomass burning: 16 ~ 18‰.

The joint inversion of [CO] and $\delta^{18}O$ estimated total global CO production at 2951TgCO/yr, 3084TgCO/yr and 2583TgCO/yr for 1997, 1998 and 2004 respectively. The *a posteriori* fossil fuel combustion source changed less than 5% in the SH and adjusted ±15% in the NH. The inversion result showed that *a priori* biofuel inventory is significantly underestimated in the NH (up to 80%). Since GFED-v2 inventory was used for the biomass burning source strength, the *a posteriori* source did not change much however, in 1997, the inversion analysis increases 33% of the *a priori* source in the NH. The inversion result indicated a significant current overestimation of direct biogenic emission source (up to 50% in the NH). The methane oxidation source is considered to be a well-known source because of its relatively well known chemistry and long life time of methane. Thus, *a posteriori* source strength is similar to the *a priori* source strength. In the NH, ~10% more methane-derived CO was estimated and ~3% less methane-derived CO was estimated in the SH. A strong interannual variation of NMHC-derived CO was found in this study. A strong La Niña was followed by a strong El Niño during the 1997 and 1998. NMHC-derived CO production was doubled in that period in the NH. Also, an 8-year-consecutive inversion analysis was performed using NOAA GMD [CO] and this confirmed the strong interannual variation of NMHC oxidation source of CO and showed a good correlation with the ONI and global surface temperature change.

The updated CO budget improved modeled concentration and oxygen isotope ratio and since the improvement was more clearly shown in oxygen isotope ratio, this implied that more accurate *a posteriori* sources are estimated. Also, this indicates correct estimation of CO source distribution can be obtained when isotope information is combined with [CO] information.

The joint inversion result was compared to the inversion result using [CO] measured from 11 NOAA GMD stations in the NH. While the two observational data sets are independent, the inversion results estimate similar *a posteriori* source strengths and interannual trends. Thus, the joint inversion reliably constrains the CO sources albeit a small number of observational stations. Also, CO concentration and $\delta^{18}O$ were simultaneously and sequentially applied in the inversion analysis to find a more effective way for combining the two observations. While the sequential inversion provided more precise results (smaller *a posteriori* uncertainties), simultaneous inversion estimated more accurately constrained the CO sources (smaller model-observation difference).

In this study, the results of inversion analyses were evaluated by comparing *a posteriori* [CO] and $\delta^{18}O$ with measurements and the uncertainties raised from the inversion system is implicitly incorporated in the observation error covariance matrix ($\boldsymbol{S_e}$). However, the robustness of the inversion system (accuracy and precision) itself can be analyzed by using pseudo-data which is a data set the results of inversion analysis are explicitly known. Thus, further

inversion tests with pseudo-data sets will give more direct information about the ability of recovering the actual source strengths of the joint inversion system.

Isotope ratio measurements provide information about the CO sources and enables more robust inversion results since in this case the number of observations is doubled: [$C^{16}O$] and [$C^{18}O$] instead of [CO]. Thus, CO sources can be more tightly constrained. However, since its measurement is much more difficult than the concentration measurement, the observations of CO isotopes are very limited. Due to the limited number of observations in this study, CO sources were estimated annually on a hemispheric scale so as to avoid an ill-conditioned problem. Therefore, more fine spatial and temporal observation network and long-term measurement of CO isotopes are essential for obtaining detailed results of CO source estimates.

The carbon isotope information is also potentially useful to separate C3 (woody plants) and C4 (grasses) biomass burning since $\delta^{13}C$ of C4 plants is heavier than that of C3 plants. In addition to the oxygen isotopes, the incorporation of carbon isotopes in the inversion analysis constrains CO sources with four independent observations ($C^{16}O$, $C^{18}O$, ^{12}CO and ^{13}CO). It is expected that more precise and reliable source strengths estimates can be obtained from carbon isotope information.

Another limitation of using isotope information for optimizing CO source strengths is insufficient information of isotope source signature. Although the

globally and annually averaged current information of isotopic source signature applied in this study reproduced measurements fairly well, some of the sources are dependent on various climatic and environmental factors. For example, $\delta^{18}O$ from biomass burning is a function of burning temperature as well as is different for different species. Also, in spite of the importance of chemical oxidation sources of CO, there have been no direct measurements of CO isotope ratios reported. Therefore, further research about the isotopic source signatures is essential for more accurate CO sources estimates in fine spatial and temporal scale.

Last but not least, more CO concentration and isotope measurements are available from aircraft campaigns as well as CO concentration is available from satellite observations. This information overcomes the limitation of surface measurement since they provide observational information in fine temporal frequency and in fine vertical and horizontal resolution. Thus, if a new inversion method which combines various observations having a different spatial and temporal resolution without losing their advantages is developed, a global CO budget can be more tightly constrained in fine temporal and spatial resolution.

REFERENCES

Arellano, A. F., Jr., P. S. Kasibhatla, L. Giglio, G. R. van der Werf, and J. T. Randerson (2004), Top-down estimates of global CO sources using MOPITT measurements, *Geophys. Res. Lett.*, *31*(1), L01104.

Arellano, A. F., Jr., P. S. Kasibhatla, L. Giglio, G. R. van der Werf, J. T. Randerson, and G. J. Collatz (2006), Time-dependent inversion estimates of global biomass-burning CO emissions using Measurement of Pollution in the Troposphere (MOPITT) measurements, *J. Geophys. Res.*, *111*(D9), D09303.

Aster, R., B. Borchers, and C. Thurber (2005), Parameter Estimation and Inverse Problems, *International geophysics series, vol. 90, Elsevier Academic Press*.

Bergamaschi, P., et al. (1998), Isotope analysis based source identification for atmospheric CH_4 and CO sampled across Russia using the Trans-Siberian railroad, *Journal of Geophysical Research-Atmospheres*, *103*(D7), 8227 - 8235.

Bergamaschi, P., R. Hein, C. A. M. Brenninkmeijer, and P. J. Crutzen (2000a), Inverse modeling of the global CO cycle 2. Inversion of 13C/12C and 18O/16O isotope ratios, *J. Geophys. Res.*, *105*(D2), 1929-1945.

Bergamaschi, P., R. Hein, M. Heimann, and P. J. Crutzen (2000b), Inverse modeling of the global CO cycle 1. Inversion of CO mixing ratios, *J. Geophys. Res.*, *105*(D2), 1909-1927.

Bousquet, P., P. Ciais, P. Peylin, M. Ramonet, and P. Monfray (1999a), Inverse modeling of annual atmospheric CO_2 sources and sinks 1. Method and control inversion, *J. Geophys. Res.*, *104*(D21), 26161-26178.

Bousquet, P., P. Peylin, P. Ciais, M. Ramonet, and P. Monfray (1999b), Inverse modeling of annual atmospheric CO_2 sources and sinks 2. Sensitivity study, *J. Geophys. Res.*, *104*(D21), 26179-26193.

Bousquet, P., et al. (2006), Contribution of anthropogenic and natural sources to

atmospheric methane variability, *Nature*, *443*(7110), 439-443.

Brenninkmeijer, C. A. M. (1993), Measurement of the Abundance of ^{14}CO in the Atmosphere and the $^{13}C/^{12}C$ and $^{18}O/^{16}O$ Ration of Atmospheric CO with Applications in New Zealand and Antarctica, *J. Geophys. Res.*, *98*(D6), 10595-10614.

Brenninkmeijer, C. A. M., T. Röckmann, M. Bräunlich, P. Jöckel, and P. Bergamaschi (1999), Review of progress in isotope studies of atmospheric carbon monoxide, *Chemosphere - Global Change Science*, *1*(1-3), 33-52.

Burk, R. L., and M. Stuiver (1981), Oxygen isotope ratios in tree cellulose reflect mean annual temperature and humidity, *Science*, *211*, 1417 - 1419.

Chen, Y.-H., and R. G. Prinn (2006), Estimation of atmospheric methane emissions between 1996 and 2001 using a three-dimensional global chemical transport model, *J. Geophys. Res.*, *111*(D10), D10307.

Criss, R. E. (1999), Principles of Stable Isotope Distribution, *Oxford University Press, New York, USA*.

Duncan, B. N., J. A. Logan, I. Bey, I. A. Megretskaia, R. M. Yantosca, P. C. Novelli, N. B. Jones, and C. P. Rinsland (2007), Global budget of CO, 1988-997: Source estimates and validation with a global model, *J. Geophys. Res.*, *112*(D22), D22301.

Emmons, L. K., et al. (2006), Sensitivity of chemical budgets to meteorology in MOZART-4, *EOS Trans. AGU*, *87*(52), Fall Meet. Suppl.,. Abstract A51C-0094.

Emmons, L. K., et al. (2010), Description and evaluation of the Model for Ozone and Related chemical Tracers, version 4 (MOZART-4), *Geosci. Model Dev.*, *3*(1), 43-67.

Enting, I. G. (2002), Inverse problems in atmospheric constituent transport, *Cambridge University Press, UK*.

Erickson, D. J., III (1989), Ocean to Atmosphere Carbon Monoxide Flux: Global Inventory And Climate Implications, *Global Biogeochemical Cycles*, *3*(4), 305-

314.

Granier, C., G. Pétron, J.-F. Müller, and G. Brasseur (2000), The impact of natural and anthropogenic hydrocarbons on the tropospheric budget of carbon monoxide, *Atmospheric Environment*, *34*(29-30), 5255-5270.

Guenther, A., et al. (1995), A global model of natural volatile organic compound emissions, *J. Geophys. Res.*, *100*(D5), 8873-8892.

Guenther, A., T. Karl, P. Harley, C. Wiedinmyer, P. I. Palmer, and C. Geron (2006), Estimates of global terrestrial isoprene emissions using MEGAN (Model of Emissions of Gases and Aerosols from Nature), *Atmos. Chem. Phys.*, *6*(11), 3181-3210.

Hansen, J., R. Ruedy, M. Sato, and R. Reynolds (1996), Global surface air temperature in 1995: Return to pre-Pinatubo level, *Geophysical Research Letters*, *23*(13), 1665-1668.

Hansen, J., R. Ruedy, M. Sato, and K. Lo (2002), Global Warming Continues, *Science*, *295*(5553), 275c-.

Hansen, J., M. Sato, R. Ruedy, K. Lo, D. W. Lea, and M. Medina-Elizade (2006), Global temperature change, *Proceedings of the National Academy of Sciences*, *103*(39), 14288-14293.

Heald, C. L., et al. (2004), Comparative inverse analysis of satellite (MOPITT) and aircraft (TRACE-P) observations to estimate Asian sources of carbon monoxide, *J. Geophys. Res.*, *109*(D23), D23306.

Heimann, M., and T. Kaminski (1999), Inverse modelling approaches to infer surface trace gas fluxes from observed atmospheric mixing ratios, in *Developments in Atmospheric Science*, edited by A. F. Bouwman, pp. 277-295, Elsevier.

Hein, R., P. J. Crutzen, and M. Heimann (1997a), An Inverse Modeling Approach to Investigate the Global Atmospheric Methane Cycle, *Global Biogeochem. Cycles*, *11*(1), 43-76.

Hein, R., P. J. Crutzen, and M. Heimann (1997b), An Inverse Modeling Approach to Investigate the Global Atmospheric Methane Cycle, *Global Biogeochem. Cycles*, *11*(1), 43-76.

Ho, S.-P., D. P. Edwards, J. C. Gille, M. Luo, G. B. Osterman, S. S. Kulawik, and H. Worden (2009), A global comparison of carbon monoxide profiles and column amounts from Tropospheric Emission Spectrometer (TES) and Measurements of Pollution in the Troposphere (MOPITT), *J. Geophys. Res.*, *114*(D21), D21307.

Horowitz, L. W., et al. (2003), A global simulation of tropospheric ozone and related tracers: Description and evaluation of MOZART, version 2, *J. Geophys. Res.*, *108*(D24), 4784.

Horowitz, L. W., A. M. Fiore, G. P. Milly, R. C. Cohen, A. Perring, P. J. Wooldridge, P. G. Hess, L. K. Emmons, and J.-F. Lamarque (2007), Observational constraints on the chemistry of isoprene nitrates over the eastern United States, *J. Geophys. Res.*, *112*(D12), D12S08.

Houghton, J. T., Y. Ding, D. J. Griggs, N. Noguer, P. J. van der Linden, X. Dai, K. Maskell, and C. A. Johnson (2001), Climate Change 2001: The Scientific Basis. Cambridge university Press

IPCC (2001), Climate Chamge 2001: The Scientific Basis, *Intergovernmental Panel on Climate Change, Cambridge University Press, Cambridge, UK*.

Kalnay, E., et al. (1996), The NCEP/NCAR 40-Year Reanalysis Project, *Bulletin of the American Meteorological Society*, *77*(3), 437-471.

Kasibhatla, P., A. Arellano, J. A. Logan, P. I. Palmer, and P. Novelli (2002), Top-down estimate of a large source of atmospheric carbon monoxide associated with fuel combustion in Asia, *Geophys. Res. Lett.*, *29*(19), 1900.

Kato, S., H. Akimoto, T. Röckmann, M. Bräunlich, and C. A. M. Brenninkmeijer (1999), Stable isotopic compositions of carbon monoxide from biomass burning experiments, *Atmospheric Environment*, *33*(27), 4357-4362.

Keeling, C. D. (1958), The concentration and isotopic abundances of atmospheric carbon dioxide in rural areas, *Geochimica et Cosmochimica Acta*, *13*(4), 322-334.

Keeling, C. D. (1961), The concentration and isotopic abundances of carbon dioxide in rural and marine air, *Geochimica et Cosmochimica Acta*, *24*(3-4), 277-298.

Khalil, M. A. K., and R. A. Rasmussen (1994), Global decrease in atmospheric carbon monoxide concentration, *Nature*, *370*(6491), 639-641.

Kistler, R., et al. (2001), The NCEP–NCAR 50–Year Reanalysis: Monthly Means CD–ROM and Documentation, *Bulletin of the American Meteorological Society*, *82*(2), 247-267.

Lathière, J., D. A. Hauglustaine, A. D. Friend, N. De Noblet-Ducoudré, N. Viovy, and G. A. Folberth (2006), Impact of climate variability and land use changes on global biogenic volatile organic compound emissions, *Atmos. Chem. Phys.*, *6*(8), 2129-2146.

Lawrence, M. G., P. J. Crutzen, P. J. Rasch, B. E. Eaton, and N. M. Mahowald (1999), A model for studies of tropospheric photochemistry: Description, global distributions, and evaluation, *Journal of Geophysical Research*, *104*, 26245 - 26277.

Lawrence, M. G., P. Jöckel, and R. von Kuhlmann (2001), What does the global mean OH concentration tell us?, *Atmos. Chem. Phys.*, *1*(1), 37-49.

Levin, I., et al. (2010), The global SF6 source inferred from long-term high precision atmospheric measurements and its comparison with emission inventories, *Atmos. Chem. Phys.*, *10*(6), 2655-2662.

Lewis, A. C., J. R. Hopkins, L. J. Carpenter, J. Stanton, K. A. Read, and M. J. Pilling (2005), sources and sinks of acetone, methanol, and acetaldehyde in North Atlantic marine air, *Atmospheric Chemistry and Physics*, *5*, 1963 - 1974.

Lin, Y.-C., J. Cho, G. A. Tompsett, P. R. Westmoreland, and G. W. Huber (2009), Kinetic and Mechanism of Cellulose Pyrolysis, *Journal of Physical Chemistry C*, *113*, 20097 - 20107.

Lines, L. R., A. K. Schultz, and S. Treitel (1988), Cooperative inversion of geophysical data, *Geophysics*, *53*(1), 8-20.

Mak, J. E., and C. A. M. Brenninkmeijer (1994), Compressed Air Sample Technology for the Isotopic Analysis of Atmospheric Carbon Monoxide, *Journal of Atmospheric and Oceanic Technology*, *11*(2), 425-431.

Mak, J. E., G. Kra, T. Sandomenico, and P. Bergamaschi (2003), The seasonally varying isotopic composition of the sources of carbon monoxide at Barbados, West Indies, *J. Geophys. Res.*, *108*(D20), 4635.

Manning, M. R., C. A. M. Brenninkmeijer, and W. Allan (1997), Atmospheric carbon monoxide budget of the southern hemisphere: Implications of 13C/12C measurements, *J. Geophys. Res.*, *102*(D9), 10673-10682.

Mikaloff Fletcher, S. E., P. P. Tans, L. M. Bruhwiler, J. B. Miller, and M. Heimann (2004), CH_4 sources estimated from atmospheric observations of CH_4 and its $^{13}C/^{12}C$ isotopic ratios: 1. Inverse modeling of source processes, *Global Biogeochem. Cycles*, *18*(4), GB4004.

Miller, J. B., K. A. Mack, R. Dissly, J. W. C. White, E. J. Dlugokencky, and P. P. Tans (2002), Development of analytical methods and measurements of $^{13}C/^{12}C$ in atmospheric CH_4 from the NOAA Climate Monitoring and Diagnostics Laboratory Global Air Sampling Network, *J. Geophys. Res.*, *107*(D13), 4178.

Miyoshi, A., S. Hatakeyama, and N. Washida (1999), OH radical- initiated photooxidation of isoprene: An estimate of global CO production, *Journal of Geophysical Research-Atmospheres*, *99*(D9), 18779 - 18787.

Mühle, J., et al. (2010), Perfluorocarbons in the global atmosphere: tetrafluoromethane, hexafluoroethane, and octafluoropropane, *Atmos. Chem. Phys.*, *10*(11), 5145-5164.

Müller, J.-F., and G. Brasseur (1995), IMAGES: A three-dimensional chemical transport model of the global troposphere, *J. Geophys. Res.*, *100*(D8), 16445-16490.

Müller, J. F., and T. Stavrakou (2005), Inversion of CO and NOx emissions using the adjoint of the IMAGES model, *Atmos. Chem. Phys.*, *5*(5), 1157-1186.

Müller, J. F., et al. (2008), Global isoprene emissions estimated using MEGAN, ECMWF analyses and a detailed canopy environment model, *Atmos. Chem. Phys.*,

8(5), 1329-1341.

Naik, V., C. Delire, and D. J. Wuebbles (2004), Sensitivity of global biogenic isoprenoid emissions to climate variability and atmospheric CO2, *J. Geophys. Res.*, *109*(D6), D06301.

Novelli, P. C., K. A. Masarie, and P. M. Lang (1998a), Distributions and recent changes of carbon monoxide in the lower troposphere, *Journal of Geophysical Research*, *103*(D15), 19015-19033.

Novelli, P. C., K. A. Masarie, and P. M. Lang (1998b), Distributions and recent changes of carbon monoxide in the lower troposphere, *J. Geophys. Res.*, *103*(D15), 19015-19033.

Novelli, P. C., K. A. Masarie, P. M. Lang, B. D. Hall, R. C. Myers, and J. W. Elkins (2003a), Reanalysis of tropospheric CO trends: Effects of the 1997-1998 wildfires, *Journal of Geophysical Research*, *108*(D15).

Novelli, P. C., K. A. Masarie, P. M. Lang, B. D. Hall, R. C. Myers, and J. W. Elkins (2003b), Reanalysis of tropospheric CO trends: Effects of the 1997-1998 wildfires, *J. Geophys. Res.*, *108*(D15), 4464.

Olivier, J., A. F. Bouwman, C. Maas, J. Berdowski, C. Veldt, J. Bloos, A. Visschedijk, P. Zandveld, and J. Haverlag (1996), Description of EDGAR Version 2.0: A set of global emission inventories of greenhouse gases and ozone-depleting substances for all anthropogenic and most natural sources on a per country basis and on 1 degree x 1 degree grid, *RIVM report nr. 771060 002 / TNO-MEP report nr. R96/119*.

Olivier, J., J. Peters, C. Granier, G. Petron, J. F. Müller, and S. Wallens (2003), Present and future surface emissions of atmospheric compounds, *POET report #2, EU project EVK2-1999-00011*.

Pacifico, F., S. P. Harrison, C. D. Jones, and S. Sitch (2009), Isoprene emissions and climate, *Atmospheric Environment*, *43*(39), 6121-6135.

Palmer, P. I., D. J. Jacob, D. B. A. Jones, C. L. Heald, R. M. Yantosca, J. A. Logan, G. W. Sachse, and D. G. Streets (2003), Inverting for emissions of carbon monoxide from Asia using aircraft observations over the western Pacific, *J.*

Geophys. Res., *108*(D21), 8828.

Palmer, P. I., P. Suntharalingam, D. B. A. Jones, D. J. Jacob, D. G. Streets, Q. Fu, S. A. Vay, and G. W. Sachse (2006), Using CO_2:CO correlations to improve inverse analyses of carbon fluxes, *J. Geophys. Res.*, *111*(D12), D12318.

Pataki, D. E., J. R. Ehleringer, L. B. Flanagan, D. Yakir, D. R. Bowling, C. J. Still, N. Buchmann, J. O. Kaplan, and J. A. Berry (2003), The application and interpretation of Keeling plots in terrestrial carbon cycle research, *Global Biogeochem. Cycles*, *17*(1), 1022.

Pétron, G., C. Granier, B. Khattatov, J.-F. Lamarque, V. Yudin, J.-F. Müller, and J. Gille (2002), Inverse modeling of carbon monoxide surface emissions using Climate Monitoring and Diagnostics Laboratory network observations, *J. Geophys. Res.*, *107*(D24), 4761.

Pétron, G., C. Granier, B. Khattatov, V. Yudin, J.-F. Lamarque, L. Emmons, J. Gille, and D. P. Edwards (2004), Monthly CO surface sources inventory based on the 2000-2001 MOPITT satellite data, *Geophys. Res. Lett.*, *31*(21), L21107.

Pfister, G., G. Pétron, L. K. Emmons, J. C. Gille, D. P. Edwards, J. F. Lamarque, J. L. Attie, C. Granier, and P. C. Novelli (2004), Evaluation of CO simulations and the analysis of the CO budget for Europe, *J. Geophys. Res.*, *109*(D19), D19304.

Pfister, G., P. G. Hess, L. K. Emmons, J. F. Lamarque, C. Wiedinmyer, D. P. Edwards, G. Pétron, J. C. Gille, and G. W. Sachse (2005), Quantifying CO emissions from the 2004 Alaskan wildfires using MOPITT CO data, *Geophys. Res. Lett.*, *32*(11), L11809.

Pfister, G. G., et al. (2006), Ozone production from the 2004 North American boreal fires, *J. Geophys. Res.*, *111*(D24), D24S07.

Pfister, G. G., L. K. Emmons, P. G. Hess, J. F. Lamarque, J. J. Orlando, S. Walters, A. Guenther, P. I. Palmer, and P. J. Lawrence (2008a), Contribution of isoprene to chemical budgets: A model tracer study with the NCAR CTM MOZART-4, *J. Geophys. Res.*, *113*(D5), D05308.

Pfister, G. G., P. G. Hess, L. K. Emmons, P. J. Rasch, and F. M. Vitt (2008b), Impact of the summer 2004 Alaska fires on top of the atmosphere clear-sky

radiation fluxes, *J. Geophys. Res.*, *113*(D2), D02204.

Pilkington, M. (2006a), Joint inversion of gravity and magnetic data for two-layer models, *Geophysics*, *71*(3), L35-L42.

Pilkington, M. (2006b), Joint inversion of gravity and magnetic data for two-layer models, *Geophysics*, *71*(3), 35-42.

Rayner, P. J., R. M. Law, C. E. Allison, R. J. Francey, C. M. Trudinger, and C. Pickett-Heaps (2008a), Interannual variability of the global carbon cycle (1992–2005) inferred by inversion of atmospheric CO2 and δ13CO2 measurements, *Global Biogeochem. Cycles*, *22*(3), GB3008.

Rayner, P. J., R. M. Law, C. E. Allison, R. J. Francey, C. M. Trudinger, and C. Pickett-Heaps (2008b), Interannual variability of the global carbon cycle (1992-2005) inferred by inversion of atmospheric CO2 and δ13CO2 measurements, *Global Biogeochem. Cycles*, *22*(3), GB3008.

Röckmann, T., C. A. M. Brenninkmeijer, G. Saueressig, P. Bergamaschi, J. N. Crowley, H. Fischer, and P. J. Crutzen (1998), Mass-Independent Oxygen Isotope Fractionation in Atmospheric CO as a Result of the Reaction CO + OH, *Science*, *281*(5376), 544-546.

Rodgers, C. (2000), Inverse Methods For Atmospheric Sounding: Theory And Practice, *Series on Atmospheric, Oceanic and Planetary Physics Vol. 2*, *World Scientific Publishing Company, Singapore*.

Sanderson, M. G., W. J. Collins, R. G. Derwent, and C. E. Johnson (2003), Simulation of Global Hydrogen Levels Using a Lagrangian Three-Dimensional Model, *Journal of Atmospheric Chemistry*, *46*(1), 15-28.

Saurer, M., S. Borella, and L. M. (1997), δ18O of tree rings of beech (Fagus sylvatica) as a record of δ18O of the growing season precipitation, *Tellus, 49B*, 80 - 92.

Saurer, M., P. Cherubini, and R. T. W. Siegwolf (2000), Oxygen isotopes in tree rings of Abies alba: The climatic significance of interdecadal variations, *Journal of Geophysical Research-Atmospheres*, *105*(D10), 12461 - 12470.

Saurer, M., A. S. H. Prévôt, J. Dommen, J. Sandradewi, U. Baltensperger, and R. T. W. Siegwolf (2009), The influence of traffic and wood combustion on the stable isotopic composition of carbon monoxide, *Atmos. Chem. Phys.*, *9*(9), 3147-3161.

Shindell, D. T., et al. (2006), Multimodel simulations of carbon monoxide: Comparison with observations and projected near-future changes, *J. Geophys. Res.*, *111*(D19), D19306.

Shindell, D. T., G. Faluvegi, S. Bauer, D. Koch, N. Unger, S. Menon, R. L. Miller, G. Schmidt, and D. G. Streets (2007), Climate response to projected changes in short-lived species under an A1B scenarioi from 2000-2050 in the GISS climate model, *Journal of Geophysical Research-Atmospheres*, *112*, D20103.

Shindell, D. T., H. L. II, M. D. Schwarzkopf, L. W. Horowitz, J. F. Lamarque, and G. Faluvegi (2008), Multimodel projections of climate change from short-lived emissions due to human activities, *Journal of Geophysical Research-Atmospheres*, *113*, D11109.

Smith, T. M., R. W. Reynolds, R. E. Livezey, and D. C. Stokes (1996), Reconstruction of historical sea surface temperatures using empirical orthogonal functions, *Journal of Climate*, *9*(6), 1403-1420.

Smith, T. M., R. W. Reynolds, T. C. Peterson, and J. Lawrimore (2008), Improvements to NOAA's Historical Merged Land–Ocean Surface Temperature Analysis (1880–2006), *Journal of Climate*, *21*(10), 2283-2296.

Stevens, C. M., and A. F. Wagner (1989), The role of isotope fractionation effects in atmospheric chemistry, *Zeitschrift für Naturforschung*, *44a*, 376-384.

Stevenson, D. S., et al. (2006), Multimodel ensemble simulations of present-day and near-future tropospheric ozone, *J. Geophys. Res.*, *111*(D8), D08301.

Stohl, A., et al. (2010), Hydrochlorofluorocarbon and hydrofluorocarbon emissions in East Asia determined by inverse modeling, *Atmos. Chem. Phys.*, *10*(8), 3545-3560.

Tsunogai, U., F. Nakagawa, D. D. Komatsu, and T. Gamo (2002), Stable Carbon and Oxygen Isotopic Analysis of Atmospheric Carbon Monoxide Using

Continuous-Flow Isotope Ratio MS by Isotope Ratio Monitoring of CO, *Analytical Chemistry*, *74*(22), 5695-5700.

Tsunogai, U., Y. Hachisu, D. D. Komatsu, F. Nakagawa, T. Gamo, and K.-i. Akiyama (2003), An updated estimation of the stable carbon and oxygen isotopic compositions of automobile CO emissions, *Atmospheric Environment*, *37*, 4901 - 4910.

Weiss, R. F., J. Mühle, P. K. Salameh, and C. M. Harth (2008), Nitrogen trifluoride in the global atmosphere, *Geophys. Res. Lett.*, *35*(20), L20821.

Williams, J., H. Fischer, S. Wong, P. J. Crutzen, M. P. Scheele, and J. Lelieveld (2002), Near equatorial CO and O-3 profiles over the Indian Ocean during the winter monsoon: High O-3 levels in the middle troposphere and interhemispheric exchange, *Journal of Geophysical Research-Atmospheres*, *107*(D19).

Yurganov, L. N., et al. (2005), Increased Northern Hemispheric carbon monoxide burden in the troposphere in 2002 and 2003 detected from the ground and from space, *Atmos. Chem. Phys.*, *5*(2), 563-573.

Appendix A.

MOZART-4 simulation results: source contribution at each station, $\delta^{18}O$ of each source and contribution of emissions for each geographic region (FF, BF and BB only)

Alert

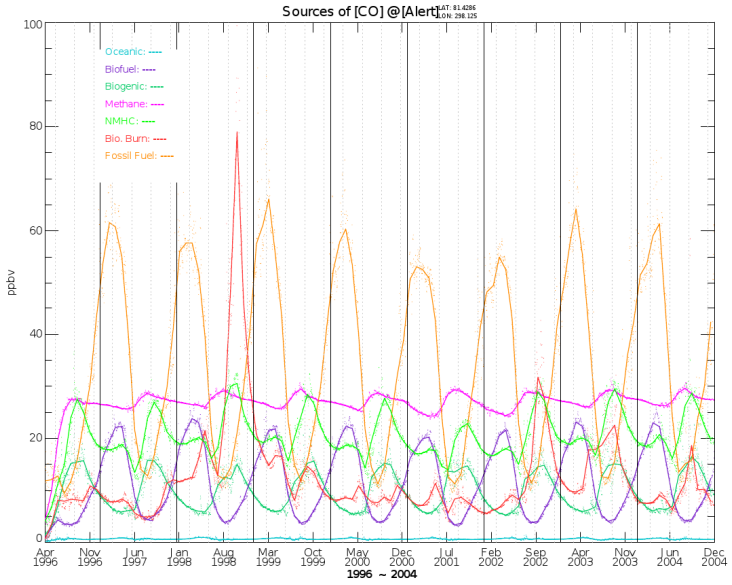

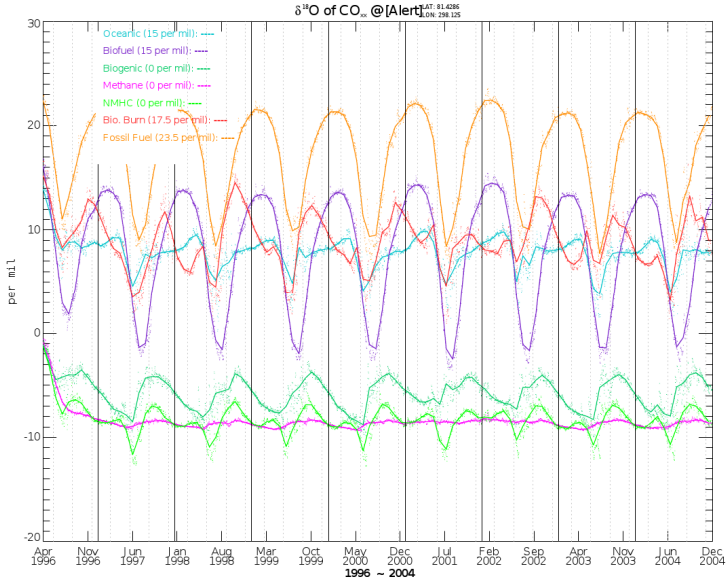

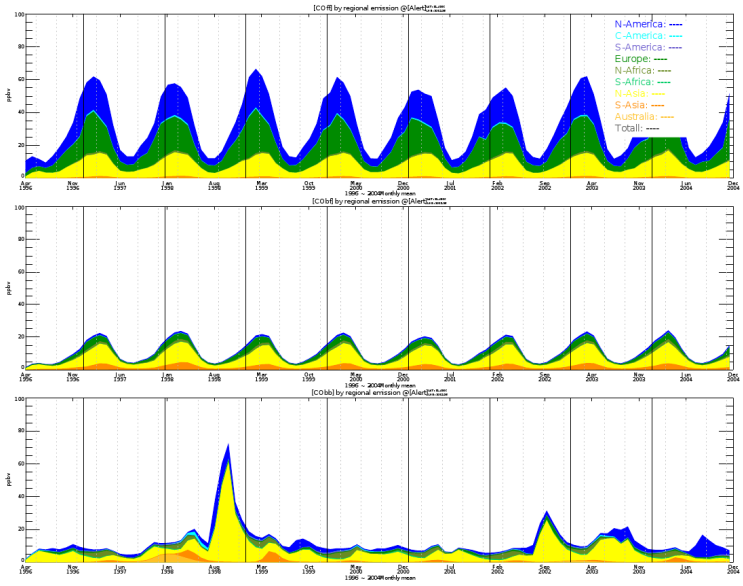

Spitzbergen

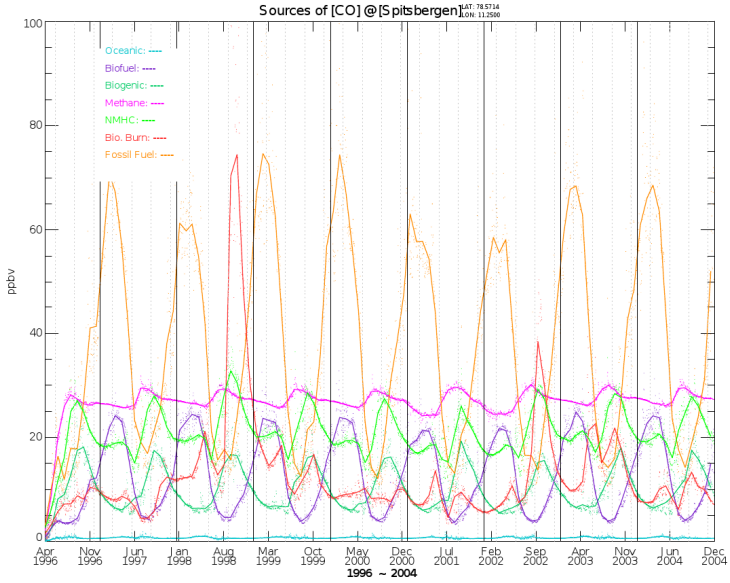
Sources of [CO] @[Spitsbergen]
LAT: 78.5714
LON: 11.2500
Oceanic: ----
Biofuel: ----
Biogenic: ----
Methane: ----
NMHC: ----
Bio. Burn: ----
Fossil Fuel: ----
ppbv
100
80
60
40
20
0
Apr 1996
Nov 1996
Jun 1997
Jan 1998
Aug 1998
Mar 1999
Oct 1999
May 2000
Dec 2000
Jul 2001
Feb 2002
Sep 2002
Apr 2003
Nov 2003
Jun 2004
Dec 2004
1996 ~ 2004

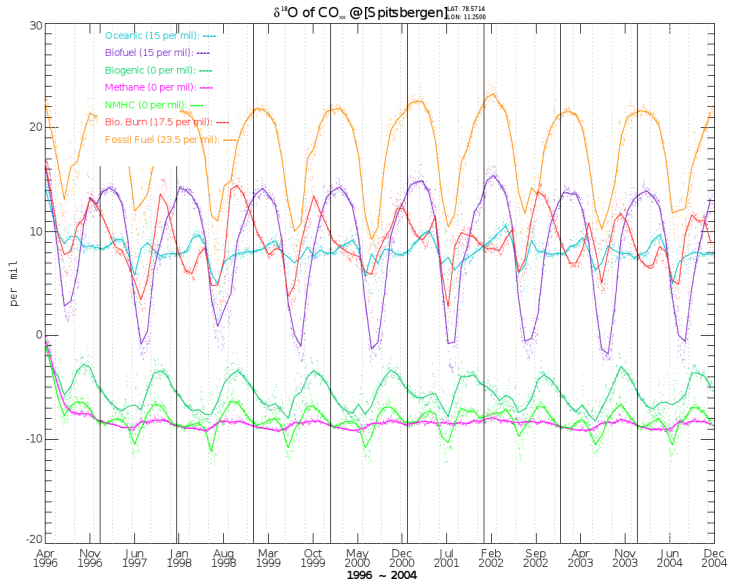
δ18O of CO in @[Spitsbergen]
LAT: 78.5714
LON: 11.2500
Oceanic (15 per mil): ----
Biofuel (15 per mil): ----
Biogenic (0 per mil): ----
Methane (0 per mil): ----
NMHC (0 per mil): ----
Bio. Burn (17.5 per mil): ----
Fossil Fuel (23.5 per mil): ----
per mil
30
20
10
0
-10
-20
Apr 1996
Nov 1996
Jun 1997
Jan 1998
Aug 1998
Mar 1999
Oct 1999
May 2000
Dec 2000
Jul 2001
Feb 2002
Sep 2002
Apr 2003
Nov 2003
Jun 2004
Dec 2004
1996 ~ 2004

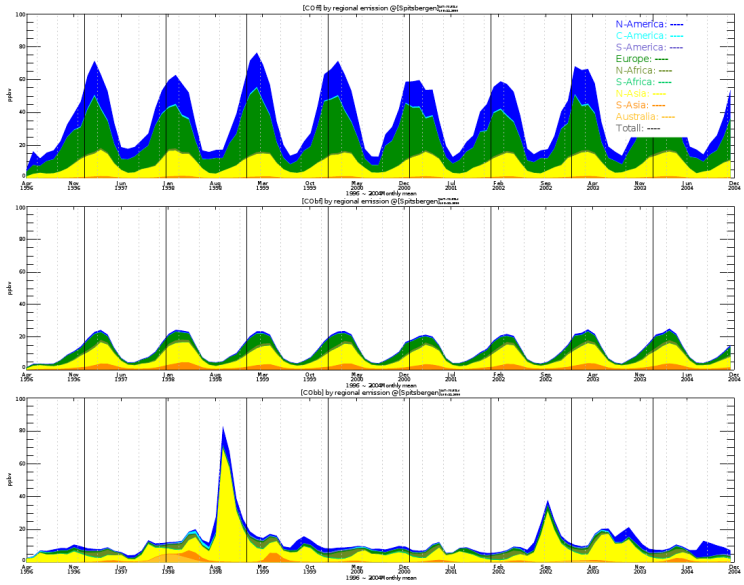
N-America: ----
C-America: ----
S-America: ----
Europe: ----
N-Africa: ----
S-Africa: ----
N-Asia: ----
S-Asia: ----
Australia: ----
Totall: ----

Iceland

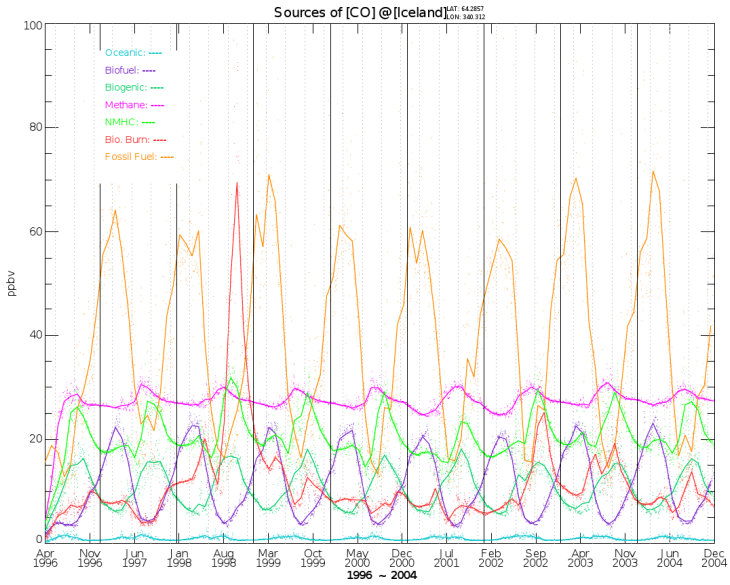
Sources of [CO] @[Iceland]
LAT: 64.2857
LON: 340.312
Oceanic: ----
Biofuel: ----
Biogenic: ----
Methane: ----
NMHC: ----
Bio. Burn: ----
Fossil Fuel: ----
ppbv
100
80
60
40
20
0
Apr 1996
Nov 1996
Jun 1997
Jan 1998
Aug 1998
Mar 1999
Oct 1999
May 2000
Dec 2000
Jul 2001
Feb 2002
Sep 2002
Apr 2003
Nov 2003
Jun 2004
Dec 2004
1996 ~ 2004

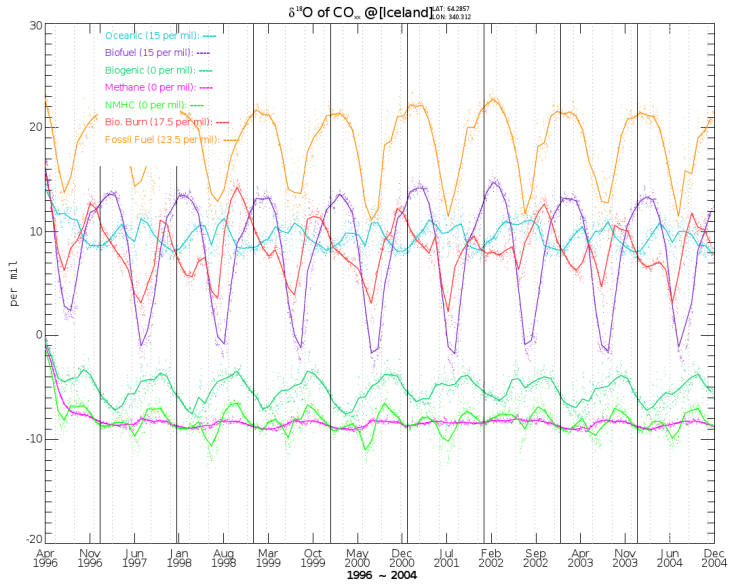
δ18O of CO2 @[Iceland]
LAT: 64.2857
LON: 340.312
Oceanic (15 per mil): ----
Biofuel (15 per mil): ----
Biogenic (0 per mil): ----
Methane (0 per mil): ----
NMHC (0 per mil): ----
Bio. Burn (17.5 per mil): ----
Fossil Fuel (23.5 per mil): ----
per mil
30
20
10
0
-10
-20
Apr 1996
Nov 1996
Jun 1997
Jan 1998
Aug 1998
Mar 1999
Oct 1999
May 2000
Dec 2000
Jul 2001
Feb 2002
Sep 2002
Apr 2003
Nov 2003
Jun 2004
Dec 2004
1996 ~ 2004

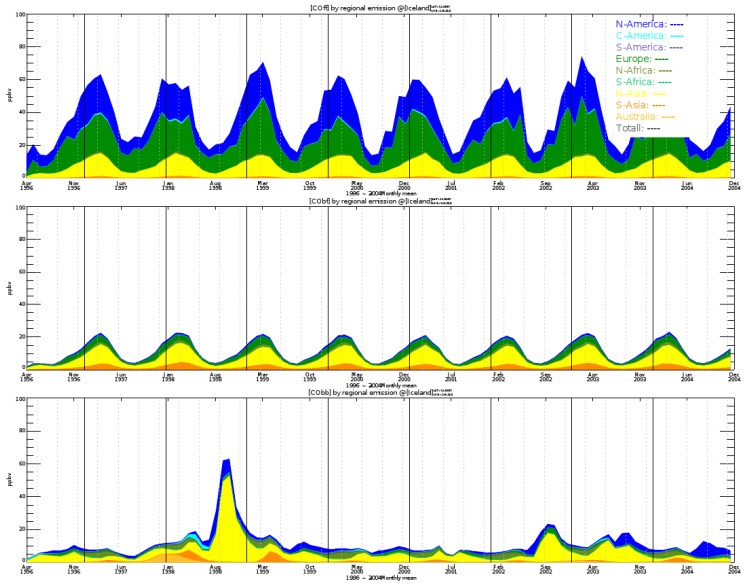
[COff] by regional emission @Iceland
N-America: ----
C-America: ----
S-America: ----
Europe: ----
N-Africa: ----
S-Africa: ----
N-Asia: ----
S-Asia: ----
Australia: ----
Total: ----
ppbv
1996 ~ 2004Monthly mean
[CObf] by regional emission @Iceland
ppbv
1996 ~ 2004Monthly mean
[CObb] by regional emission @Iceland
ppbv
1996 ~ 2004Monthly mean

Izana

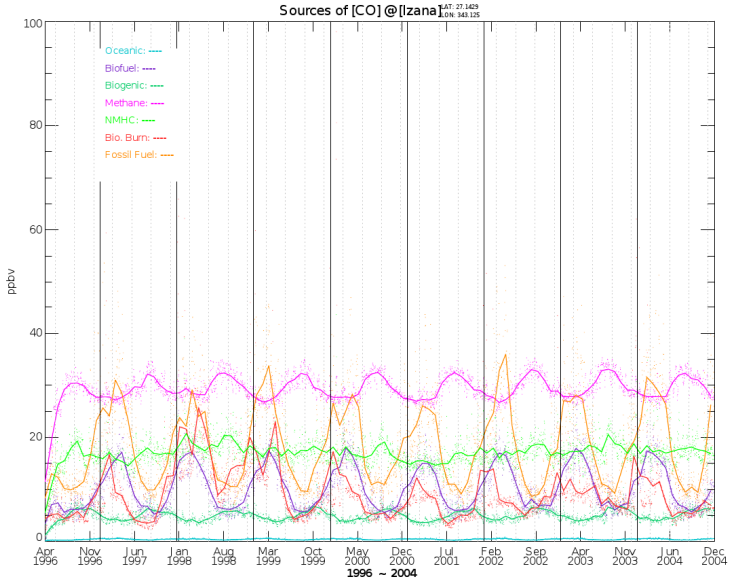
Sources of [CO] @[Izana]
LAT: 27.1429
LON: 343.125
Oceanic: ----
Biofuel: ----
Biogenic: ----
Methane: ----
NMHC: ----
Bio. Burn: ----
Fossil Fuel: ----
ppbv
100
80
60
40
20
0
Apr 1996
Nov 1996
Jun 1997
Jan 1998
Aug 1998
Mar 1999
Oct 1999
May 2000
Dec 2000
Jul 2001
Feb 2002
Sep 2002
Apr 2003
Nov 2003
Jun 2004
Dec 2004
1996 ~ 2004

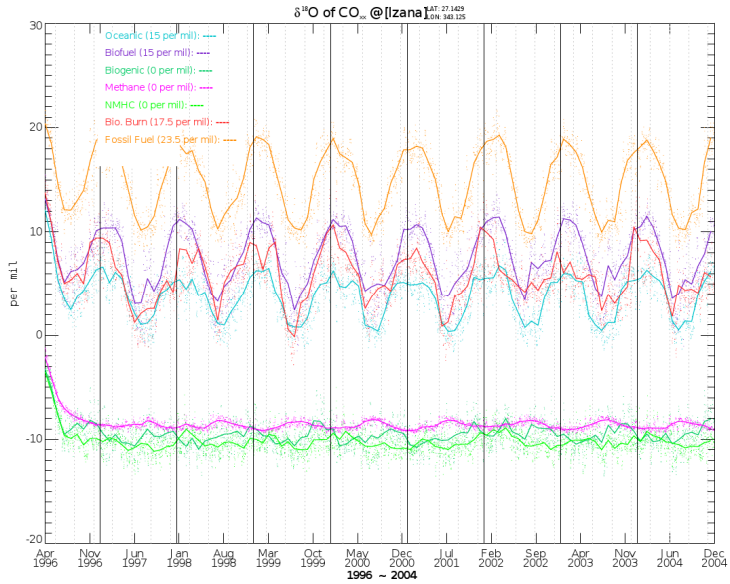
δ18O of CO∞ @[Izana]
LAT: 27.1429
LON: 343.125
Oceanic (15 per mil): ----
Biofuel (15 per mil): ----
Biogenic (0 per mil): ----
Methane (0 per mil): ----
NMHC (0 per mil): ----
Bio. Burn (17.5 per mil): ----
Fossil Fuel (23.5 per mil): ----
per mil
30
20
10
0
-10
-20
Apr 1996
Nov 1996
Jun 1997
Jan 1998
Aug 1998
Mar 1999
Oct 1999
May 2000
Dec 2000
Jul 2001
Feb 2002
Sep 2002
Apr 2003
Nov 2003
Jun 2004
Dec 2004
1996 ~ 2004

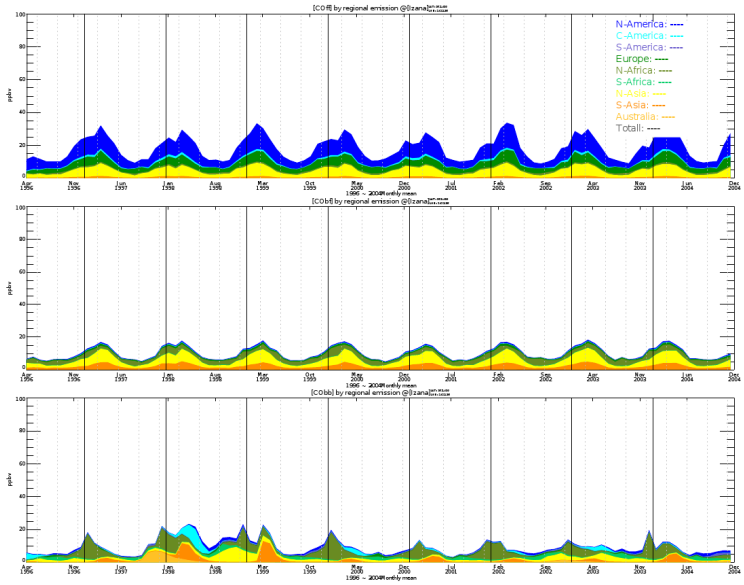
N-America: ----
C-America: ----
S-America: ----
Europe: ----
N-Africa: ----
S-Africa: ----
N-Asia: ----
S-Asia: ----
Australia: ----
Total: ----

Mauna Loa

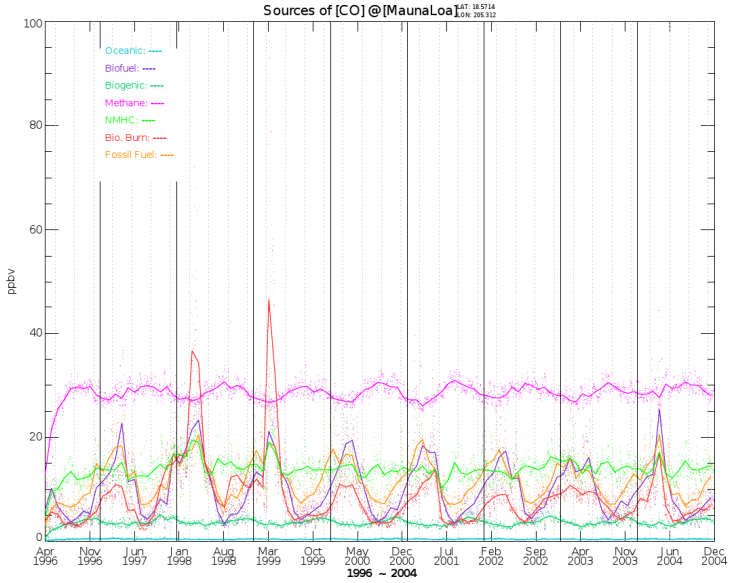
Sources of [CO] @[MaunaLoa]
LAT: 18.5714
LON: 205.312
Oceanic: ----
Biofuel: ----
Biogenic: ----
Methane: ----
NMHC: ----
Bio. Burn: ----
Fossil Fuel: ----
ppbv
100
80
60
40
20
0
Apr 1996
Nov 1996
Jun 1997
Jan 1998
Aug 1998
Mar 1999
Oct 1999
May 2000
Dec 2000
Jul 2001
Feb 2002
Sep 2002
Apr 2003
Nov 2003
Jun 2004
Dec 2004
1996 ~ 2004

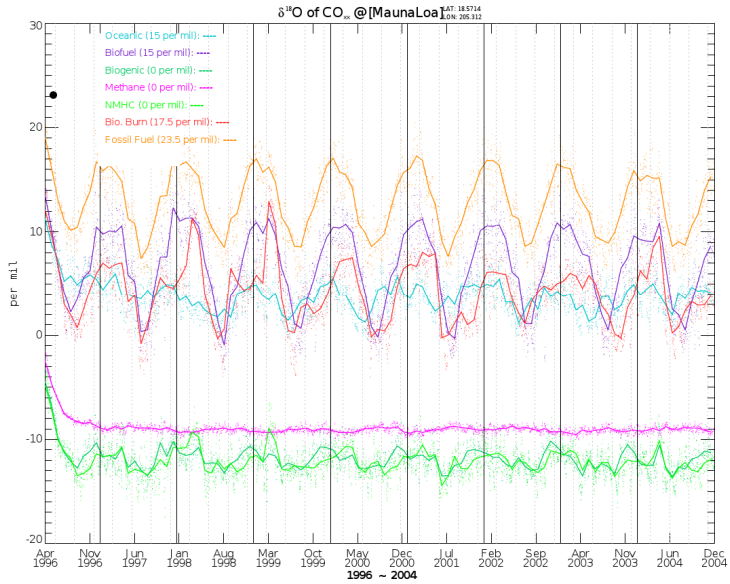
δ18O of CO∞ @[MaunaLoa]
LAT: 18.5714
LON: 205.312
Oceanic (15 per mil): ----
Biofuel (15 per mil): ----
Biogenic (0 per mil): ----
Methane (0 per mil): ----
NMHC (0 per mil): ----
Bio. Burn (17.5 per mil): ----
Fossil Fuel (23.5 per mil): ----
per mil
30
20
10
0
-10
-20
Apr 1996
Nov 1996
Jun 1997
Jan 1998
Aug 1998
Mar 1999
Oct 1999
May 2000
Dec 2000
Jul 2001
Feb 2002
Sep 2002
Apr 2003
Nov 2003
Jun 2004
Dec 2004
1996 ~ 2004

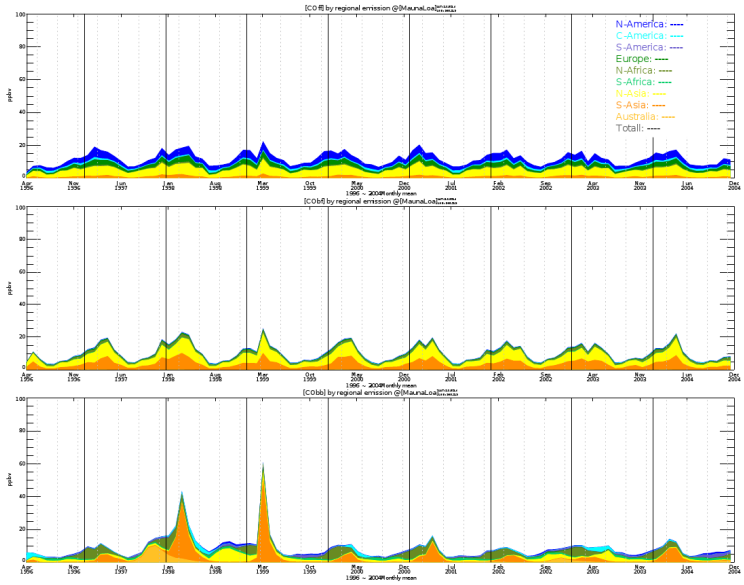
N-America: ----
C-America: ----
S-America: ----
Europe: ----
N-Africa: ----
S-Africa: ----
N-Asia: ----
S-Asia: ----
Australia: ----
Total: ----

Barbados

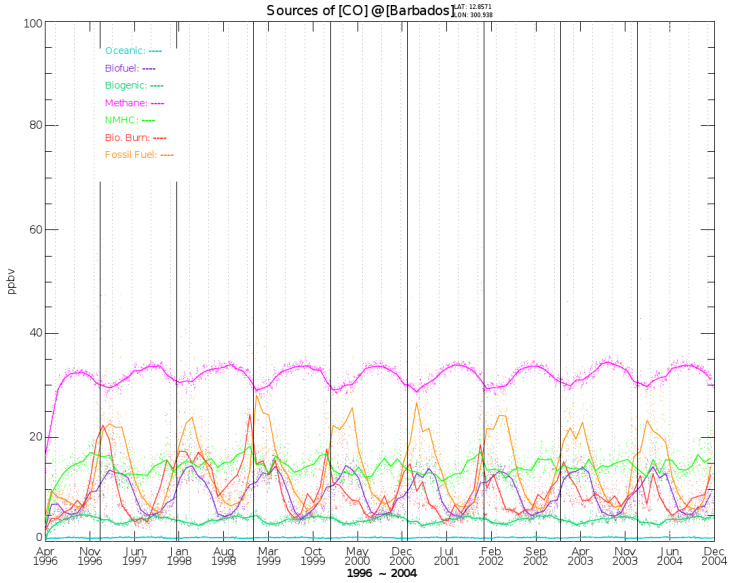
Sources of [CO] @[Barbados]
LAT: 12.8571
LON: 300.938
Oceanic: ----
Biofuel: ----
Biogenic: ----
Methane: ----
NMHC: ----
Bio. Burn: ----
Fossil Fuel: ----
ppbv
100
80
60
40
20
0
Apr 1996
Nov 1996
Jun 1997
Jan 1998
Aug 1998
Mar 1999
Oct 1999
May 2000
Dec 2000
Jul 2001
Feb 2002
Sep 2002
Apr 2003
Nov 2003
Jun 2004
Dec 2004
1996 ~ 2004

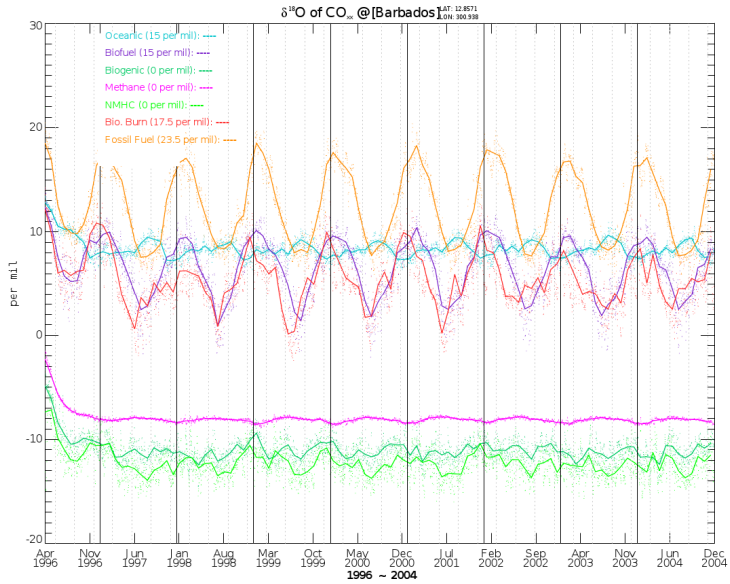
δ18O of CO2 @[Barbados]
LAT: 12.8571
LON: 300.938
Oceanic (15 per mil): ----
Biofuel (15 per mil): ----
Biogenic (0 per mil): ----
Methane (0 per mil): ----
NMHC (0 per mil): ----
Bio. Burn (17.5 per mil): ----
Fossil Fuel (23.5 per mil): ----
per mil
30
20
10
0
-10
-20
Apr 1996
Nov 1996
Jun 1997
Jan 1998
Aug 1998
Mar 1999
Oct 1999
May 2000
Dec 2000
Jul 2001
Feb 2002
Sep 2002
Apr 2003
Nov 2003
Jun 2004
Dec 2004
1996 ~ 2004

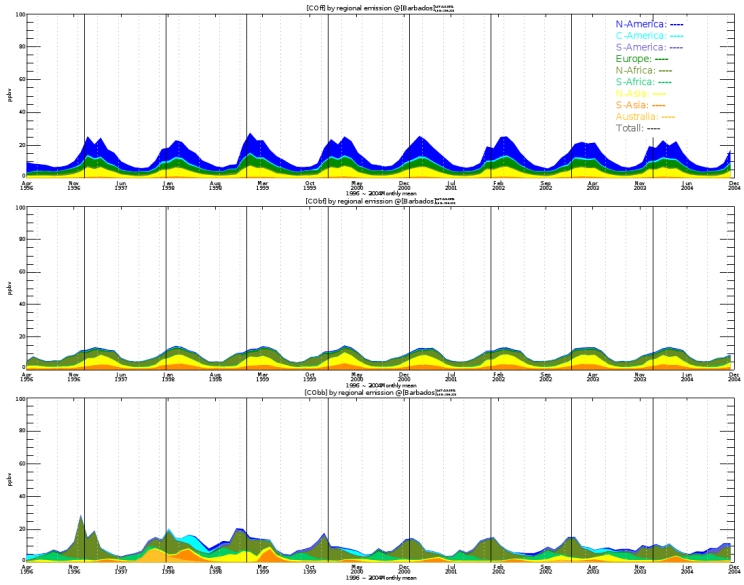
N-America: ----
C-America: ----
S-America: ----
Europe: ----
N-Africa: ----
S-Africa: ----
N-Asia: ----
S-Asia: ----
Australia: ----
Totall: ----

Baring head

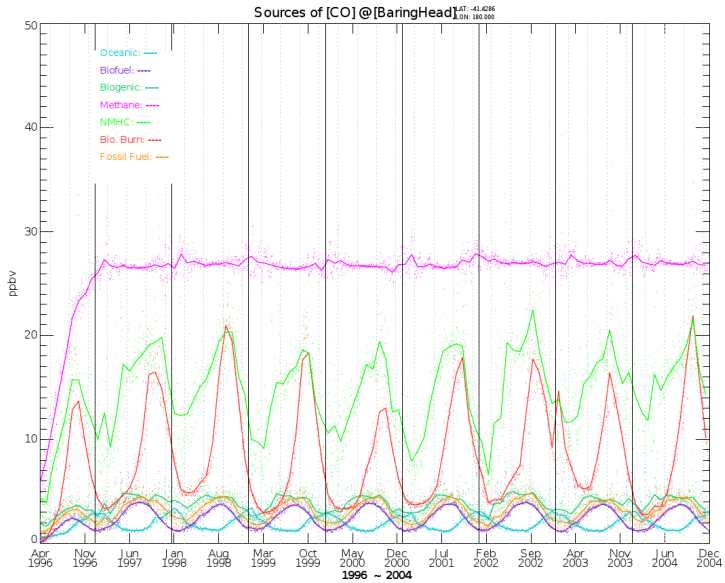
Sources of [CO] @[BaringHead]
Oceanic: ----
Biofuel: ----
Biogenic: ----
Methane: ----
NMHC: ----
Bio. Burn: ----
Fossil Fuel: ----
ppbv
1996 ~ 2004

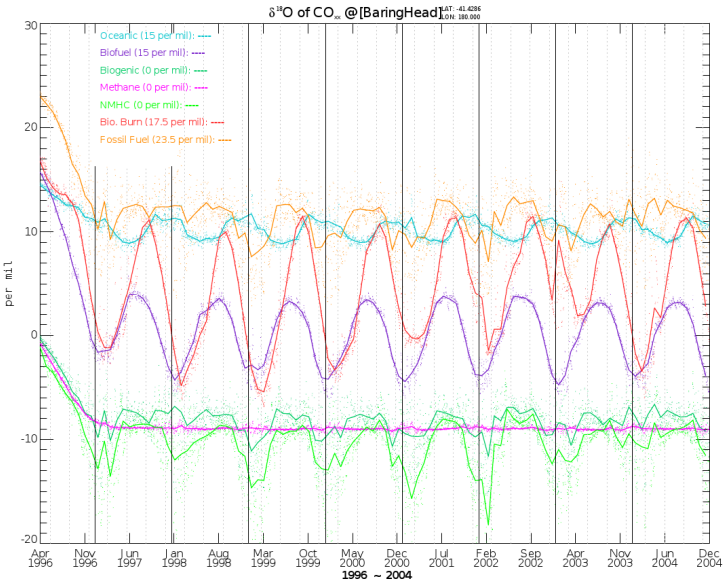
δ18O of CO2 @[BaringHead]
Oceanic (15 per mil): ----
Biofuel (15 per mil): ----
Biogenic (0 per mil): ----
Methane (0 per mil): ----
NMHC (0 per mil): ----
Bio. Burn (17.5 per mil): ----
Fossil Fuel (23.5 per mil): ----
per mil
1996 ~ 2004

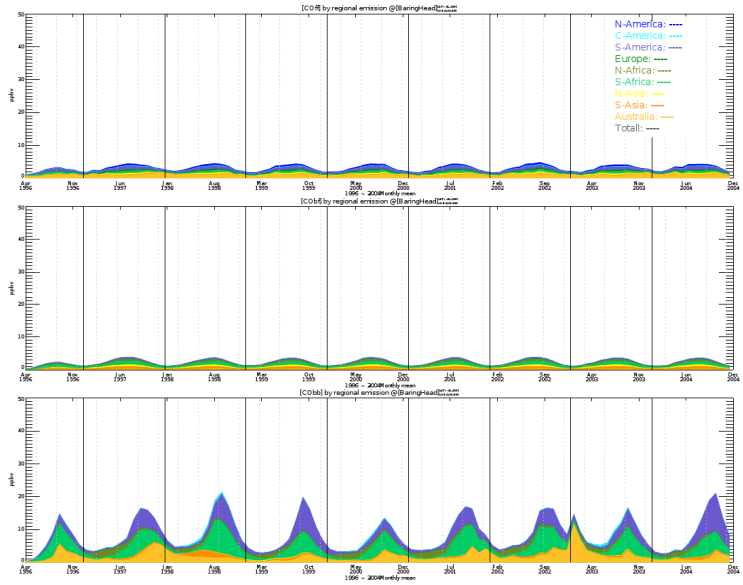
N-America: ----
C-America: ----
S-America: ----
Europe: ----
N-Africa: ----
S-Africa: ----
N-Asia: ----
S-Asia: ----
Australia: ----
Totall: ----

Scott Base

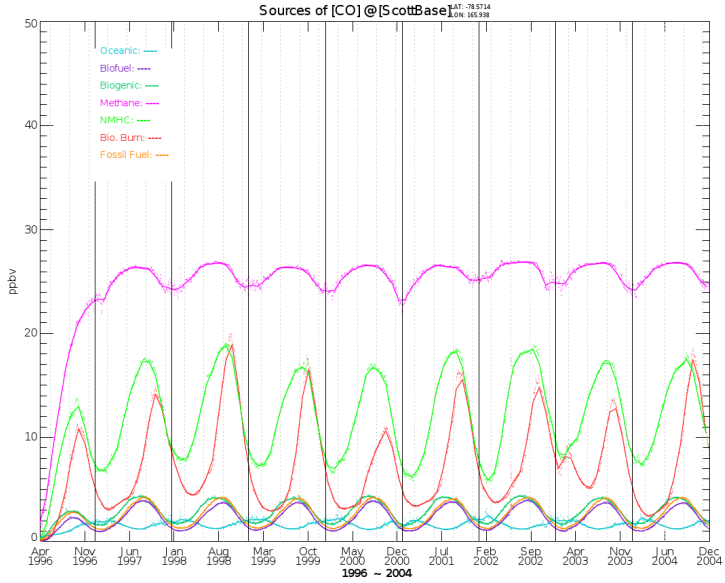
Sources of [CO] @[ScottBase]
LAT: -78.5714
LON: 165.938
Oceanic: ----
Biofuel: ----
Biogenic: ----
Methane: ----
NMHC: ----
Bio. Burn: ----
Fossil Fuel: ----
ppbv
50
40
30
20
10
0
Apr 1996
Nov 1996
Jun 1997
Jan 1998
Aug 1998
Mar 1999
Oct 1999
May 2000
Dec 2000
Jul 2001
Feb 2002
Sep 2002
Apr 2003
Nov 2003
Jun 2004
Dec 2004
1996 ~ 2004

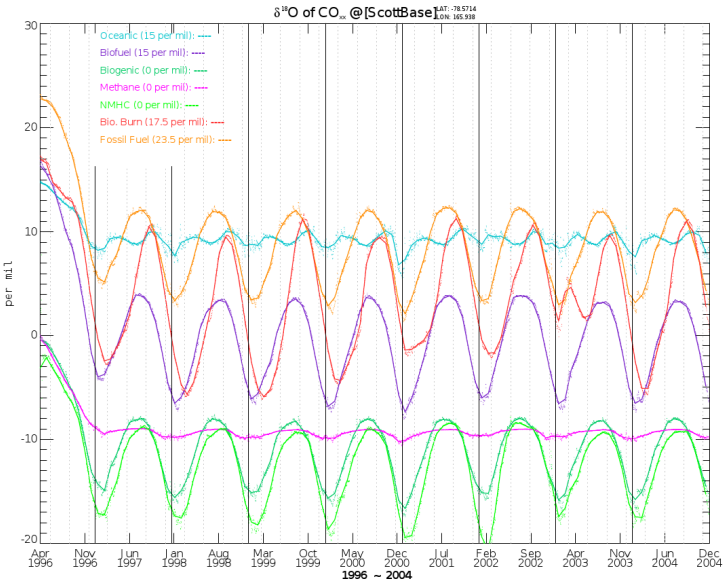
δ18O of CO𝓍 @[ScottBase]
LAT: -78.5714
LON: 165.938
Oceanic (15 per mil): ----
Biofuel (15 per mil): ----
Biogenic (0 per mil): ----
Methane (0 per mil): ----
NMHC (0 per mil): ----
Bio. Burn (17.5 per mil): ----
Fossil Fuel (23.5 per mil): ----
per mil
30
20
10
0
-10
-20
Apr 1996
Nov 1996
Jun 1997
Jan 1998
Aug 1998
Mar 1999
Oct 1999
May 2000
Dec 2000
Jul 2001
Feb 2002
Sep 2002
Apr 2003
Nov 2003
Jun 2004
Dec 2004
1996 ~ 2004

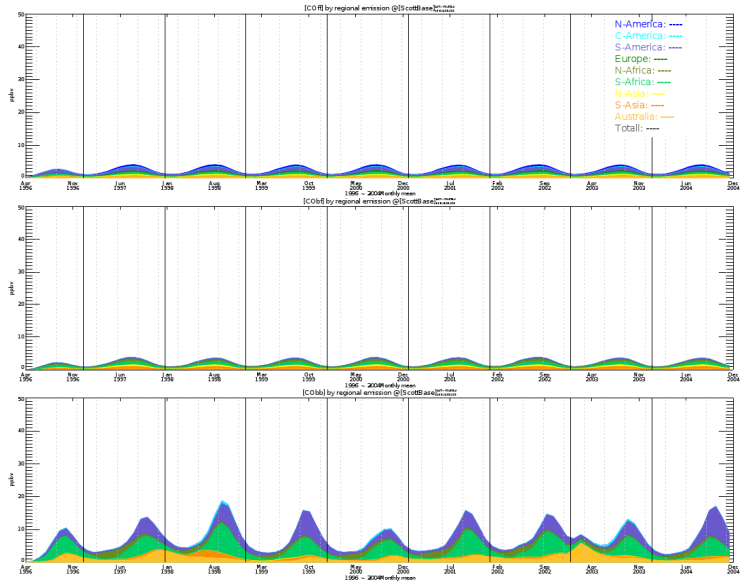
[CO fl] by regional emission @IS-cottBase[
N-America: ----
C-America: ----
S-America: ----
Europe: ----
N-Africa: ----
S-Africa: ----
N-Asia: ----
S-Asia: ----
Australia: ----
Totall: ----
ppbv
1996 ~ 2004Monthly mean
[CO bfl] by regional emission @IS-cottBase[
ppbv
1996 ~ 2004Monthly mean
[CO bb] by regional emission @IS-cottBase[
ppbv
1996 ~ 2004Monthly mean

Appendix B.

1997 ~2004 Monthly averaged source contribution at each station (ppbv)

	month	ALT	ZEP	ICE	IZO	MLO	RPB	BHD	SCO
Fossil fuel									
	1	52.4	60.3	56.5	24.5	14.7	21.0	2.1	1.3
	2	56.5	66.2	58.6	25.5	15.9	23.1	2.0	1.2
	3	59.5	64.8	63.9	29.5	17.1	22.4	2.2	1.4
	4	54.5	58.7	60.4	27.8	17.1	21.6	2.6	1.8
	5	41.7	42.9	45.4	23.3	13.0	17.0	3.3	2.5
	6	22.9	23.7	29.4	15.3	11.4	12.6	4.0	3.3
	7	13.7	16.0	18.3	11.4	8.3	9.4	4.2	3.8
	8	12.2	14.6	17.2	10.2	7.1	7.5	4.4	4.2
	9	15.1	18.3	21.9	9.8	8.0	6.5	4.4	4.1
	10	23.1	25.1	28.4	11.8	9.2	6.7	3.9	3.4
	11	30.9	35.8	37.4	15.7	10.9	8.5	2.9	2.5
	12	41.2	48.3	46.6	20.3	14.0	14.6	2.5	1.7
Biofuel									
	1	16.3	18.6	16.2	13.1	12.5	11.2	1.3	1.1
	2	19.3	21.9	19.3	15.2	14.3	13.1	1.3	1.0
	3	22.0	23.4	21.8	16.9	17.2	13.6	1.6	1.2
	4	21.9	22.7	20.8	16.0	19.6	13.4	2.0	1.6
	5	16.7	17.4	15.7	13.1	14.1	12.4	2.7	2.2
	6	9.0	9.3	8.8	9.2	10.3	8.8	3.3	2.9
	7	5.1	5.2	4.9	6.7	5.6	5.8	3.7	3.5
	8	3.9	4.0	3.8	6.6	4.0	4.9	3.8	3.8

	9	4.3	4.8	4.6	5.9	5.3	5.1	3.5	3.7
	10	6.2	6.8	6.6	6.5	6.5	6.1	2.9	3.1
	11	8.6	9.8	9.1	7.5	7.3	7.8	2.1	2.2
	12	11.8	13.8	12.1	10.6	10.6	9.4	1.5	1.5
Biomass burning									
	1	10.2	10.3	9.9	14.2	9.7	14.9	6.4	5.5
	2	9.5	9.6	9.3	14.2	10.3	13.1	4.4	4.5
	3	9.3	9.5	9.2	11.7	18.3	11.7	4.1	4.0
	4	10.6	11.0	10.3	13.0	16.7	9.7	4.1	3.8
	5	12.9	14.2	11.7	10.1	9.5	8.1	4.5	4.1
	6	10.3	11.2	9.7	7.3	6.3	6.6	5.4	4.7
	7	9.6	8.6	8.0	5.4	4.6	5.8	7.7	6.3
	8	13.1	11.7	11.2	6.0	4.8	6.5	11.9	9.4
	9	20.0	22.6	17.4	6.5	6.0	8.5	16.9	13.3
	10	21.0	22.0	19.0	7.3	6.8	8.4	17.1	15.1
	11	15.9	16.2	14.4	8.7	7.4	11.1	12.7	12.4
	12	12.1	12.3	11.4	12.7	8.1	15.2	8.5	8.6
CH_4 oxidation									
	1	26.6	26.6	26.7	27.8	27.6	29.8	27.1	24.2
	2	26.3	26.2	26.3	27.7	27.4	29.6	27.3	24.5
	3	25.9	25.8	26.0	27.5	27.2	30.2	27.1	25.3
	4	25.6	25.6	26.1	27.7	27.4	30.9	26.9	25.9
	5	25.5	25.6	26.6	28.3	28.6	31.8	26.9	26.3
	6	26.8	26.9	27.8	30.4	28.9	32.9	26.8	26.6
	7	28.5	29.1	29.6	31.6	29.7	33.4	26.7	26.6
	8	29.1	29.5	29.9	32.5	30.3	33.	26.7	26.6

	9	28.5	28.7	29.0	31.8	29.8	33.7	26.9	26.5
	10	27.9	27.8	28.0	30.3	29.4	33.2	26.9	25.8
	11	27.4	27.3	27.4	29.1	29.1	32.4	26.7	24.9
	12	27.2	27.1	27.2	28.4	28.2	30.9	27.1	24.4
NMHC oxidation									
	1	18.5	18.7	18.2	16.9	14.5	14.3	11.3	7.5
	2	18.1	18.5	18.0	17.4	14.2	14.2	10.6	7.1
	3	18.7	19.1	18.7	17.1	15.5	14.0	10.5	7.7
	4	19.3	19.9	19.5	16.9	15.3	13.5	12.7	9.2
	5	18.4	19.0	18.7	16.4	13.0	14.5	15.5	11.9
	6	15.2	15.8	17.0	17.0	12.4	13.8	16.2	14.6
	7	18.5	19.4	19.6	16.9	13.9	13.4	17.5	16.2
	8	24.4	24.8	25.2	18.5	14.5	13.8	18.2	17.3
	9	27.7	28.5	28.2	18.3	13.8	14.8	19.8	17.5
	10	26.2	26.5	25.7	17.7	13.9	15.5	19.0	16.3
	11	22.3	22.7	21.7	16.8	14.2	16.0	15.4	12.9
	12	19.8	20.2	19.5	17.2	14.7	15.5	13.7	9.7
Biogenic									
	1	8.1	8.4	7.8	4.7	3.7	4.2	3.2	1.7
	2	6.8	7.0	6.6	4.2	3.4	3.8	3.1	1.7
	3	6.1	6.3	6.2	4.0	3.2	3.3	3.2	2.0
	4	5.8	6.4	6.8	4.0	3.3	3.3	3.8	2.6

	5	6.0	6.8	8.5	4.2	3.1	3.8	4.5	3.3
	6	7.0	7.5	10.6	4.6	3.3	4.1	4.7	4.0
	7	12.1	9.5	12.9	5.0	3.6	4.3	4.5	4.2
	8	13.9	12.7	14.9	6.0	3.6	4.3	4.4	4.2
	9	14.8	16.6	16.6	6.0	3.9	4.7	4.4	3.9
	10	14.9	16.4	15.5	6.1	4.5	4.8	4.3	3.3
	11	12.2	13.3	12.4	5.9	4.5	4.7	3.5	2.6
	12	9.8	10.4	9.7	5.4	4.2	4.5	3.4	2.0
Ocean									
	1	0.6	0.6	0.7	0.5	0.5	0.7	2.9	1.9
	2	0.7	0.7	0.7	0.5	0.5	0.7	2.6	2.1
	3	0.8	0.8	0.9	0.5	0.5	0.8	2.1	2.1
	4	0.9	0.9	1.2	0.5	0.4	0.8	1.7	1.8
	5	0.8	0.9	1.2	0.4	0.4	0.8	1.4	1.6
	6	0.6	0.7	1.2	0.3	0.4	0.7	1.3	1.3
	7	0.6	0.7	1.4	0.3	0.4	0.8	1.2	1.2
	8	0.7	0.7	1.3	0.3	0.4	0.8	1.3	1.2
	9	0.6	0.7	0.9	0.3	0.4	0.8	1.6	1.4
	10	0.6	0.6	0.7	0.4	0.4	0.7	2.2	1.6
	11	0.6	0.6	0.6	0.5	0.5	0.6	2.5	1.8
	12	0.6	0.6	0.6	0.5	0.5	0.6	2.9	1.8
Total CO									
	1	132.8	143.5	135.9	101.6	83.2	96.0	54.3	43.2
	2	137.2	150.1	138.9	104.8	85.9	97.4	51.3	42.2
	3	142.3	149.7	146.8	107.2	99.1	96.0	50.7	43.8
	4	138.6	145.3	145.1	105.9	99.9	93.1	53.8	46.9
	5	122.1	126.7	127.7	95.9	81.7	88.3	58.7	51.9
	6	91.8	95.1	104.4	84.2	73.0	79.5	61.6	57.3
	7	88.1	88.5	94.8	77.3	66.1	72.8	65.5	61.9
	8	97.2	98.1	103.4	80.1	64.8	71.7	70.7	66.7

9	111.0	120.1	118.6	78.7	67.1	74.2	77.5	70.3
10	120.0	125.2	123.9	80.2	70.6	75.4	76.3	68.7
11	117.9	125.7	123.0	84.2	73.9	81.2	65.8	59.3
12	122.6	132.7	127.0	95.1	80.3	90.7	59.6	49.7

Appendix C.

A priori and *a posteriori* model-observation difference

RPB		1997	1998	2004
[CO]	Observation			
	Modeled	15.35	27.60	
	Optimized ([CO] only)	8.93	17.46	
	Optimized (Joint Simultaneous)	8.40	17.45	
	Optimized (Joint Sequential)	8.54	17.42	
d180	Observation			
	Modeled	3.71	4.88	
	Optimized (Joint Simultaneous)-adjusted isotopic source ratio	1.79	3.08	
	Optimized (Joint Sequential)-adjusted isotopic source ratio	2.02	4.52	
	Optimized (Joint Simultaneous)-fixed isotopic source ratio	2.33	5.41	
	Optimized (Joint Sequential)-fixed isotopic source ratio	2.27	5.32	
IZO		**1997**	**1998**	**2004**
[CO]	Observation			
	Modeled	10.39	17.85	
	Optimized ([CO] only)	8.85	4.86	
	Optimized (Joint Simultaneous)	9.03	4.71	
	Optimized (Joint Sequential)	9.09	4.69	
d180	Observation			
	Modeled	1.73	1.18	
	Optimized (Joint Simultaneous)-adjusted isotopic source ratio	1.04	0.56	
	Optimized (Joint Sequential)-adjusted isotopic source ratio	1.11	0.94	
	Optimized (Joint Simultaneous)-fixed isotopic source ratio	1.29	1.79	
	Optimized (Joint Sequential)-fixed isotopic source ratio	1.30	1.70	
MLO		**1997**	**1998**	**2004**
[CO]	Observation			
	Modeled			12.72
	Optimized ([CO] only)			11.97
	Optimized (Joint Simultaneous)			11.67
	Optimized (Joint Sequential)			11.76

d180	Observation			
	Modeled			4.90
	Optimized (Joint Simultaneous)-adjusted isotopic source ratio			2.52
	Optimized (Joint Sequential)-adjusted isotopic source ratio			4.00
	Optimized (Joint Simultaneous)-fixed isotopic source ratio			5.01
	Optimized (Joint Sequential)-fixed isotopic source ratio			4.96
ZEP		**1997**	**1998**	**2004**
[CO]	Observation			
	Modeled	15.65	13.53	
	Optimized ([CO] only)	9.17	8.11	
	Optimized (Joint Simultaneous)	8.86	7.26	
	Optimized (Joint Sequential)	8.60	6.78	
d180	Observation			
	Modeled	0.76	1.24	
	Optimized (Joint Simultaneous)-adjusted isotopic source ratio	0.84	0.90	
	Optimized (Joint Sequential)-adjusted isotopic source ratio	1.74	0.70	
	Optimized (Joint Simultaneous)-fixed isotopic source ratio	1.43	0.97	
	Optimized (Joint Sequential)-fixed isotopic source ratio	1.46	0.94	
ALT		**1997**	**1998**	**2004**
[CO]	Observation			
	Modeled	16.91		
	Optimized ([CO] only)	7.87		
	Optimized (Joint Simultaneous)	7.83		
	Optimized (Joint Sequential)	8.01		
d180	Observation			
	Modeled	1.47		
	Optimized (Joint Simultaneous)-adjusted isotopic source ratio	0.78		
	Optimized (Joint Sequential)-adjusted isotopic source ratio	0.75		
	Optimized (Joint Simultaneous)-fixed isotopic source ratio	1.14		
	Optimized (Joint Sequential)-fixed isotopic source ratio	1.14		
ICE		**1997**	**1998**	**2004**
[CO]	Observation			
	Modeled			9.74

	Optimized ([CO] only)			8.27
	Optimized (Joint Simultaneous)			7.72
	Optimized (Joint Sequential)			7.51
d180	Observation			
	Modeled			1.94
	Optimized (Joint Simultaneous)-adjusted isotopic source ratio			0.92
	Optimized (Joint Sequential)-adjusted isotopic source ratio			1.52
	Optimized (Joint Simultaneous)-fixed isotopic source ratio			2.41
	Optimized (Joint Sequential)-fixed isotopic source ratio			2.35
BHD		**1997**	**1998**	**2004**
[CO]	Observation			
	Modeled	9.71	5.83	9.54
	Optimized ([CO] only)	4.84	4.00	3.06
	Optimized (Joint Simultaneous)	4.92	4.01	3.09
	Optimized (Joint Sequential)	4.88	4.23	3.17
d180	Observation			
	Modeled	4.93	3.53	2.48
	Optimized (Joint Simultaneous)-adjusted isotopic source ratio	1.34	0.86	0.63
	Optimized (Joint Sequential)-adjusted isotopic source ratio	3.04	1.92	0.63
	Optimized (Joint Simultaneous)-fixed isotopic source ratio	4.50	3.65	1.90
	Optimized (Joint Sequential)-fixed isotopic source ratio	4.50	3.60	1.94
SCO		**1997**	**1998**	**2004**
[CO]	Observation			
	Modeled	5.34	5.66	7.74
	Optimized ([CO] only)	2.76	2.60	1.74
	Optimized (Joint Simultaneous)	2.71	2.58	1.70
	Optimized (Joint Sequential)	2.99	2.49	1.78
d180	Observation			
	Modeled	3.38	3.18	1.63
	Optimized (Joint Simultaneous)-adjusted isotopic source ratio	0.93	0.82	0.43
	Optimized (Joint Sequential)-adjusted isotopic source ratio	1.53	1.85	0.42
	Optimized (Joint Simultaneous)-fixed isotopic source ratio	2.91	3.31	1.15
	Optimized (Joint Sequential)-fixed isotopic source ratio	2.90	3.26	1.17